Characterization and Helicopter Flight Test of 3-D Imaging Flash LIDAR Technology for Safe, Autonomous, and Precise Planetary Landing

Vincent Eric Roback

Thesis submitted to the faculty of the Virginia Polytechnic Institute and State University in partial fulfillment of the requirements for the degree of
Master of Science
In
Electrical Engineering

Scott M. Bailey, Chair
Troy A. Henderson
Wayne A. Scales

August 13, 2012
Blacksburg, VA

Keywords: Lidar, Laser Remote Sensing, Flash Lidar, 3-D Imaging, Precision Landing, Safe Landing, Hazard Detection, ALHAT, Flight Test, Planetary Landing, Lunar Landing

ABSTRACT

Characterization and Helicopter Flight Test of 3-D Imaging Flash Lidar Technology for Safe, Autonomous, and Precise Planetary Landing

V. Eric Roback

Two flash lidars, integrated from a number of cutting-edge components from industry and NASA, are lab characterized and flight tested under the Autonomous Landing and Hazard Avoidance (ALHAT) project (in its fourth development and field test cycle) which is seeking to develop a guidance, navigation, and control (GNC) and sensing system based on lidar technology capable of enabling safe, precise human-crewed or robotic landings in challenging terrain on planetary bodies under any ambient lighting conditions. The flash lidars incorporate pioneering 3-D imaging cameras based on Indium-Gallium-Arsenide Avalanche Photo Diode (InGaAs APD) and novel micro-electronic technology for a 128 x 128 pixel array operating at 30 Hz, high pulse-energy 1.06 μm Nd:YAG lasers, and high performance transmitter and receiver fixed and zoom optics. The two flash lidars are characterized on the NASA-Langley Research Center (LaRC) Sensor Test Range, integrated with other portions of the ALHAT GNC system from around the country into an instrument pod at NASA-JPL, integrated onto an Erickson Aircrane Helicopter at NASA-Dryden, and flight tested at the Edwards AFB Rogers dry lakebed over a field of human-made geometric hazards. Results show that the maximum operational range goal of 1000m is met and exceeded up to a value of 1200m, that the range precision goal of 8 cm is marginally met, and that the transmitter zoom optics divergence needs to be extended another eight degrees to meet the zoom goal 6° to 24°. Several hazards are imaged at medium ranges to provide three-dimensional Digital Elevation Map (DEM) information.

ACKNOWLEDGEMENTS

I would, first of all, like to thank God (in the trinity of: Father, Jesus Christ, and Holy Spirit) for His love and the tiny glimmer of insight He has given me into "The Laws of Nature" which are His. I would like to thank my wife, Marie, who is at the same time the love of my life, my dearest friend, my closest advisor, and my partner on the adventure of life for all of her selfless love and encouragement. I would also like to thank my parents, Sammy and JoAnn Roback, for all of their sacrifices and for instilling in me the importance of hard work and education. I thank Marie's parents, Omar and Esther Zimmerman, for all of their many trips to lighten my load at home in order that I might write. I thank Faith and Levi for being gifts from God and for sacrificing time with "daddy" so that I could write. I thank Dr. Scott Bailey, my advisor, for being a selfless advocate and teacher. I thank Dr. Alex Bulyshev and Dr. Andrew Johnson for the range and intensity plots. I would like to thank Bill Carrion and Anna Noe for their help as master technicians. I thank the other members of the NASA-Langley (LaRC) ALHAT team for their many contributions to the effort: data acquisition and control electronics hardware and software, power, firmware, and mechanical design. I thank Dr. Farzin Amzajerdian and Dr. Bob Reisse for their leadership and personal mentoring as leaders of the LaRC ALHAT effort. I thank Dr. Chirold Epp as agency head of ALHAT for his tireless leadership and the resulting figurative tree he has tended under whose shade many of us continue to grow technically stronger each day.

TABLE OF CONTENTS

LIST OF FIGURES

LIST OF TABLES

LIST OF APPENDICES

INTRODUCTION

1.1 ALHAT Background

Many landing mission concepts being developed for exploration of planetary bodies will require precision landing on sites of high scientific value making on-board terrain hazard detection and avoidance capabilities a necessity. Future human exploration missions will similarly require precise landing with increased levels of safety over those exercised in the Apollo program if they are to become more commonplace. Despite the successes of the Apollo program (which sought to land under favorable lighting conditions at sites without significant terrain challenges) two of the six missions experienced near disaster during the landing phase with all six landings being perilous. As an example, Figure 1.1 shows that Apollo 15 landed partially in a crater which resulted in a crumpled main engine bell and a vehicle resting attitude near the safe limit.

Figure 1.1: Apollo 15 landed partially in a crater which crumpled its main engine nozzle bell and left the vehicle in a resting attitude near its safe limit (*Brady and Pashcall,* 2010).

Laser remote sensing (i.e. active sensor) technologies have the potential to play significant roles in such missions. Currently, the NASA-Langley Research Center (LaRC) is developing lidar landing sensors under the Autonomous Landing and Hazard Avoidance Technology (ALHAT) project which include a 3-Dimensional (3-D) Imaging Flash Lidar, a Doppler Lidar, and a Laser Altimeter (*Epp et. al.,* 2008).

ALHAT is pursuing laser remote sensing technology development to carry out five sensor functions: altimetry, Terrain Relative Navigation (TRN), velocimetry, Hazard Detection and Avoidance (HDA) and Hazard Relative Navigation (HRN). The 3-D Flash Lidar, the Doppler Lidar, and the Laser Altimeter can perform the five functions while also offering a degree of redundancy. A lunar landing scenario provides the framework for discussing the operations of the lidar sensors as shown in Figure 1.2.

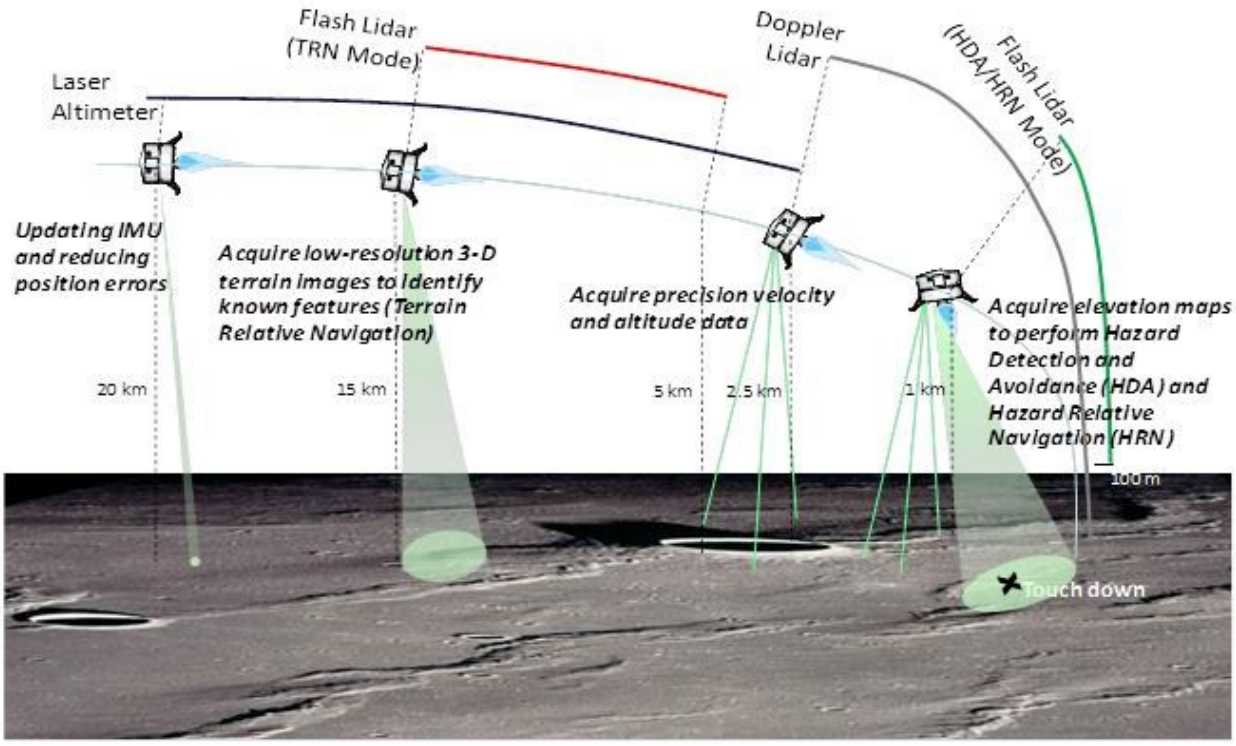

Figure 1.2: Operational scenario for ALHAT sensor systems.

As the landing vehicle initiates its powered descent toward the landing site at approximately 20 km above the surface, the Laser Altimeter begins its operation providing altitude data with sub-meter precision. Precise altitude data can significantly reduce the vehicle position error since the Inertial Measurement Unit (IMU) continually builds-up position error during the travel time from the Earth. The IMU drift error can be over 1 km for a Moon-bound vehicle and over 10 km for Mars. Accurate altitude data can reduce position error to a few hundred meters. Shortly thereafter, the flash lidar starts its operation with its laser beam concentrated to illuminate a subset of its pixels generating relatively low-resolution elevation data of the terrain below. The reason for reducing the divergence of the lidar transmitter beam to a fraction of its receiver field of view is to increase its operational range to approximately 15 km from a nominal 1 km range.

From approximately 15 km to 5 km altitude, the flash lidar can generate elevation or contour maps of the terrain. Through a process referred to as Terrain Relative Navigation, the collected maps are matched to on-board maps having known surface features such as craters. The TRN process can further reduce the vehicle relative position error from hundreds of meters to tens of meters. When the landing vehicle descends to approximately 2.5 km, the Doppler lidar initiates its operation by providing ground-relative velocity and altitude data with precisions on the order of 1 cm/sec and 10 cm, respectively. The Doppler lidar data can enable navigation to the selected landing site to within a meter in precision. From approximately 1 km to 0.5 km above ground level, the flash lidar operates with its full field of view in order to generate a high resolution elevation map of the landing zone. Since, as the vehicle descends, the flash lidar field of view illuminates a smaller and smaller area on the ground, the flash lidar continues to zoom its field of view out during descent without expanding it beyond the minimum required spatial precision. Through a process referred to as Hazard Detection and Avoidance, a digital elevation map is processed to identify hazardous features such as rocks, craters, and steep slopes and to determine the most suitable safe-landing location. Through a phase of operation referred to as Hazard Relative Navigation, the Flash lidar continues to update the map in order to establish a trajectory which leads to the selected landing location. The flash lidar operation ends approximately 100 m above the ground as the vehicle thrusters create a dust cloud which inhibits viewing. The high-fidelity navigation fix provided to the Guidance, Navigation, and Control system by the Doppler Lidar's precision velocity and altitude data allows dead-reckoning (i.e. navigation not relying any further on lidar sensor inputs) navigation to the desired landing site to ensure a safe and smooth landing.

The ALHAT goals drive the performance and operational requirements of the lidar sensor systems. The first goal is autonomous operation under any ambient lighting conditions and to any landing location. The second goal is global landing precision which means landing to within 30 meters of a predetermined location in the case of lunar landing. The third goal is hazard detection of terrain features greater than 30 cm in height and slopes greater than 5 degrees over the vehicle footprint which is taken to be approximately 10 m. The last goal is local landing precision to within a one meter error at the safe location selected by the onboard hazard detection and avoidance algorithm. Table 1.1 details the ALHAT sensor suite and breaks out the operational range, precision, and resolution requirements based on the five sensor functions including a degree of redundancy. The flash lidar is capable of performing all the functions with exception of velocimetry, which the Doppler Lidar provides. The Doppler Lidar also provides high resolution altitude and ground-relative attitude data that could further improve precision navigation to the desired landing site. The Laser Altimeter provides independent altitude data over an operational range of 100 m to 20 km. Even though the Flash lidar is capable of providing altitude data, the Laser Altimeter is employed in the operational scenario of Figure 1.2 in order to provide redundancy as well as to ease pointing authority requirements on the spacecraft since the flash lidar's HDA and HRN functions require one direction of viewing while the altimetry during an earlier phase of the mission may require a different direction of viewing the combination of which may impose significant weight and power penalties if one sensor must be positioned to perform all functions. All three lidar sensors have a nominal update rate of 30 Hz.

Table 1.1: ALHAT sensor performance requirements.

Sensor	Function	Operational Altitude Range	Precision/Resolution
Flash Lidar	HDA/HRN	1000 m – 100 m	5 cm/40 cm
	TRN	15 km – 5 km	20 cm/6 m
	Altimetry[1]	20 km – 100 m	20 cm
Doppler Lidar	Velocimetry	2500 m – 10 m	1 cm/sec
	Altimetry	2500 m – 10 m	10 cm
Laser Altimeter	Altimetry	20 km – 100 m	20 cm
	TRN[1]	15 km – 5 km	20 cm

[1] Secondary function, maybe considered as redundancy option.

The ALHAT project has accomplished three field tests of the proposed systems with the present development targeted for the fourth field test to address the HDA mode of operation. Table 1.2 details the progression toward the ultimate goals as accomplished in each prior development and field test cycle for the flash lidar, note that the second field test (not shown) was devoted solely to the Doppler Lidar.

Table 1.2: Accomplishments of previous ALHAT flash lidar development and field test efforts along with ultimate goals for all three modes of sensor operation. Note that field test #2 has been omitted since it was devoted to the Doppler lidar (*Amzajerdian et. al.,* 2009).

Mode of Operation	Field Test	Parameter	Current	Goal
HDA / HRN	1	Max operational range	400 m	> 1000 m
		Number of pixels	128 x 128	256 x 256
		FOV	3 deg	Variable 6 to 24 deg
		Range precision	8 cm	5 cm
		GSD	20 cm	10 cm
		Frame rate	10 Hz	30 Hz
		Range / intensity corrections	Post processing	Real time
TRN	3	Max operational range	8 km	20 km
		Number of illuminated pixels	10 x 10	20 x 20
		Range precision	20 cm	20 cm
		Frame rate	30 Hz	30 Hz

ALHAT's reason for employing two lidars in the present field test number four is to cover two field-of-view (FOV) ranges and address two concepts of accomplishing HDA. The first lidar, referred to as the fixed-FOV lidar, since its receiver and transmitter optics are set at one degree, is aimed at using a mosaic technique to map the landing site. The small, one-degree FOV is necessary to achieve the spatial precision goal. The second lidar, referred to as the variable-FOV (var-FOV) lidar, is aimed at using a staring technique to map the test site which requires a large enough FOV that mosaic is not needed for looking around. Since the var-FOV lidar has a large FOV for staring, the spatial precision is degraded which leads to the second objective of the var-FOV lidar which is the demonstration of an image enhancement technique referred to as super-resolution (3-D corollary to digital zoom in 2-D digital cameras) to improve the spatial precision back to the value achieve in the fixed-FOV lidar via its smaller FOV. The var-FOV lidar is also aimed at developing and testing the zoom optics technology which is ultimately intended for zooming out during descent to maintain a large ground footprint for viewing maximum area to select a safe landing site without zooming out enough to compromise the maximum spatial precision number that is tolerable.

1.2 Flash Lidar Operating Principles

Flash lidar is a new technology development with the larger realm of lidar systems that has only begun to see practical use in the last decade (*Richmond, et. al.,* 2000 and *Stettner et. al.,* 2001). As a new technology with proprietary restrictions imposed by the camera manufacturer, the author is bound in the depth of information to which he is privy that can be released and, in several cases, details are deliberately glossed over. The forerunner to flash lidar was scanning lidar in which a narrow FOV, pulsed beam was raster-scanned back and forth until it completely

mapped the scene of interest. Scanning lidar requires time to complete an image and depends upon the scanner's speed and accuracy for scene reconstruction from a multitude of lidar shots during the scan. The basic concept behind flash lidar operation is that a wide divergence, narrow pulse of laser light is emitted from a source (which triggers the start of a range counter) and travels to and illuminates a target whose backscattered pulse triggers a 2-D focal plane array in the camera populated with pixels. Each pixel operates independently and is triggered by the scene in its narrow field of view thus allowing each pixel to sense not only intensity but range as well. With flash lidar, the entire scene is completely mapped in only one frame, essentially freezing any motion in the scene since the scene is recorded simultaneously rather than being recorded one shot at a time during a lidar raster scan. The technical break-through that allowed the development of the first flash lidars was that of a focal plane array with a sufficiently large number of pixels to record a scene to a reasonable resolution which required micro-electronics design breakthroughs to permit complete processing circuits to fit side-by-side to form a dense focal plane array of pixels. Flash lidar is based on pulsed lidar technology in which ranging is accomplished using the time-of-flight of a laser pulse as opposed to coherent lidar technology in which the phase of the optical signal is used in heterodyning to create a beat frequency with a local oscillator for later signal processing.

1.2.1 Flash Lidar Technology Basics

The classic lidar equation describes the received power incident on the photo-detector in a lidar.

$$\Phi_R = \frac{\pi \Phi_T D^2}{4\Omega_T R^4} \tau_1 \tau_2 \tau_T \tau_r \frac{\rho A_{TAR}}{\Omega_{TAR}} \tag{1.1}$$

$$\Omega_T = \frac{\pi \theta_T{}^2}{4} \tag{1.2}$$

Where Φ_R is the power incident on the photo-detector, Φ_T is the transmitted power, Ω_T is the transmitter beam solid angle, θ_T is the transmitter beamwidth, τ_1 and τ_2 are one-way path transmission, A_{TAR} is the target area (such that A_{TAR} / R^2 is the solid-angle subtended by the target), R is one-way range, Ω_{TAR} is the solid angle of the return beam, D is the receiver diameter (such that $\pi D^2 / 4 R^2$ is the solid-angle subtended by the receiver), τ_T is transmitter optical transmission, τ_r is the receiver optical transmission, and ρ is the target reflectivity (*Cooke, et. al.,* 1985).

One of the multitude of uses for the lidar equation is its use to infer maximum operational range of a lidar system. The technique involves imaging a target at a relatively small, fixed distance using successively larger neutral density (ND) filters which increase the optical density (OD) through which the lidar beam passes, thereby, reducing the received power on the photodetector array. The lidar equation is then used to trade the reduction in received power for a theoretical increase in range to the target which would result in the same reduction in received power since the beam would diverge more for a farther target and hence lose intensity. This trade is possible since most terms in the lidar equation can be held constant from run to run such as those which address detector area, laser transmitter power (assuming the laser output power is stable run to run), transmitter beam solid angle (no change to beam divergence lenses), solid angle subtended by the target (same fixed target used), target reflectivity (same target used which remains at the same orientation from run to run to preserve angle-dependent reflectivity), solid angle of the return beam (same target at same orientation or a target which is Lambertian,

meaning a perfectly diffuse reflector with π for the return beam angle), path transmission (unchanging atmospheric losses), and receiver optics transmission (no change to receiver optics between runs). Thus the two changing terms which are balanced are transmitter optics transmission in the numerator and range squared in the denominator. The neutral density (ND) filters effect a percentage change in optical transmission per the equation:

$$\%T = 10^{-OD} \tag{1.3}$$

thus applied to the lidar equation to find the percentage change in range with all constant parameters remaining at 100% of their original value from run to run:

$$\Phi_R = \frac{\tau_T}{R^2} = 1 = \frac{\%\tau_T}{\%R^2} = \frac{10^{-OD}}{\%R^2} \tag{1.4}$$

so that

$$R_{THEORETICAL} = R\sqrt{10^{OD}} \tag{1.5}$$

The lidar equation also addresses atmospheric transmission which plays directly into the wavelength at which the lidar is designed to operate for maximum range. Due to the constituents of the atmosphere at different altitudes, certain wavelengths experience less attenuation than others as shown in Figure 1.3.

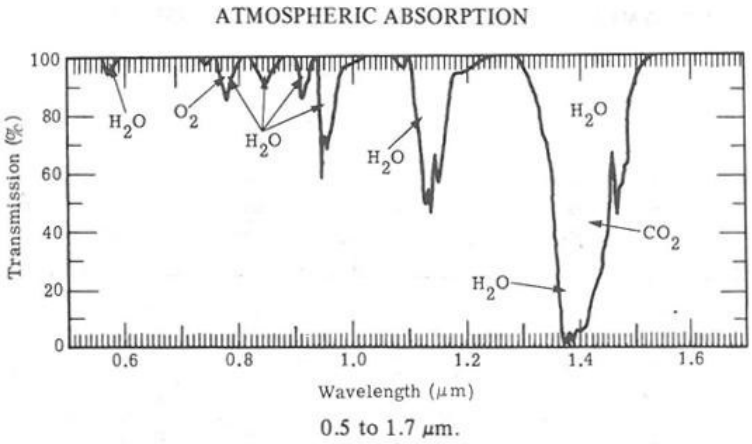

Figure 1.3: Atmospheric transmission at sea level over a 0.3 km path (*LaRocca*, 1985).

Since the goal of the ALHAT lidars is ranging to ground targets from a flight vehicle, the ALHAT lidars are designed to experience maximum atmospheric transmission which is one reason for the operations at 1.06 μm. Note that since transmission is affected by atmospheric constituents, lidars can be used to indirectly measure properties of those constituents.

The lidar equation addresses target reflectivity which plays directly into prediction of maximum operational range. The lidar equation indicates that target reflectivity directly reduces the return power at the detector which indicates that when conducting experiments in the laboratory to characterize maximum range, the expected reflectivity of the ground targets during flight test should either be simulated properly or known so that corrections can be made. Target reflectivity is a function of wavelength and incidence angle. For a perfectly diffuse target, the reflectivity is maximum at a zero incidence angle and then drops off with a cosine dependence on angle of incidence to zero reflectivity at a 90° angle of incidence. The lidar equation is used to determine the theoretical range which results from a change in the target reflectivity in much

the same manner as it is used to infer theoretical range as the transmitter optical transmission is changed as discussed previously. The equation that results after all constant terms are eliminated is:

$$\Phi_R = \frac{\rho}{R^2} = 1 = \frac{\%\rho}{\%R^2} \tag{1.6}$$

so that

$$R_{THEORETICAL} = R\sqrt{\%\rho} \tag{1.7}$$

Temporal and spatial pulse shape play key roles in optimal lidar functioning. A time-of-flight lidar requires a laser pulse with a smooth and repeatable pulse shape so that the pulse return peak can be precisely measured. The ideal pulse spatial profile for most flash lidar applications is that of a top-hat. A top-hat beam has a uniform intensity with intensity dropping off sharply at the beam edges. A top-hat is ideal in that the entire detector array is uniformly illuminated to minimize issues with saturation of some pixels and insufficient illumination of other pixels which can introduce maximum range issues and, depending on the limits of the sensor's dynamic range, can create problems with correcting for amplifier-induced phase delay which plays directly into range precision as will be discussed below. A top-hat with sharp intensity drop at its edges also supports maximum range since a minimal amount of the laser power is wasted on the periphery of the beam during drop-off.

The lidar equation is combined with noise terms to produce the classic signal-to-noise ratio equation in terms of radiant power.

$$\left(\frac{S}{N}\right)_{\Phi} = \frac{\frac{1}{2}m^2\left(\frac{\eta e}{h\upsilon}\right)^2\Phi_R^2}{2e\frac{\eta e}{h\upsilon}BF\left(\Phi_R+\Phi_B+\frac{h\eta I_d}{\eta e}\right)+\left(\frac{4KTB}{M^2R_{eq}}\right)+\left(\frac{i_{Namp}^2{}^B}{M^2}\right)} \quad (1.8)$$

$$F = kM + \left(2 - \frac{1}{M}\right)(1 - k) \quad (1.9)$$

Where m is the modulation index of the transmitter source (m=1 for a pulsed system), I_S is the photo-current due to the signal, M is the electron multiplication factor (i.e. detector internal gain), R_{eq} is the equivalent resistance of the detector load, e is the electron charge, B is the detection bandwidth, Ib is the photo-current due to background radiation, K is the Boltzmann's constant, T is the absolute temperature (including the amplifier noise figure), F is the excess noise factor due to the multiplication factor, η is the quantum efficiency of the detector, hυ is the photon energy, Φ_R is the received radiant power at the detector, Φ_B is the radiant power generated by the background, and k is the ionization ratio of the photodetector (*Cooke et. al.,* 1985). Since the detector internal gain, M, resides in both the numerator and the denominator of the denominator terms, there is an optimum value of detector internal gain which will maximize the lidar's signal to noise ratio. The optimum value of M is dependent on the relative strengths of the terms in the denominator which can be generally grouped into those representing the photodetector dark current, the amplifier noise power, the signal optical power, and the background optical power. Since the relative strength of the terms varies from one lidar design to another, the selection of M is lidar specific within the bounds of the available detectors of course. Figure 1.4 shows the notional dependence of signal to noise ratio on noise power and signal power whose value is optimal for a certain value of detector internal gain, M, for the specific case of avalanche photo-diode (APD) type detectors.

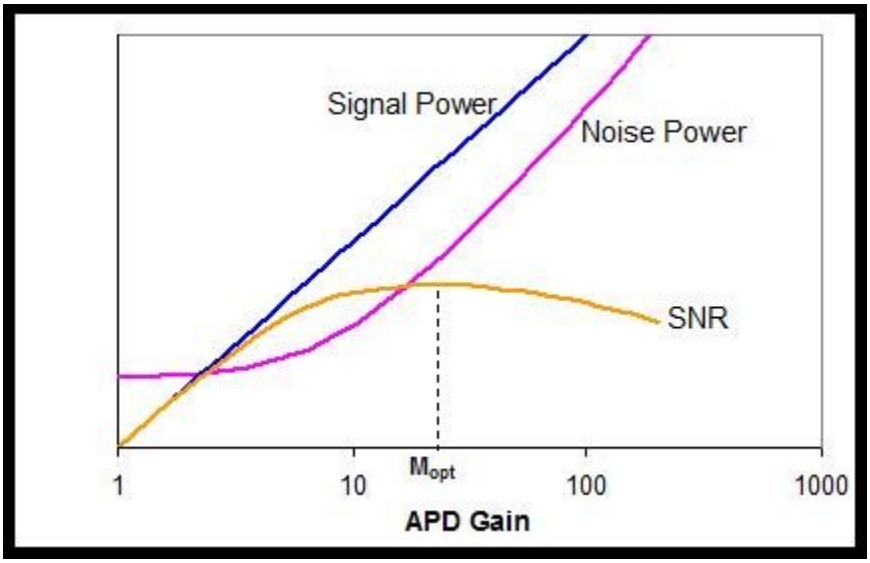

Figure 1.4: APD performance versus its multiplication gain (*Singh et. al.,* 2005).

The ALHAT flash lidars utilize APD detector technology. APD detectors make use of a cascading (or "avalanching") effect to amplify photo-electrons. When an electron is freed by the incident action of a photon, that electron is accelerated in the strong electric field which arises as a result of the APD's reverse bias voltage (as in a reverse-biased diode in regular circuit design). As the accelerated electron collides with the atomic lattice of the detector material, additional electrons are freed which in turn do the same all resulting in the avalanching effect which effectively provides gain to the original electron signal. The material used in APD detectors determines its sensitivity to wavelength. The quantum efficient of the Indium-Gallium-Arsenide (InGaAs) APD is shown in Figure 1.5. Quantum efficient is a measure of how robustly a given detector converts photons into photo-electrons.

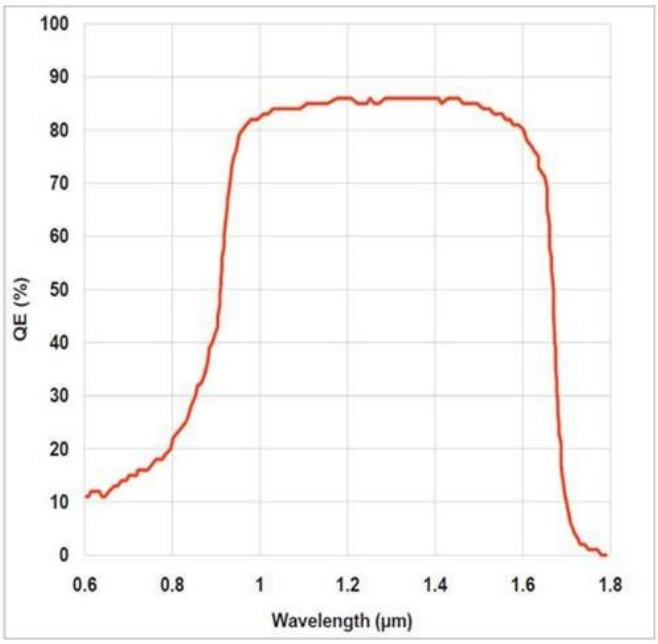

Figure 1.5: Quantum efficiency for an InGaAs APD as a function of wavelength. Courtesy of Andover Technology plc. Available at http://www.andor.com/scientific_cameras/idus-ingaas/array-1-7.

As Figure 1.5 shows, InGaAs APD's have high efficiency at wavelengths which are compatible with good atmospheric transmission as shown in Figure 1.3 which is part of the reason for selection of 1.06 µm for the ALHAT lidars. Although InGaAs detectors are sensitive to the near infrared (IR) spectrum, that material is not favorable for embedding the micro-electronic circuits needed for acquiring, conditioning and storing the detector output. If Silicon were sensitive to the near-IR spectrum, it would be ideal for use in detectors, but it is not sensitive. The design compromise is to use InGaAs for the detector and to use Silicon as the base for the electronics, which reside on a separate board termed a Read-Out Integrated Circuit (ROIC), and then to electrically bond the two boards together to form a focal plane array (FPA). The bonding of the two boards is a process referred to as hybridization. Typically Indium is used as the bonding

material, with a bump being placed on each board and the two boards pressed together with all bumps perfectly aligned so that press-bonding occurs at each detector so it is connected to its respective set of data acquisition and conditioning electronics as shown in Figure 1.6. The focal plane array of Figure 1.6 is that of the Advanced Scientific Concepts, Inc. (ASC) Tiger Eye camera used in the present development.

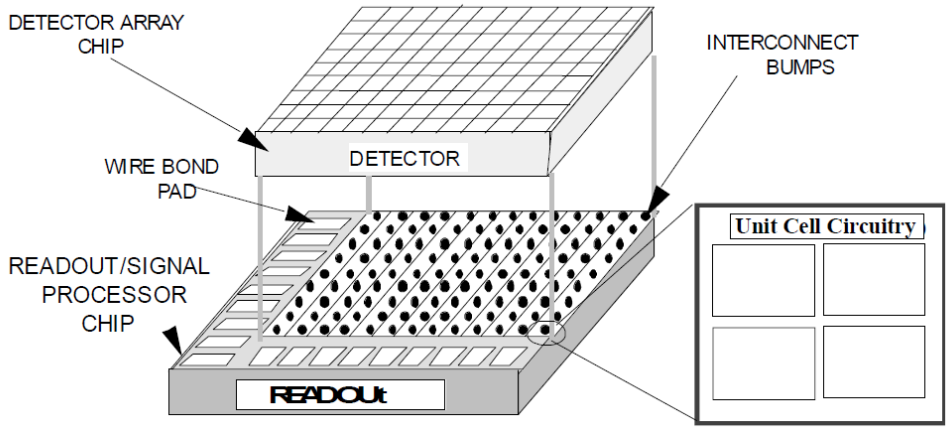

Figure 1.6: Bump bonded focal plane array, consisting of InGaAs APD detector and silicon-based ROIC, for the ASC Tiger Eye 3-D imaging camera used in ALHAT (*Dries et. al.,* YEAR).

The hybridized FPA generally requires calibrations in order to ensure that all pixels (i.e. all detectors with their respective read out circuitry) respond the same to incidence photons so that precise results are generated. One such correction that is needed is referred to as non-uniformity correction. Non-uniformity refers to differing output from pixel to pixel given the same number of illuminating photons. The calibrations are done during FPA and camera manufacturing, but need to be updated during normal experiment operations to correct for day to day or hour to hour drifts in the correction curves which will be discussed in additional detail in the flash lidar camera section. Another correction that is critical is referred to as range / intensity

correction. The need for range / intensity correction arises from the amplification of the detector signal in the ROIC. The pre-amp in the ROIC, like all amplifiers, has its own frequency response consisting of a gain versus frequency component and a phase versus frequency component. Unless Bessel technology is used (and it is not in the ALHAT flash lidars) which exhibits a flat phase response versus frequency, then the pre-amp will introduce some frequency-dependent phase shift in the signal it amplifies from the detector. A given pulse actually consists of a continuum of frequency components, as can be seen by looking at its Fourier Series components. The larger a pulse's amplitude, the higher the peak frequencies it contains generally. The pre-amp's frequency response will act on each of the frequency components to introduce phase shifting and when the final time-domain version of that signal is considered as it exists the pre-amp, the pulse shape will be distorted in phase as compared to the signal that entered the pre-amp. Since a time-of-flight lidar uses timing to infer range to target, and since the return pulse's peak is used to stop the range counter, then a phase distortion will result in a distortion to the actual range to target for that pixel. Since a given target can have a continuum of reflectivities and since the laser pulse which reaches the target will not be a perfect planar wave (i.e. it will exhibit some spatial intensity variation), then the return signal as seen at different pixels will have different intensity amplitudes. So, in theory, a flat target board which should return that same range value at each pixel, will instead return a span of ranges due to the phase distortion introduced by the amplifier. A calibration is accomplished, which is described in the lab characterization section, to minimize the phase distortion's effect on range precision, where range precision refers to all pixels outputting the same range value when similarly stimulated by a range target.

A micro-lens array is typically used in conjunction with a detector array. With a larger active sensing area, a detector is more sensitive, however, a larger active area also means higher noise and larger capacitance which reduces bandwidth. Reducing a detector's active area leaves gaps between pixels which act as blind spots where photons fall but are not sensed. A design compromise entails making the detector active area smaller, but placing a micro-lens array between the detector and the target source which acts to collect the photons that would normally fall between detectors and instead channel them to a detector active area. The amount of detector array area which is effectively sensitive given the light collecting abilities of the micro-lens array is termed fill factor. The f/# of the micro-lens array is selected based upon manufacturing constraints and the planned optical receiver design for the lidar. The f/# concept is detailed in the optics discussion below.

Several geometric optics principles are useful when considering lidar development and testing. Figure 1.7 shows a simple lens to illustrate several basic optics concepts germane to flash lidar development, where R is the range to target from the optic center of the lens, f is the focal length of the lens, d is the detector size, a is the lens aperture, and θ_{FOV} is the field of view of the lens.

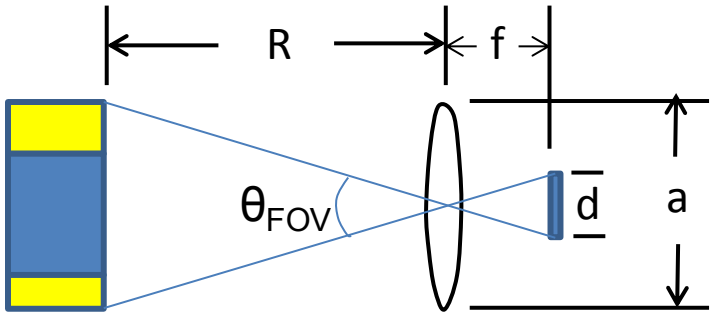

Figure 1.7: Simple lens illustrating basic geometric optics principles.

The field-of-view (FOV) is calculated from the detector size and the focal length of the lens as:

$$\theta_{FOV} = TAN^{-1}\left(\frac{d}{2f}\right) \tag{1.10}$$

$$IFOV = \frac{\theta_{FOV}}{\#\ pixels} \tag{1.11}$$

The IFOV serves as the spatial precision number for the lens since smaller angular information is not resolvable since the pixel is the smallest resolvable portion of the incoming optical information. When IFOV is applied to range, a parameter referred to as Ground Spot Distance (GSD) is formed which serves as a maximum linear version of the spatial precision useful in comparing spatial precision to hazard size. Another key optical parameter, the f/#, is calculated as:

$$f/\# = \frac{f}{a} \tag{1.12}$$

The f/# can be thought of as a measure of the angle of light accepted by the detector, with smaller f/#'s corresponding to larger angles. The larger the angle of light accepted, the larger the portion of the aperture utilized for bending light, and with a larger portion of the lens being used also comes larger aberrations since aberrations are generally minimal near the center of a lens. In relation to micro-lens design, the f/# selected becomes the limiting f/# for design of the receiver optics since receiver optics designed with a smaller f/# (i.e. accepting a larger cone angle of light) will accept photons from a larger cone angle than the micro-lens array with a smaller f/#, thus a portion of the receiver optics cone angle will be rejected by the micro-lens which means that photons are wasted and that the receiver optics aperture is wasted. Wasted aperture on the receiver optics is inefficient since a larger aperture means more volume is consumed by the sensor and it also means a greater total weight for the sensor. Lastly, the aperture, a, dominates the light gather ability of the lens which is quantified by the throughput

parameter. The larger the aperture (as long as it does not violate the micro-lens f/#), the higher the intensity the return signal will achieve at the photodetector.

1.2.2 ALHAT 3-D Imaging Flash Lidar Camera

NASA-LaRC, the ALHAT sensors lead, produces the ALHAT flash lidars through integration of components from leading manufacturers in combination with in-house design and development of portions of the optics and all of the support mechanical, electrical, and software components. The 3-D imaging camera used in the ALHAT flash lidars is the Tiger Eye (Figure 1.8) manufactured by ASC.

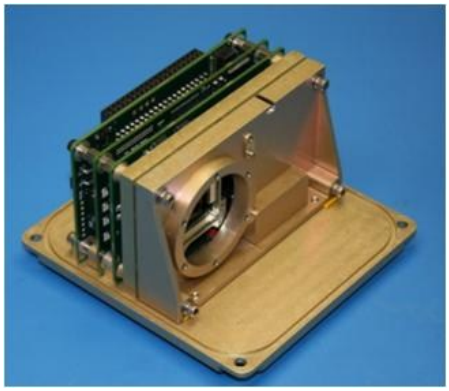

Figure 1.8: ASC Tiger Eye 3-D imaging camera.

ASC, one of the early innovators of flash lidar systems, is one of the few companies which is able to produce flash lidar cameras, given the complexity and recentness of the technology (*Stettner et. al.,* 2005 and *Stettner*, 2010). An operations sequence which follows one laser pulse from origination to ultimate range data output is described, which is followed by a discussion on data uncertainty and several key design issues which affect operations and data interpretation.

The flash lidar operations sequence is kicked off by the issuance of a command from the ALHAT flight software to the Tiger Eye camera to begin a ranging sequence. The Tiger Eye then issues a trigger signal to the laser to generate a pulse. Next, a pulse is generated by the laser portion of the sensor. The fixed-FOV lidar (so named since its distinguishing characteristic is that its receiver and transmitter optics are fixed at one value of 1 deg) utilizes a Big Sky laser (class IV) with the smooth Gaussian temporal pulse shape shown in Figure 1.9. The figure shows the pulse width to be 8 ns full-width, half max (FWHM). A short pulse width is critical to minimizing ranging uncertainty since peak detection is the reference point to stop the range counter and detection of peak is made more difficult the wider the pulse due to sampling demands and resulting uncertainty. In air, each nanosecond is equivalent to approximately one foot of wave travel. A smooth pulse shape is also critical again for purposes of repeatable finding the peak of the pulse in an automated manner.

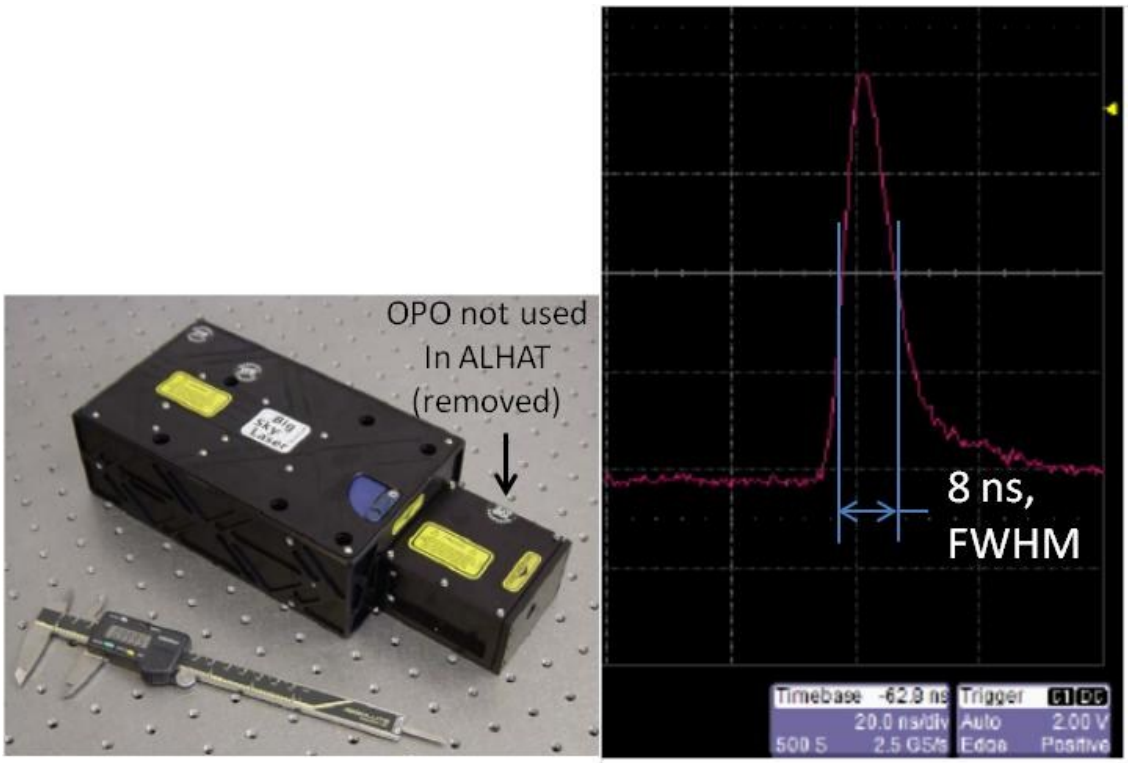

Figure 1.9: Big Sky laser head (electronics not shown) and its temporal pulse shape used in the fixed-FOV lidar (*Quantel*, 2008).

The var-FOV lidar (so named since its distinguishing characteristic is that its receiver and transmitter optics are variable over a range from 6 to 16 degrees), utilizes a Fibertek laser (class IV) with the smooth Gaussian temporal pulse shape shown in Figure 1.10. The figure shows the pulse width to be 8 ns full-width, half max (FWHM). Both lasers operate at a wavelength of 1.06 μm based on the above information concerning optimum wavelengths to minimize atmospheric attenuation, wavelengths which the InGaAs detector is sensitive to and lastly to minimize mass, volume and power requirements. Mass, volume, and power are minimized by use of 1.06 μm since that is a basic wavelength output by Neodymium-Doped: Yttrium Aluminum Garnet (Nd:YAG) lasers and requires no modification. Wavelength modification, by an optical parametric oscillator (OPO) for example, significantly reduces the pulse energy output

(note that the average power of a laser is simply a product of its pulse energy, Ep, with its pulse repetition frequency) of a laser requiring a larger laser to output the same pulse energy as a laser without wavelength modification. The larger laser size coupled with the associated larger power and cooling requirements as well as the additional mass and volume of the OPO (or similar) all lead to an increase in mass, power, and volume.

After the pulse is fired by the laser, the camera is notified and the pulse travels through the conditioning transmitter optics. The laser notifies the camera that a pulse has been fired through an optical pick-off fiber in which a portion of the backscatter of the laser pulse from a transmitter optic enters a fiber optic and is routed into the camera. The optical signal used to signal the camera that the laser has fired is referred to as an optical t0 signal since it effectively sets the start point in time for range counting to begin.

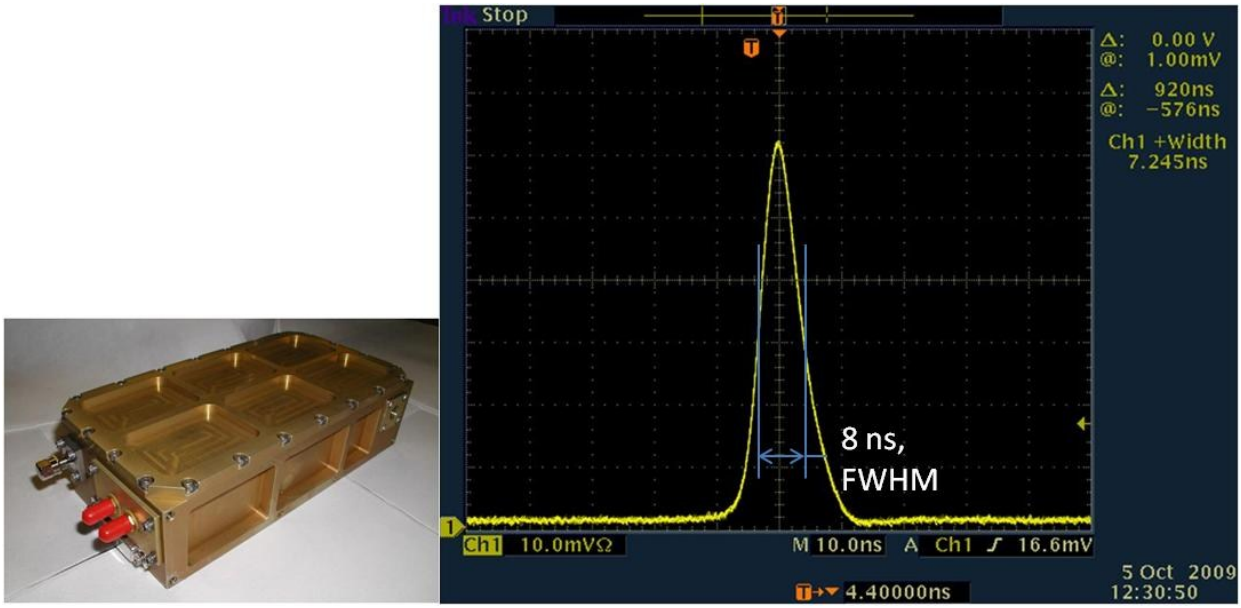

Figure 1.10: Fibertek laser head (electronics not shown) and its temporal pulse shape used in the var-FOV lidar (*Hovis et. al.*, 2010).

The t0 serves the additional function that it virtually eliminates the laser jitter (an unavoidable reality when working with passively Q-switched lasers like the Big Sky and Fibertek) from corrupting range counting, since the range counting starts when the laser actually fires, whenever that finally occurs. The optical laser pulse travels through conditioning transmitter optics designed to set its divergence angle to the desired value to match the receiver optics FOV. The details of divergence and FOV are covered in the lab characterization section. The transmitter optics also smooth the intensity profile if needed, Big Sky needed it while the Fibertek did not. Figure 1.11 shows the fixed-FOV lidar's transmitter optics (which consist of two turning mirrors, a 5x beam expander, a beam shaper, and a mount for the t0 fiber optic) and Figure 1.12 shows the var-FOV lidar's transmitter optics (which consist of three turning mirrors and three beam expanding lenses on a zoom motor stage, and the t0 fiber optic). LaRC designed and developed the transmitter optics.

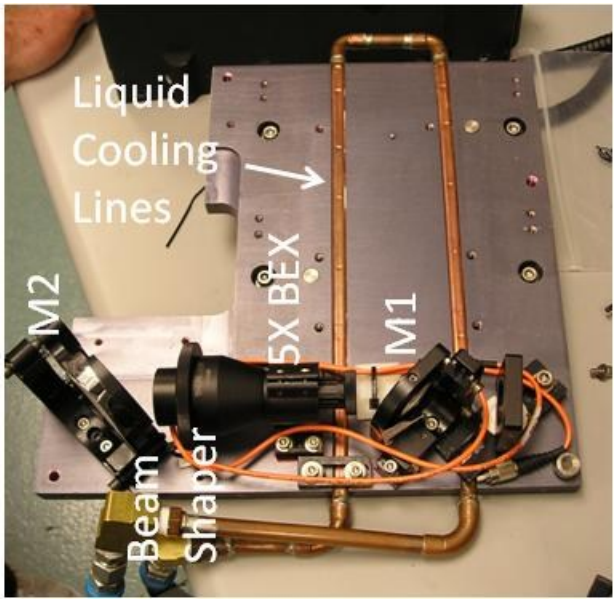

Figure 1.11: Fixed-FOV lidar transmitter-optics-only consisting of two turning mirrors, a 5x beam expander, and a beam shaper along with the t0 fiber optic and its mount.

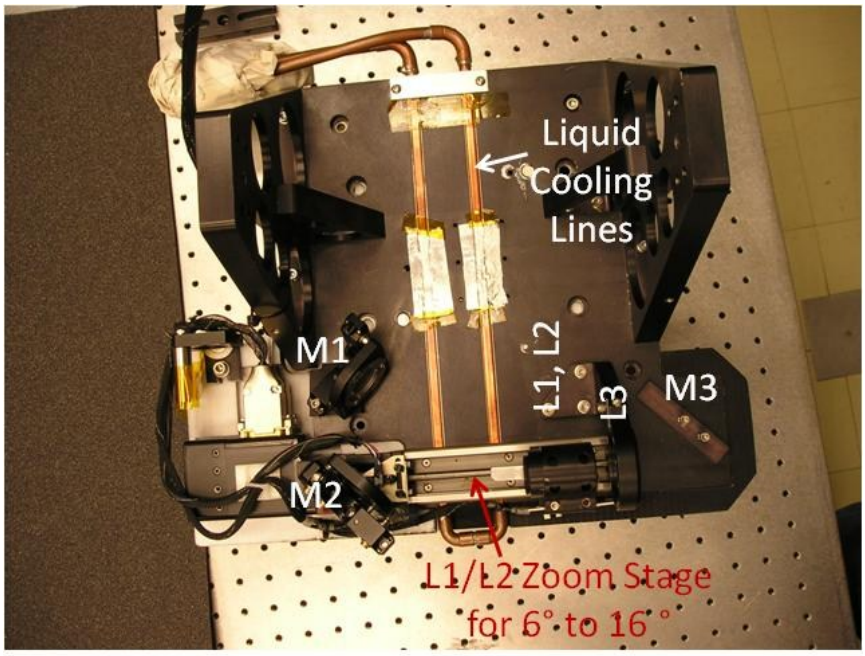

Figure 1.12: Var-FOV lidar transmitter-optics-only consisting of three turning mirrors and three beam expanding lenses on a zoom motor stage, note that the last 3 inch turning mirror and the t0 fiber optic are not shown.

Once the laser pulse exits the transmitter optics, it travels to the target and back to the lidar receiver. The beam travels through the atmosphere en-route to the target and experiences some attenuation. Soon after the beam exits the transmitter optics, it is at its smallest area for the trip and is hence most likely to backscatter strongly enough from nearby aerosols (or nearby structure if off-axis reflections have occurred in the transmitter optics at some point) to saturate the sensitive detector which necessitates baffling in some cases or dialing down the sensitivity of the camera in other cases which is undesirable since a less sensitive system does not achieve as great a maximum range. Thus care is taken to minimize off-axis reflections and to align and position transmitter and receiver to minimize such backscatter. The pulse contacts the target and is returned in an attenuated state depending upon the surface reflectivity of the target which is

wavelength, incidence angle, and surface finish dependent. The pulse travels back and enters the receiver optics.

Once the faint pulse backscatter reaches the receiver optics, it is collected and focused onto the detector array for sensing. Focus is set carefully to maximize the depth of field so that the largest span of ranges possible are in focus when set to infinity focus. The receiver optics are set to match the divergence of the transmitter optics, with some overfilling allowed to guard against misalignment issues. Pictures of the receiver optics are seen in subsequent sections. The signal passes through a solar filter which removes most of the solar background so that the return is mostly independent of sun position and illumination since the InGaAs is sensitive in the very upper portion of the solar band. The signal then travels through a high transmission window which protects the camera's FPA and is sensed by the detector. Each pixel sees its own portion of the return signal.

At the detector, the return pulse is digitized, used to measure range and intensity, corrected, and then output to the ALHAT flight software. Once the pulse intensity exceeds a pre-set threshold value, the digitized pulse is stored. The pulse peak is used as the range counting stop point. The roundtrip time is used to compute range. As discussed in the previous flash lidar technology basics section, analog amplification of the pulse introduces phase distortion which means that the computed range value contains a slight error. In real-time, the range / intensity calibrations are applied to each pixel and the range computation is corrected. Intensity has also already been corrected for pixel-to-pixel non-uniformity through coefficients loaded in firmware which are augmented every 15 or 20 minutes by real-time updating of the non-uniformity parameters (essentially a dark-current measurement). The range and intensity data for each pixel is then packaged along with a header containing various settings and

housekeeping parameters and sent to the ALHAT flight software for time tagging, storage and transmittal to the rest of the ALHAT system.

Precision, accuracy, and resolution provide a quantification of data uncertainty. Using the classic illustration of a dart board, precision refers to the ability to put all darts (or range data points) at the same point on the board (or have all range values from all pixels read the same) regardless of whether that point is on the bull's eye (perfect accuracy) or on the edge of the dart board (poor accuracy). Accuracy refers to the ability to put any single dart on the bull's eye (or have any signal range value correspond to the actual true range). For ALAHT, resolution refers to the combined flash lidar system's ability (sensor and hazard detection algorithms combined) to identify a target in flight. The correlation between precision and resolution for ALHAT hazard detection is defined in a paper describing algorithm requirements (Huertas et. al., 2010). Thus, resolution is dominated by and linked directly to precision.

Spatial precision is dominated by FOV and number of available pixels. Spatial precision is dominated by the number of components of information available in each image in the x and y directions for use in identifying hazards which may be spaced closely together. The IFOV described earlier serves as the spatial precision number for the lens since smaller angular information is not resolvable since the pixel is the smallest resolvable portion of the incoming optical information. Spatial precision as applied to GSD actually improves during descent, since GSD (for a constant IFOV) decreases with range; the negative side of this improvement is that the FOV footprint on the ground decreases with range and, thus, the lidar is not able to see as large a swath on the ground for hazard detection. The var-FOV lidar is being evaluated for future operations in which FOV will be increased during descent with the control parameter

being GSD, i.e. GSD will be maintained during descent so that the GSD goal is met while still maximizing the ground footprint of the FOV.

Range precision is dominated by the ability to precisely determine the true return pulse peak point. A time-of-flight lidar relies on a t0 to provide a start time for ranging and, in the case of the ALHAT lidars, a pulse peak detection to provide a stop time for ranging. The optical t0 virtually eliminates the laser jitter from shot to shot from entering the precision uncertainty since a portion of the actual laser pulse is fed to the camera to start the range time count. If all pixels responded exactly the same, then precision would be perfect since all pixels receive the actual return pulse at the same time. All pixels do start range counting at the same time since the t0 is globally applied to all. Thus, sources of imprecision are centered on the peak detection. The first source of peak detection error is that the return pulse (being on the order of 8 ns) cannot be digitized to an infinitely high fidelity due to the extremely high sample rates involved which would be simultaneous for over 16,000 pixels. Since each pixel is digitized independently, any interpolation-related errors from one pixel to the next feed into the overall range precision error of the image. The second source of peak detection error is associated with the range / intensity phase shift phenomenon described in the flash lidar technology basics section. To recap briefly, since the target reflectivity and the beam's spatial profile are not ideal such that an ideally constant intensity pulse is returned, then different pixels experience different intensity values when sampling the return pulse. The pre-amp's frequency response results in some phase distortion to the signal from each pixel. The phase distortion translates directly into time and thus range distortion. Each pixel has its own pre-amp further complicating the correction process. Range / intensity calibrations are applied in real time with correction coefficients

embedded in camera firmware. Since the calibration process is not perfect, it leaves some precision error un-fixed.

Range accuracy is dominated by t0 biases and camera on-board range counter uncertainties. Range accuracy for the present development cycle is not critical, since hazard detection happens within one frame or via stitching together of a multitude of frames. When hazard detection happens within one frame, then range precision determines what size hazard can be picked out of the image since all pixel information is intrinsically co-registered relative to other pixels. When hazard detection occurs through stitching together of multiple frames in a mosaic scanning sequence (in which the gimbal on which the lidar is mounted raster scans back and forth to allow the lidar to "see" more terrain than just that which exists in its field of view), any range accuracy bias offsets are eliminated since the images act as differential measurements and thus the only remaining range accuracy uncertainty is the random uncertainty from shot-to-shot which is corrected by co-registering features from one frame in the mosaic to the next and adjusting range so that they form a continuous terrain map. The first of the two main sources of range accuracy error is t0 error. The t0 is taken as the actual time which the laser pulse is generated and range counting starts at that instant, however, there is some transport delay in the transmission to the camera through the fiber optics and in the sensing process. Note that there is not a delay in the generating process since the present t0 is an optical t0 which is originates directly from the laser pulse, however for electrical t0 signals generation delay is an issue. The second of the two main sources of range accuracy error is error in the range counting clock. The clock's actual period must be assumed to be a certain number and that period used in multiplying by the number of clock counts between t0 and pulse peak. The actual clock period is offset some amount from the assumed value and the period is temperature dependent and thus drifts a little.

The lidar camera has sensitivity parameters that are set for optimal operations. The sensitivity parameters modify the operation of the detector array, the amplifiers, and the detection threshold. At the one extreme, the parameters can be set to make the lidar sensitive to faint returns from distant objects (for maximum range performance) at the expense of triggering on undesirable faint returns from nearby aerosols or structure instead, while, at the opposite extreme, the parameters can be set to make the lidar insensitive to faint returns (resulting in poor maximum range performance) to avoid triggering on returns from nearby aerosols or structure.

Lab Characterization Testing

2.1 Sensor Test Range facility

The lidars are characterized on the Sensor Test Range (STR) facility at LaRC. Figure 2.1 shows that the STR is an outdoor test range in which lidars (including non-eye-safe lidars) are fired from the building 1202 roof to targets either on the 1202 roof or to targets on the neighboring roof of building 1209. The lidars are fired from an open window as shown in the lower right of the figure. The upper right of the figure shows the reflectivity and range to the three target boards. The targets at 7 and 49 meters are flat metal boards painted in a way that their reflection is diffuse and nearly Lambertian. Figure 2.2 shows detail of the target located on the neighboring roof of building 1209. Figure 2.2 delineates the various surface reflectivities and target sub-component sizes. Figure 2.3 shows both lidars (fixed-FOV and var-FOV) being characterized on the LaRC STR.

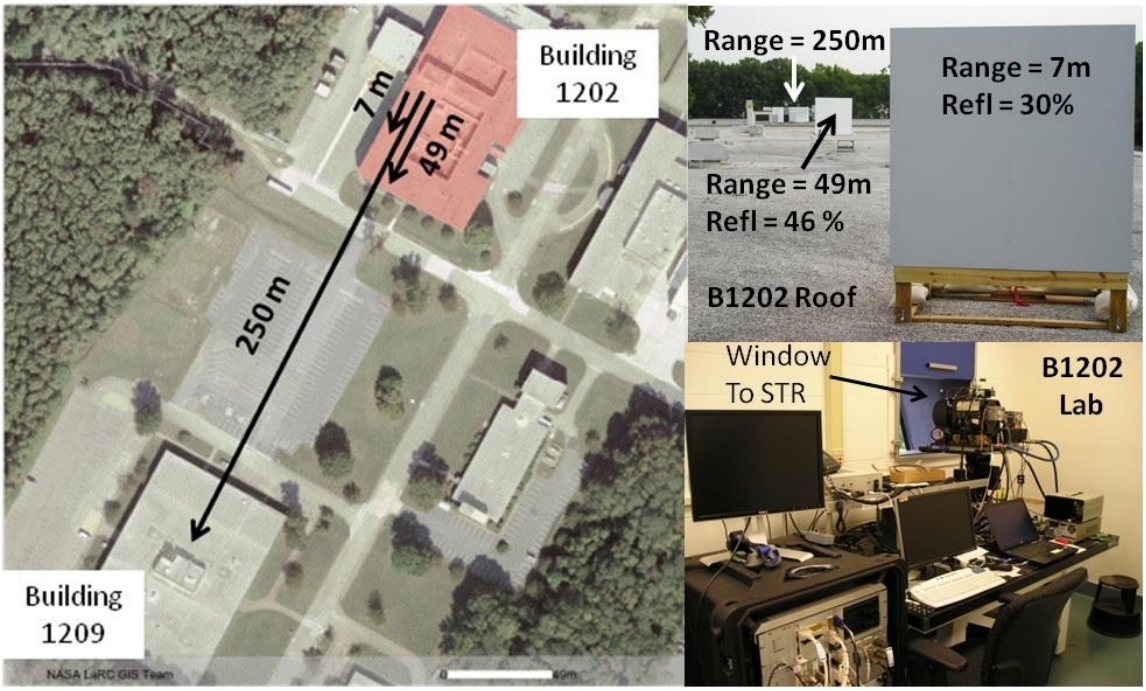

Figure 2.1: Sensor Test Range (STR) at NASA-LaRC for experimental lidar development and test. The lab with window opening to the STR is shown in the lower right. The view from lab firing window is shown in the upper right with the three targets which are available for imaging along with the range and reflectivity of each target. An overhead view of the STR is shown on left with ranges to various targets denoted.

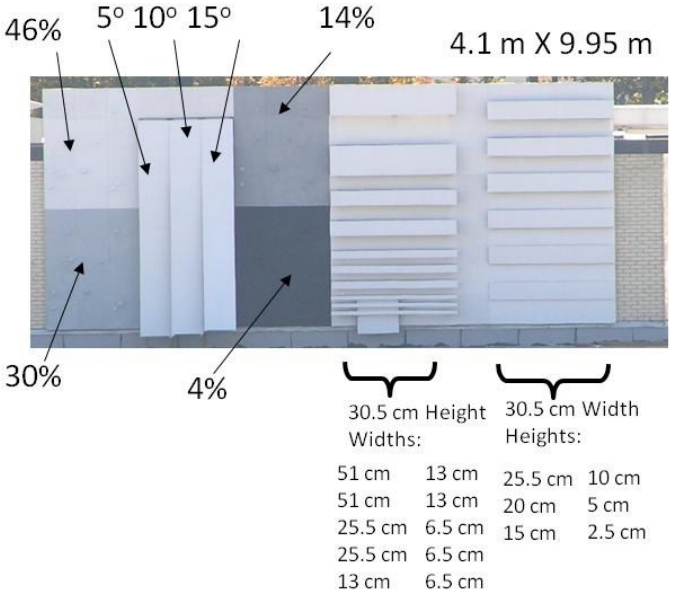

Figure 2.2: The STR target board at 250 m with target reflectivity values and sizes noted.

Figure 2.3: Fixed-FOV lidar (left) and var-FOV lidar (right) being characterized on the STR.

2.2 Flash Lidar Apparatus Configuration

2.2.1 Fixed-FOV Flash Lidar

The lab and flight configuration of the fixed-FOV lidar is presented. Figure 2.4 presents the fixed-FOV lidar sensor head which includes the laser head, the transmitter and receiver optics, the 3-D imaging camera all mounted on a liquid-cooled metallic plate. Table 2.1 presents the fixed-FOV lidar sensor head component descriptions including the laser, the turning mirrors, the beam expanding lenses, the beam shaping lens, the receiver optics, and the 3-D camera. The first turning mirror is used to adjust the beam to pass through the optic center of the beam expander and beam shaper. The beam expander is used in order to minimize

speckle as the beam passes through the beam shaper. The beam shaper adjusts the spatial profile of the beam into a top-hat at the desired divergence of one degree. The second turning mirror is used to align the exit beam with the receiver optics so that the detector is completely illuminated. The receiver optics are used to gather the back-scattered light and focus it onto the 3-D camera's FPA for recording of intensity and range. The solar filter is used to remove the solar background present at the detection wavelengths of the FPA so that the system performs independent of solar illumination state. The 1570 nm block window is simply used to mechanically protect the sensitive FPA from debris damage. Table 2.2 presents the supporting electronics, software, firmware, and mechanical key components and settings. A liquid chiller is used to pump coolant through tubes to cool the laser mounting plate and hence the laser. The camera receives preliminary notification of laser firing from the laser's Q-switch out TTL signal (the optical t0 is the one used for starting the range counting however). The power and data electronics used in lab testing are off-the-shelf or vendor-provided GSE equipment while the flight versions are LaRC custom which perform functionally the same. A slower frame rate is used in lab testing than flight to minimize wear and tear on the laser and camera, although key testing is accomplished at the flight frame rate. The camera sensitivity setting is delineated. The camera's correction firmware information is presented. The aerodynamic shroud (used to protect the lidar from the free-stream air during flight), is used for the flight testing but is not ready in its final state for evaluation in the lab testing.

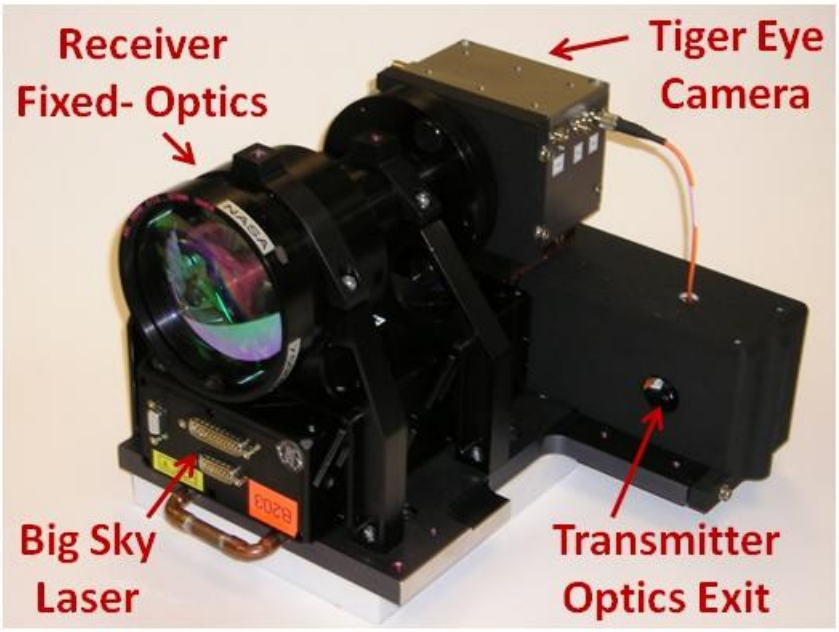

Figure 2.4: Fixed-FOV lidar sensor head containing the Big Sky laser head, the transmitter optics, the receiver optics, and the 3-D imaging camera along with optics dust cover all mounted on a liquid-cooled metallic plate.

Table 2.1: Fixed-FOV lidar sensor head component descriptions.

Transmitter		Receiver	
Item	Description	Item	Description
Laser	Big Sky	Lens	ASC 750mm f/7.5 1570 nm
Turn mirror 1 (1")	CVI Y1-1025-45-D	Corrector lens (to 1°, 730mm)	Thor Labs -50mm, plano-concave
Beam expander, 5x	Thor Labs BE05M	Solar filter	Edmund Optics IR-80 Long Pass (800 nm) 25.4mm
Beam shaper	Holo OR TH013IYA	1570nm block window	ASC custom
Turn mirror 2 (1")	CVI Y1-1025-45-D	Camera	ASC Tiger Eye #1005
Dust covers	LaRC custom	-	-

Table 2.2: Fixed-FOV lidar electronics, software, firmware, and mechanical components and key settings.

Electronics/Software/Firmware/Mechanical	
Item	Description
Laser chiller	Thermo Tek Inc Model RC3-2-32MS
Cam elect flash in	Big Sky Q-switch out
Power and data electronics	GSE (lab), LaRC custom (flight)
Frame rate	10 Hz (20 Hz flight)
Camera sensitivity setting	Maximum
Data acquisition and control	ASC Flash3D (lab), LaRC custom (flight)
Range / intensity cal in f/w	ASC calibrations
Support structure	LaRC custom
Aerodynamic shroud	Lab (none), LaRC custom (flight)

2.2.2 Var-FOV Flash Lidar

The lab and flight configuration of the var-FOV lidar is presented. Figure 2.5 presents the var-FOV lidar sensor head which includes the laser head, the transmitter and receiver optics, the 3-D imaging camera all mounted on a liquid-cooled metallic plate. Table 2.3 presents the var-FOV lidar sensor head component descriptions including the laser, the turning mirrors, the beam expanding lenses, the receiver optics, and the 3-D camera. The first and second turning mirrors are used to adjust the beam to pass through the optic center of the three beam expanding lenses. Two of the three beam expanding lenses rest on a linear zoom motor stage so that lens separation is adjusted to achieve the span of desired beam divergence

angles. The third turning mirror is used to align the exit beam with the receiver optics so that the detector is completely illuminated. The receiver optics are used to gather the back-scattered light and focus it onto the 3-D camera's FPA for recording of intensity and range. Two of the four compound receiver lens element groups internal to the zoom lens are translated by a linear motor to set full range of receiver zoom angles. The solar filter is used to remove the solar background present at the detection wavelengths of the FPA so that the system performs independent of solar illumination state. The 1570 nm block window is simply used to mechanically protect the sensitive FPA from debris damage. Table 2.4 presents the supporting electronics, software, firmware, and mechanical key components and settings. A liquid chiller is used to pump coolant through tubes to cool the laser mounting plate and hence the laser. The camera receives preliminary notification of laser firing from the laser's t0 output differential signal (the optical t0 is the key one used to start range counting however). The power and data electronics used in lab testing are off-the-shelf or vendor-provided GSE equipment while the flight versions are LaRC-custom which perform functionally the same. A slower frame rate is used in lab testing than flight to minimize wear and tear on the laser and camera, although key testing is accomplished at the flight frame rate. The camera sensitivity setting is delineated. The camera's correction firmware information is presented. The aerodynamic shroud (used to protect the lidar from the free-stream air during flight) used is LaRC custom-built.

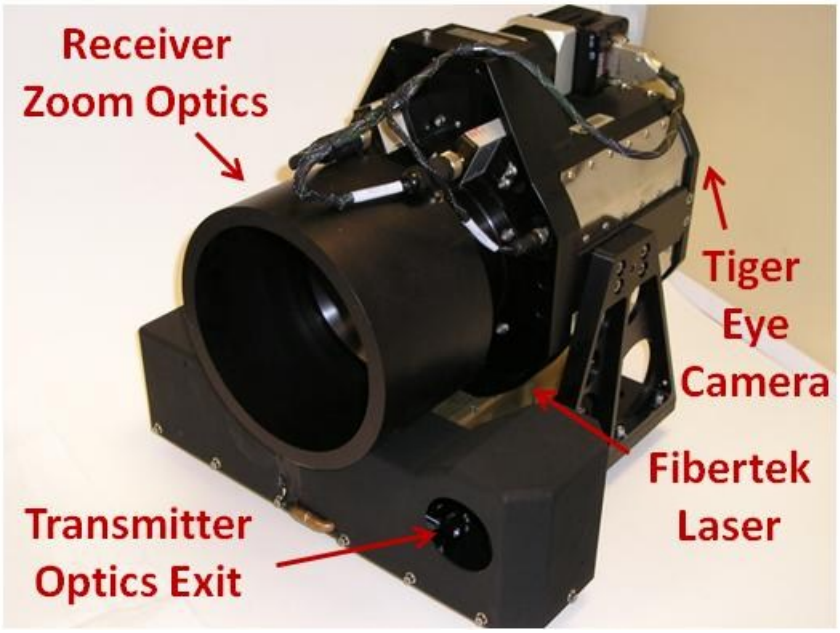

Figure 2.5: Var-FOV lidar sensor head containing the Fibertek laser head, the transmitter optics, the receiver optics, and the 3-D imaging camera along with optics dust cover all mounted on a liquid-cooled metallic plate.

Table 2.3: Var-FOV lidar sensor head component descriptions.

Transmitter		Receiver	
Item	Description	Item	Description
Laser	Fibertek	Turn mirror 3 (3")	CVI Y3-1025-45-D
Turn mirror 1 (1")	CVI Y1-1025-45-D	Dust covers	LaRC custom
Turn mirror 2 (1")	CVI Y1-1025-45-D	Lens	Ball Aerospace 6 to 24 deg zoom
Lens 1 (BEX)	CVI PLCC-10.0-10.3-C-1064	Solar filter	Edmund Optics IR-80 Long Pass (800 nm) 25.4mm
Lens 2 (BEX)	Newport KPC040AR.18	1570nm block window	ASC custom
Lens 3 (BEX)	CVI PLCX-50.8-91.2-C	Camera	ASC Tiger Eye #1004

Table 2.4: Var-FOV lidar electronics, software, firmware, and mechanical components and key settings.

Electronics/Software/Firmware/Mechanical	
Item	Description
Laser chiller	Thermo Tek Inc Model RC3-2-32MS
Cam elect flash in	Fibertek t0 output
Power and data electronics	GSE (lab), LaRC custom (flight)
Frame rate	10 Hz (20 Hz flight)
Camera sensitivity setting	Maximum
Data acquisition and control	ASC Flash3D (lab), LaRC custom (flight)
Range / intensity cal in f/w	ASC calibrations
Support structure	LaRC custom
Aerodynamic shroud	LaRC custom

2.2.3 Flash Lidar System Specifications

Table 2.5 lists key system specifications for the two flash lidars. They each operate at 1.064 μm. The fixed-FOV has higher spatial precision as evidenced by its lower FOV with the same number of pixels resulting in a smaller GSD (GSD is effectively the ground footprint of one pixel at maximum range). The ground footprints of each lidar are shown (using 6 deg for the var-FOV lidar since that is its planned FOV at maximum range). Although the var-FOV lidar has a larger aperture, most of its aperture is unused due to the relatively small focal lengths and its small, constant f/# of 2.5. The beam divergence for each lidar matches its receiver FOV for full FPA illumination. The pulse energy of the var-FOV lidar is over 2/3 stronger than that of the fixed-FOV since the laser used for the var-FOV is the planned space laser. Although the var-FOV lidar's laser is more powerful, the two lidars have comparable, tiny pulse widths on the order of

nanoseconds (critical for range precision) and video-compatible frame rates. Both lidars utilize the same 3-D camera technology and, hence, utilize the same size detector array. The same data acquisition system and support electronics are used for both lidars (16 bit range and 8 bit intensity representation) which means that on a given flight only one lidar is operated at a time.

Table 2.5: Flash lidar system specifications.

Parameter	Fixed-FOV Flash Lidar	Var-FOV Flash Lidar
Wavelength	1.064 µm	1.064 µm
Receiver lens FOV	1.00 deg	6.0 to 24.0 deg
Focal length	730 mm	45 to 120 mm
Ground footprint of planned FOV (at max range)	17 x 17 m	105 x 105 m
GSD (min) at max range	14 cm	82 cm
Aperture (full objective lens)	100 mm	125 mm
f/#	7.3	2.5 (constant during zoom)
Beam divergence	26 mrad	105 to 280 mrad
Pulse energy (Ep)	30 mJ	50 mJ
Pulse width	8 ns	8 ns
Frame rate	30 Hz	30 Hz
Number of pixels	128 x 128	128 x 128
Flight data acquisition # range bits	16	16
Flight data acq. range max / min recordable	0 to 1310 m	0 to 1310 m
Flight data acquisition # intensity bits	8	8
Flight data acq. intensity max / min recordable	0 to 4096 counts	0 to 4096 counts

2.3 Maximum Operational Range Estimation, Fixed-FOV Lidar

2.3.1 Objective

The objective is to estimate the maximum operational range which will be achieved in flight for the fixed-FOV lidar.

2.3.2 Apparatus

The fixed-FOV lidar (configuration defined at start of the lab characterization sub-section section, with test-dependent items specified in the present section) is focused at infinity and set to image the white (46% reflectivity), flat, 1.98 m x 1.98 m target board set at 49 m on the STR. The 1 inch round ND filter set is used. The camera is operated at maximum camera sensitivity. No aerodynamic shroud is installed since the mechanical development is on-going (planned for final evaluation during integration with instrumentation pod and helicopter).

2.3.3 Techniques

The target board of known reflectivity is imaged at zero incidence since reflectivity is a cosine function of incidence with zero incidence yielding maximum reflectivity. The target board is imaged at successive OD values, using a set of ND filters calibrated at the laser wavelength, to effectively attenuate the laser output until no backscatter signal intensity is observed. During the data reduction and analysis phase, the OD values are traded for effective range to estimate the maximum effective operating range that should be seen in flight. The technique for equating attenuation by OD with attenuation due to longer range is necessary since the actual flight ranges cannot be achieved within the STR which is limited to 250m. Based on the known reflectivity value and known incidence angle, data can later be adjusted to more closely match the test site target reflectivity and the imaging angle at a particular point in the trajectory. The camera sensitivity is set at its maximum while still suppressing extraneous backscatter so that no pixels are pre-triggered falsely. Transmitter and receiver optics are the flight articles so that reflection and bulk absorption losses are indicative of those to be seen in flight. Note that several pixels of defocus result from the receiver optics' infinity focus setting

(depth of field reaches back to 364m); however, maximum range estimation on a flat board of uniform reflectivity is not affected by minor defocus. Laser divergence angle and receiver FOV are those to be used in flight, since mis-match between them can be used to artificially amplify or attenuate the reported intensities. The laser divergence settled upon overfills the receiver FOV by approximately 8 milli-radians to provide robustness against any misalignments which may occur as a result of the flight vibration and shock environment such that even if shifts occur, all pixels will continue to be illuminated since the beam is considerably larger than the receiver FOV. The mosaic technique which is to be evaluated using the fixed-FOV lidar is sensitive to the loss of pixels in the FOV due to such misalignments as the mosaic technique relies on stitching together of multiple lidar images and hence relies on each image yielding a maximum of illuminated pixels. The transmitter and receiver optics are aligned for flight so that the beam is used most efficiently, thus yielding the maximum operating range. The laser is held within its normal thermal operating range using the active, liquid cooling system for a pulse energy output of 31.3 mJ at the laser output coupler and for a pulse energy output of 23.6 mJ past the last transmitter optic.

2.3.4 Results and Discussion

The technique for estimating maximum range in which attenuation due to application of OD is equivalent to attenuation due to longer theoretical target ranges (which reduce intensity through beam spreading) is based upon the following equations:

$$I = \frac{P}{A} \tag{2.1}$$

where

$$A = \pi r^2 \tag{2.2}$$

with $$r = R\frac{\theta}{2} \quad (2.3)$$

and $$\frac{P_2}{P_1} = 10^{-OD} \quad (2.4)$$

Thus, if I_1 is attenuated by increased theoretical range R_1 and if I_2 is attenuated by application of OD at near range R_2, what value of R_1 will make the two reduced intensities equivalent?

$$I_1 = I_2 \quad (2.5)$$

so $$\frac{P_1}{\pi\left(\frac{R_1\theta}{2}\right)^2} = \frac{P_1 10^{-OD}}{\pi\left(\frac{R_2\theta}{2}\right)^2} \quad (2.6)$$

thus $$R_1 = R_2\sqrt{10^{OD}} \quad (2.7)$$

where R_2 is the actual target board range, R_1 is the theoretical range that can be seen in flight, and OD is the maximum OD value for which ranging is still possible.

The criterion for establishing maximum range is application dependent. The criterion applied in the present case is that greater than 90% of the pixels should trigger at the OD test point designated as the maximum operating range condition, with maximum range being that condition at which only approximately 90% of the pixels trigger. Figure 2.6 shows a plot of the percentage of triggered pixels as a function of OD for images taken of the STR target at an actual range of 49m. Recall that the detector array contains 16384 pixels in an array of 128 by 128. Figure 2.7 shows the variation of median intensity with OD.

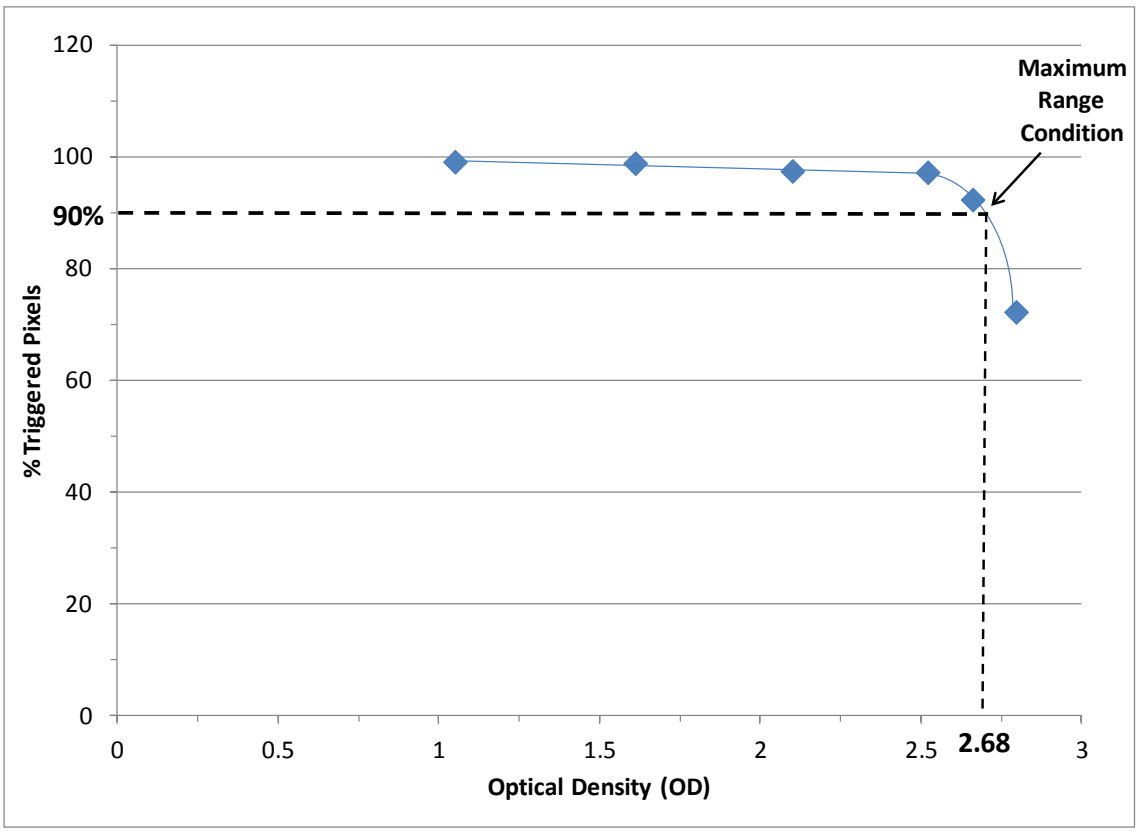

Figure 2.6: Maximum operating range estimated to be 1070 m for fixed-FOV lidar identified at 90% triggered pixels level for OD = 2.68 for images taken of STR target (46% reflectivity) at actual range of 49m.

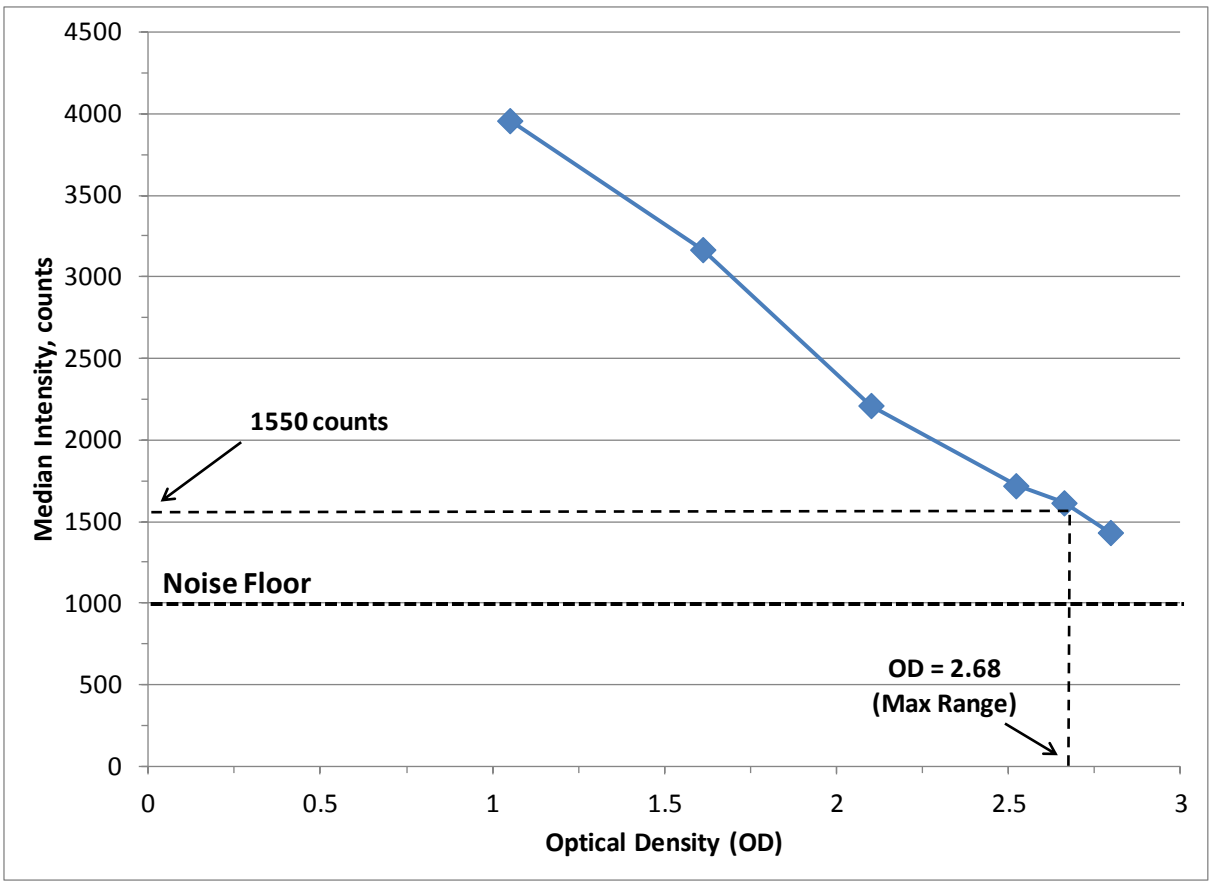

Figure 2.7: Median intensity drop as function of OD for images of STR target board (46% reflectivity) at 49m by fixed-FOV lidar with median intensity at maximum range condition identified at an OD of 2.68 yielding a signal-noise ratio of 1.5.

Based upon Figure 2.6, the number of triggered pixels for an OD value of 2.68 is 90%. Figure 2.7 shows median intensity at the maximum range OD to be approximately 1550 intensity counts which yields a sign-to-noise ratio of approximately 1.5. The maximum range is estimated to be 1070 m based on the OD of 2.68 from imaging the STR target board at an actual range of 49m utilizing equation 2.7. Figures 2.8 and 2.9 present the intensity and range image contour plots of the target at 49m for the closest OD case that is at or above the maximum-range OD value of 2.68 which turns out to be the OD case of 2.80. The contour plots of Figures 2.8 and 2.9 show pixel number on the x and y axes (128 pixels on each axis) with Figure 2.8 depicting intensity in

counts as the contour variable (with noise floor at 1000 counts and the upper limit at 4096 counts) and with Figure 2.9 depicting range in meters as its contour variable. Figure 2.8 shows that most pixels are triggered and yield intensity data in the vicinity of 1500 counts which is above the noise floor of 1000 counts to provide enough signal-noise ratio from which to develop a proper range solution. Figure 2.9 shows that, indeed, precise range values are generated around 54.2 meters. Figure 2.9 indicates that the actual range to the target is approximately 54 m instead of 49 m which is due to range accuracy biasing that is not critical for the hazard detection objective of the present development and field test cycle, as the hazard detection objective relies on range precision not range accuracy (range accuracy is to be provided by the ALHAT navigation filter).

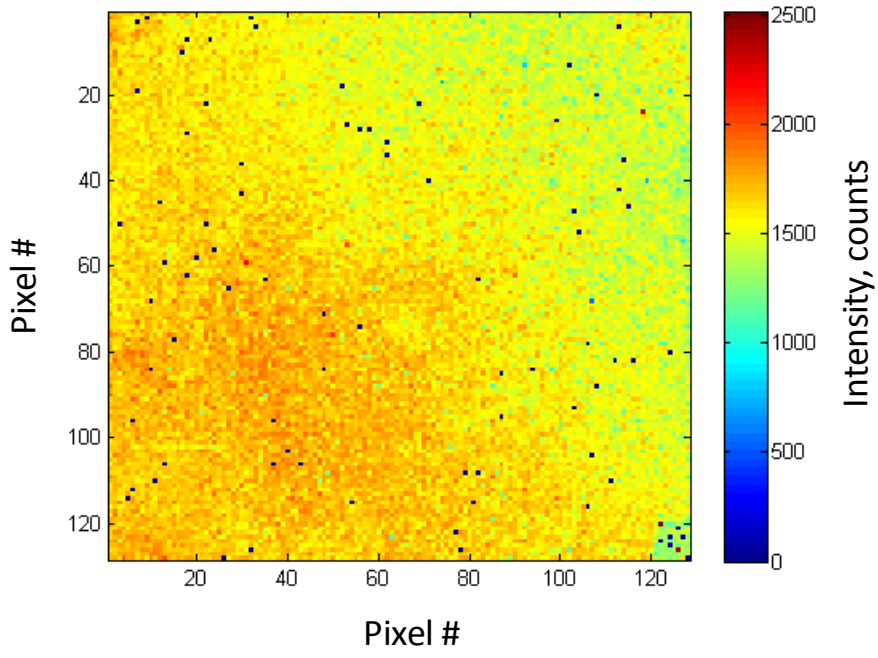

Figure 2.8: Intensity contour plot of 49 m target board (46% reflectivity) for fixed-FOV lidar at OD = 2.80 which is the nearest contour plot which is at or above the maximum operational range case.

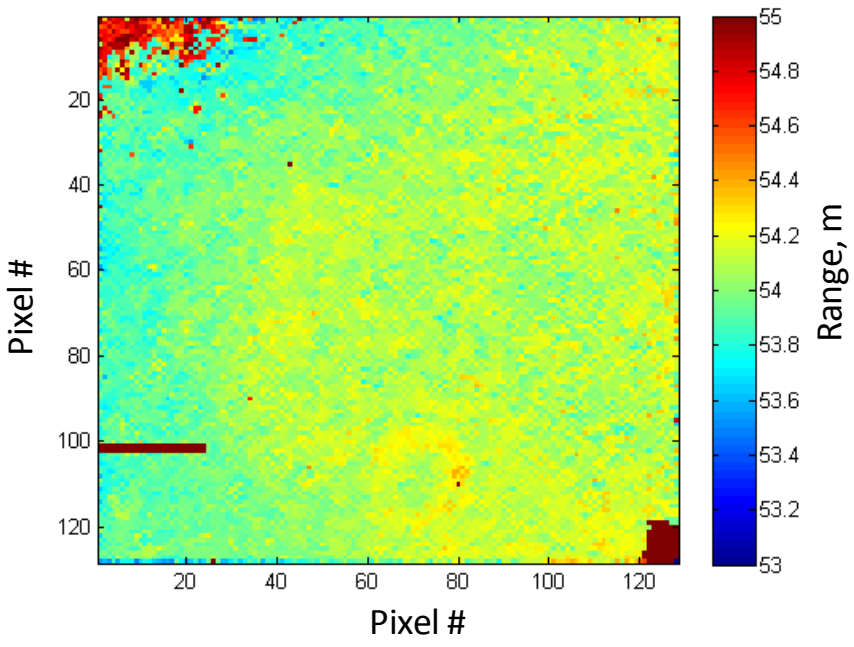

Figure 2.9: Range contour plot of 49 m target board (46% reflectivity) for fixed-FOV lidar at OD = 2.80 which is the nearest contour plot which is at or above the maximum operational range case.

2.4 Maximum Operational Range Estimation, Var-FOV Lidar

2.4.1 Objective

The objective is to estimate the maximum operational range which will be achieved in flight for the var-FOV lidar.

2.4.2 Apparatus

The var-FOV lidar (configuration defined at start of the lab characterization sub-section, with test-dependent items specified in the present section) is set to image the white (46% reflectivity), flat, 1.98 m x 1.98 m target board set at 49 m on the STR. The focus is set to

infinity such that the worst case depth of field extends back to 37m. The transmitter and receiver optics are set for FOV's of 6°, 7.5°, 10.6°, and 13.5°. The four inch square ND filter set is used. The camera is operated at maximum sensitivity. No aerodynamic shroud is installed since the mechanical development is on-going (planned for final evaluation during integration with instrumentation pod and helicopter).

2.4.3 Techniques

The target board of known reflectivity is imaged at zero incidence since reflectivity is a cosine function of incidence with zero incidence yielding maximum reflectivity. The target board is imaged at successive OD values, using a set of ND filters calibrated at the laser wavelength, to effectively attenuate the laser output until no backscatter signal intensity is observed. During the data reduction and analysis phase, the OD values are traded for effective range to estimate the maximum effective operating range that should be seen in flight. The technique for equating attenuation by OD with attenuation due to longer range is necessary since the actual flight ranges cannot be achieved within the STR which is limited to 250m. Based on the known reflectivity value and known incidence angle, data can later be adjusted to more closely match the test site target reflectivity and the imaging angle at a particular point in the trajectory. The camera sensitivity is set at its maximum while still suppressing extraneous backscatter so that no pixels are pre-triggered falsely. Transmitter and receiver optics are the flight articles so that reflection and bulk absorption losses are indicative of those to be seen in flight. The laser divergence angle and the receiver FOV are matched at each setting, as they will be in flight, since mismatch between transmit and receive optics can be used to artificially amplify or attenuate the reported intensities. The transmitter and receiver optics are aligned for

flight so that the beam is used most efficiently, thus yielding the maximum operating range. The laser is held within its normal thermal operating range using the active, liquid cooling system for a pulse energy output of 50 mJ at the laser output coupler.

2.4.4 Results and Discussion

The technique for estimating maximum range in which attenuation due to application of OD is equivalent to attenuation due to longer theoretical target ranges (which reduce intensity through beam spreading) is based upon the equations previously presented and discussed in the section on maximum operational range estimation for the fixed-FOV lidar. The criterion for establishing maximum range is application dependent. The usual rule applied in flash lidar testing is that greater than 90% of the pixels should trigger at the OD test point, however, due to the wide FOV's of the var-FOV lidar, only a subset of the FOV can be tested. The maximum range for the var-FOV lidar is considerable larger than the goals for FT 4 and larger than the maximum value which can be represented by the LaRC flight software. Thus, the conservative criteria for determining maximum range selected for the present case are that all pixels representing the range target should be illuminated for all FOV settings at a signal to noise value of 1.3 or greater. The stipulation that the criteria be satisfied for all FOV's arises from the constant f/# at which the receiver zoom optics operates. Since the f/# is held constant through all FOV's (i.e. focal lengths), then the aperture is reduced at successively larger FOV's (smaller focal lengths) and, since lens throughput is dominated by aperture, the intensity for the same OD's at larger and larger FOV's will be reduced. Based upon the conservative maximum range criteria, the maximum range is determined to be 1600 m. Figures 2.10 and 2.11 present intensity and range image contour plots of the target at 49m for the 6° FOV case at the maximum range

OD value of 3.05. The contour plots of Figures 2.10 and 2.11 show pixel number on the x and y axes (128 pixels on each axis) with Figure 2.10 depicting intensity in intensity counts as the contour variable (with noise floor at 1000 counts and the upper limit at 4096 counts) and with Figure 2.11 depicting range in meters as its contour variable. Figure 2.10 shows that most (> 90% certainly) are triggered and yield intensity data in the range of 2100 counts which is well above the noise floor of 1000 counts to provide enough signal-noise ratio from which to develop a proper range solution. Figure 2.11 shows that, indeed, precise range values are generated around 48.7 meters.

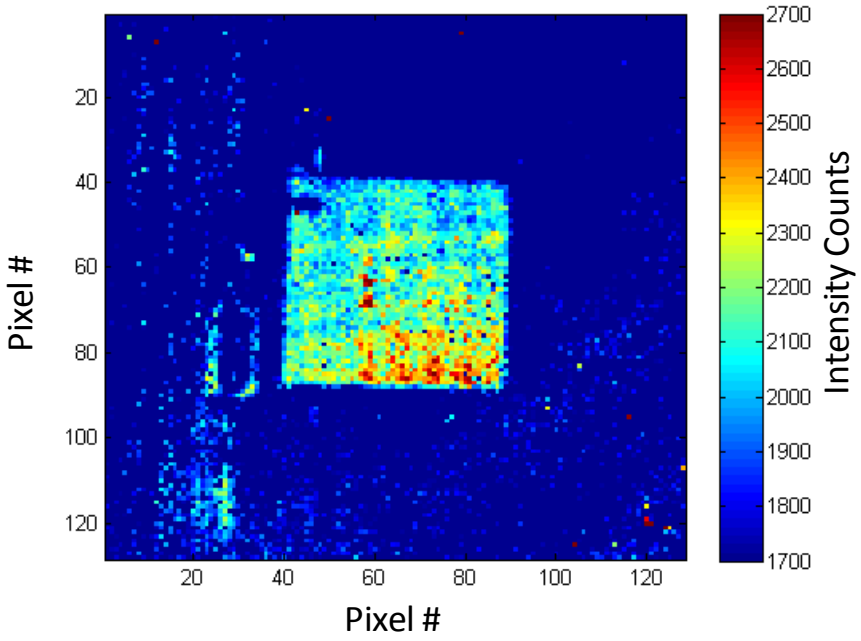

Figure 2.10: Intensity contour plot of 49 m target board (46% reflectivity) at 6° FOV for var-FOV lidar at OD = 3.05.

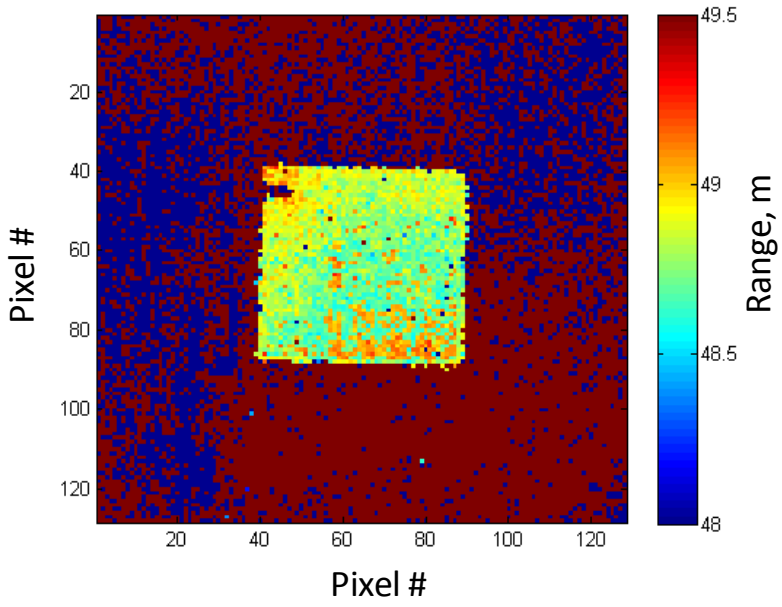

Figure 2.11: Range contour plot of 49 m target board (46% reflectivity) at 6° FOV for var-FOV lidar at OD = 3.05 equating to projected maximum range of 1600 m.

2.5 Range Precision Estimation, Fixed-FOV Lidar

2.5.1 Objective

The objective is to determine the range precision for the fixed-FOV lidar after applying corrections based on the range / intensity calibration procedure. In addition to acquiring data for the camera manufacturer's (ASC's) range / intensity correction procedure and applying those coefficients for evaluation of range precision, also acquire data for and evaluate a LaRC custom range / intensity correction method.

2.5.2 Apparatus

The fixed-FOV lidar (configuration defined at start of the lab characterization sub-section section, with test-dependent items specified in the present section) is focused at infinity and set to image the white, flat, 1.98 m x 1.98 m target board set at 49 m on the STR. The 1 inch round ND filter set is used. The camera is operated at maximum sensitivity. No aerodynamic shroud is installed since the mechanical development is on-going (planned for final evaluation during integration with instrumentation pod and helicopter). The apparatus for each of the inter-related experiments for developing the range / intensity correction coefficients (both the ASC method and the LaRC method) and then evaluating them for range precision are functionally identical.

2.5.3 Techniques

The range / intensity calibration technique is based on the notion that if the detector array (i.e. all pixels) is uniformly illuminated by backscatter from a flat target board (see the apparatus section for target board description and range) which is oriented normal to the beam / detector array, then all pixels within a given frame of data should output the same value of range and any differences are due to the range / intensity phase shift phenomenon described in the flash lidar operating principles sections. Thus the calibration data set is acquired by imaging a flat, uniform (in reflectivity), diffusely reflecting target board at zero incidence over a range of ND filters which effectively vary the laser output power to yield range / intensity data at various intensity amplitudes. Data is taken primarily over the linear region of camera operations, but some data is taken into the saturation region for completeness, although, in the saturation realm, range / intensity corrections lose their meaning since the signal is distorted due to the dynamic range limits of the instrument. The reason for setting the flat target board to be imaged at zero

incidence is that the assumption that all pixel ranges should output the same value (with the only difference being due to the range / intensity phenomenon being calibrated) does not hold since the board slope with respect to the flash lidar introduces a range bias. Figure 2.12 illustrates the offset which is quantified by equation 2.8.

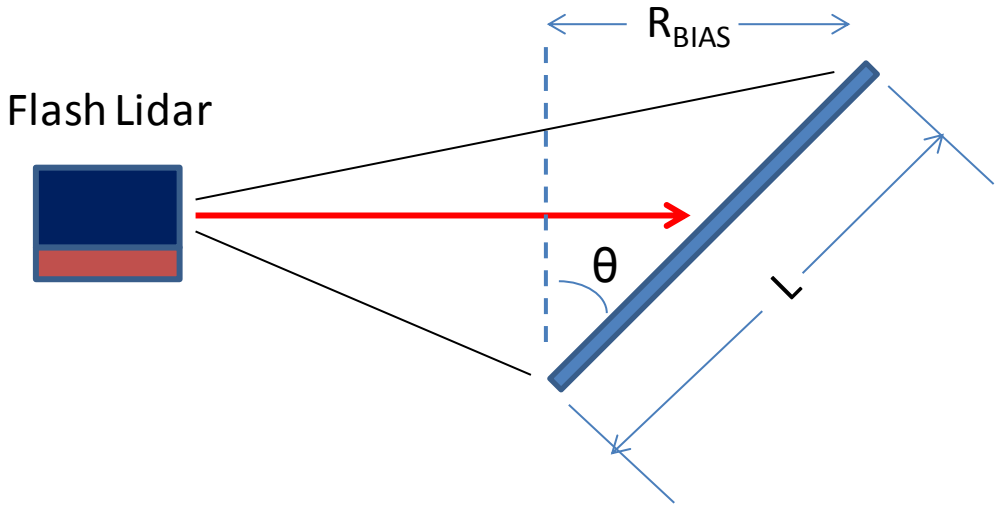

Figure 2.12: Undesirable mechanical range bias introduced by non-zero incidence flat target board which couples to amplifier-phase-response-caused range bias during range / intensity calibrations (shown only in one axis for simplicity).

$$R_{BIAS} = L\sin(\theta) \tag{2.8}$$

The flat target board is set to zero incidence using a bi-statically mounted, co-aligned visible laser (a Helium-Neon laser which is referred to as a HeNe) on the flash lidar setup. The target board is then moved in lateral and vertical rotations until the alignment beam folds back on itself indicating zero incidence. The roll rotation has no effect on incidence angle. Sharp focus is not a requirement during the calibration due to the flat requirement on the target board and since the target board completely fills the detector array. The wavelength of the laser pulse used in calibration does not need to be the same as that planned for later use, as long as the wavelength

can be sensed by the flash lidar sensor (i.e. within the detector's sensing bandwidth and not filtered out by some optical component).

Some additional attention must be paid to camera set-up and operations during range / intensity calibration operations. The camera sensitivity must be set as high as possible so that calibration data can be acquired down to approximately zero intensity amplitude so that the calibration will be valid over the complete range of possible camera operations. If the experimental setup is not clean and instead allows stray beam returns which may be detected by the camera, then the pixels stuck will trigger prematurely (pre-trigger) before the backscatter from the target board reaches that pixel (and once a pixel triggers, it cannot be triggered again until the next frame of data, thereby ruining that frame of calibration data for that particular pixel) which will require lower sensitivity settings to prevent pre-triggering which will preclude the acquisition of data down to low intensities. Periodically during the calibration a non-uniformity correction must be made to ensure that all pixels respond with similar intensities to a given dose of photons. One chief source of non-uniformity is dark-current error which is induced by the applied reverse bias voltage on the APD detector and thermal electrons which adds to the current due to photo-electrons so that the detection scheme outputs a false response to a given dose of photons since some of the response arises from the dark current and will vary from pixel to pixel. Non-uniformity could corrupt the range / intensity calibration or post-calibration testing of correction coefficients since intensity amplitudes could be offset falsely resulting in intensity-dependent range shifts which are not due to backscatter from the target of interest but instead influenced by the thermal state of the FPA.

The test procedures used to evaluate a given range / intensity calibration by estimating range precision are identical to those used to generate the calibrations, except that the

range/intensity calibration coefficients are applied to the results in order to make the corrections. In the case of the ASC coefficients, they are loaded into the camera's firmware for real-time application. In the case of the LaRC custom coefficients, they are applied in post-processing.

2.5.4 Results and Discussion

The range / intensity calibration is developed for each pixel so that all of the pixels in each single frame read the same range to the flat target board. In order to provide supporting illustrations for subsequent discussions of the data on which the calibration is based, several pieces of information are presented first. Figure 2.13 shows one intensity frame of the STR flat target board at an OD of 2.1 with pixel number being displayed on the horizontal and vertical axes and intensity (in counts) being displayed as the contour variable with the noise floor at 1000 counts. Figure 2.14 shows the histogram associated with the intensity contour plot with the bins being intensity in counts. Figure 2.15 shows the range image (or frame) which corresponds to the intensity frame of Figure 2.13 with pixel number on the horizontal and vertical axes and range in meters as the contour variable. Figure 2.16 shows the histogram associated with the range contour plot with the bins being range in meters. Figures 2.13 through 2.16 show intensity and range behavior at a medium OD value. Figures A.1 through A.8 in the appendix present intensity and range behavior at high and then low values of intensity. The Figures 2.13 through 2.16 show intensity and range for one test point.

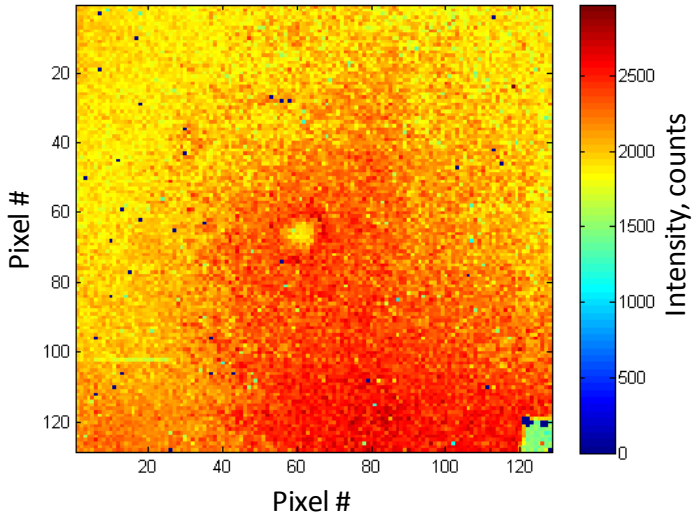

Figure 2.13: Intensity plot (at a medium intensity with most pixels in the linear region) of flat STR target board taken by the fixed-FOV lidar at OD = 2.1 during range / intensity calibrations.

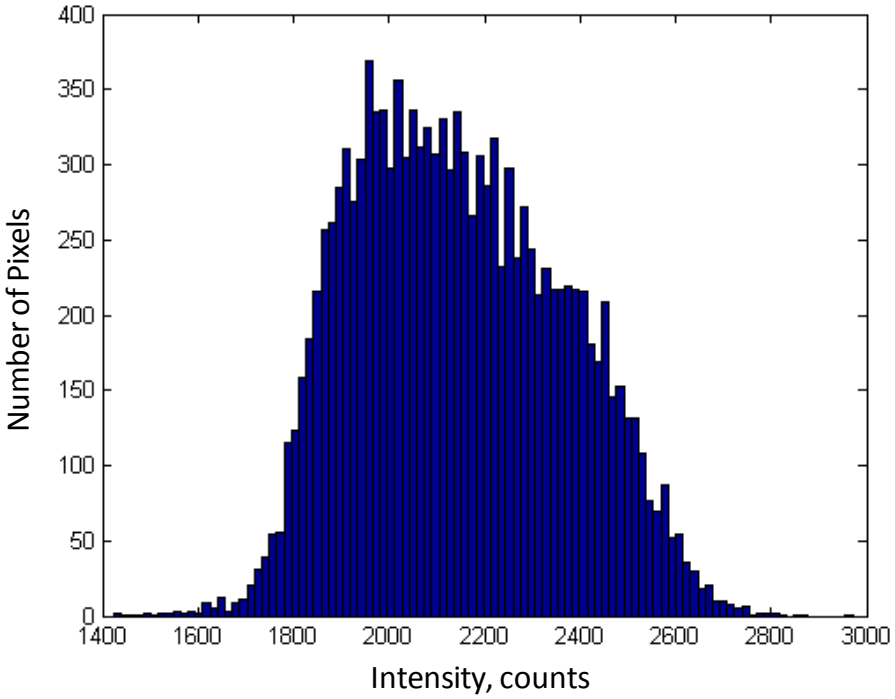

Figure 2.14: Histogram of intensity (at medium intensity with most pixels in the linear region) frame from fixed-FOV lidar at OD = 2.1.

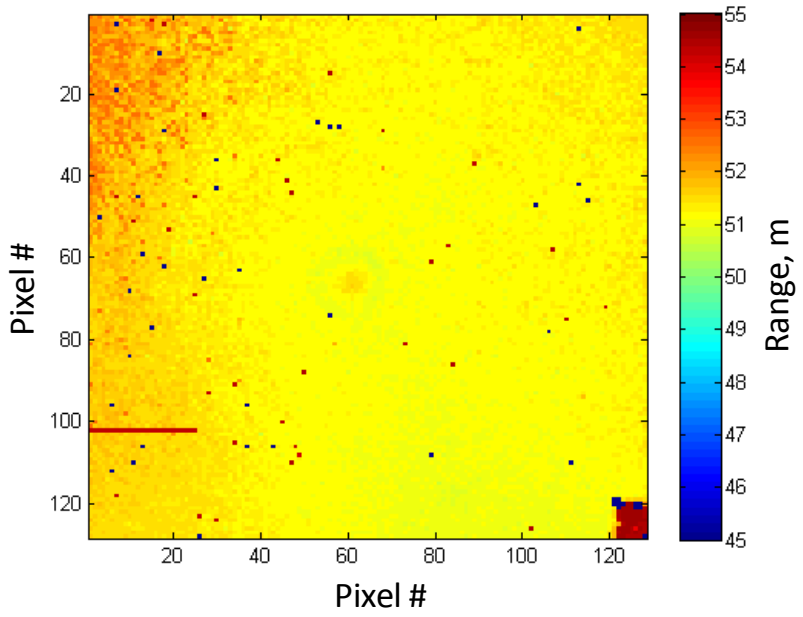

Figure 2.15: Range plot (at medium intensity case with most pixels in the linear region) of flat STR target board taken by fixed-FOV lidar at an OD = 2.1during range / intensity calibrations.

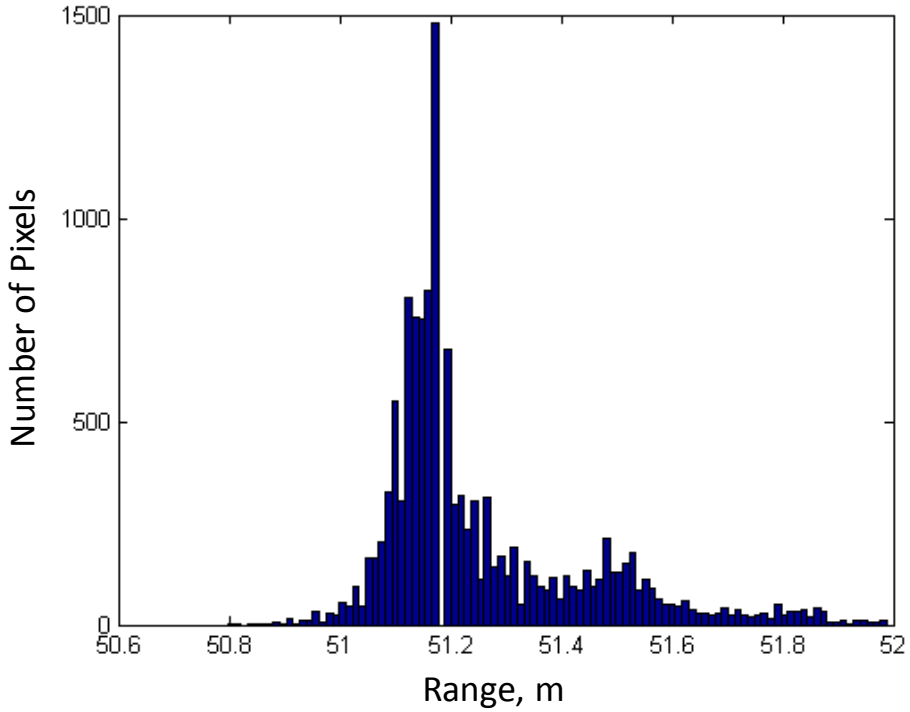

Figure 2.16: Histogram of range (at medium intensity case with most pixels in the linear region) from fixed-FOV lidar at OD = 2.1.

The range / intensity calibration does not address range accuracy and it is not applicable to all regions of sensor operation. The ultimate purpose of developing and applying the range / intensity calibration is to improve the range precision of the flash lidar, i.e. to make all pixels respond the same and to produce the same output when the same physical phenomenon is sensed at each pixel, not necessarily to make the range at each pixel accurate. Only the non-saturated (or linear) region of operation is applicable to range / intensity calibrations (the saturation region, as discussed before, does not lend itself to range correction for precision improvement and is, thus, a region where the sensor is un-calibrated which means a larger uncertainty must be accepted for experiment operations in that realm, thus saturation is a region to be avoided). The 1000 to 2500 count range of linear operations represents the dynamic range of the sensor (from signal drop out where the pixels are not triggered to the point of signal saturation and loss of precision).

The above figures are used in order to illustrate the need for calibration. Figures 2.13 and 2.15 illustrate the precision problem being addressed. Figure 2.13 shows that the flat, uniform (diffuse with uniform reflectivity) target board is being illuminated in a non-perfect way by the transmitter optics (non-perfect top-hat beam spatial profile) such that the center portion of the target backscatters with higher intensity than the peripheral portions. Figure 2.15 illustrates the range solutions for all pixels which indicates that the board is not flat, even though it is known to be flat to better than the precision limit of the sensor, with the center portion showing a smaller range value than the periphery, i.e. the flat target board appears to be bent in 3-D in a way to look like a bump. The range histogram of Figure 2.16 confirms that the pixels do indicate a span of different range values (i.e. if the pixels were all perfectly precise, there would only be one bin

on the range histogram, with all pixels reporting the same range). Comparing Figure 2.13 and Figure 2.15, it is apparent that the bright portions (higher intensity) of the board in Figure 2.13 appear closer (shorter range) in Figure 2.15 and vice versa for the dimmer (lower intensity) portions.

Not all 16,384 pixels respond properly in general and not all yield a successful calibration. Some pixels have detectors which are damaged and thus which generate no correction coefficients, while other pixels respond, but not correctly and thus yield calibrations which do not pass quality tests. Some pixels are bad by design since they are utilized for other purposes. Figure 2.17 is a map of the pixels which do not have usable range / intensity calibrations from ASC based on LaRC data for the fixed-FOV lidar which is used in the operational flight experiments to exclude bad pixel data. Figure 2.17 indicates 188 bad pixels which is 1.1% of the total number of available pixels.

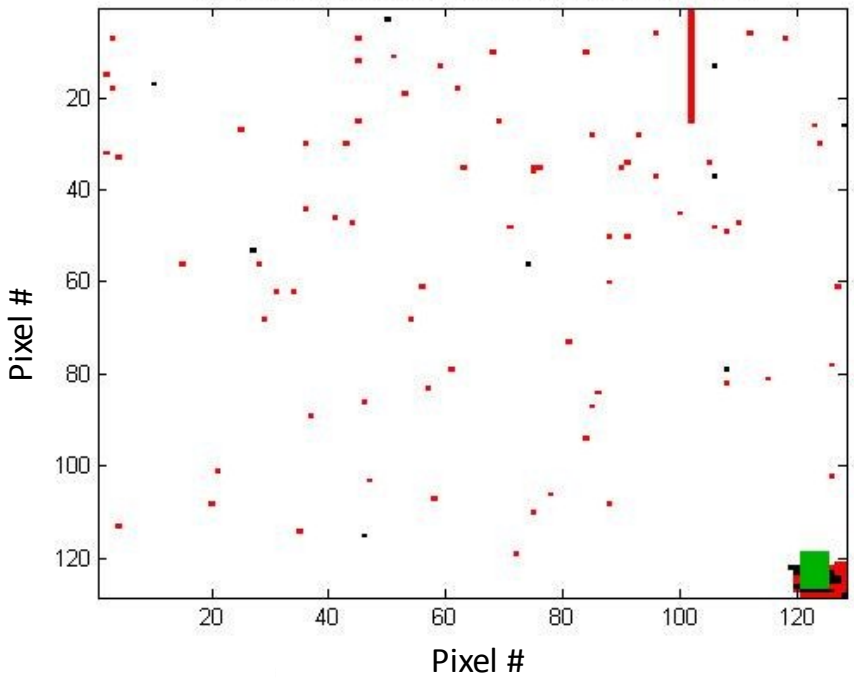

Figure 2.17: Map of the pixels without usable range / intensity calibration corrections from ASC based on LaRC data for the fixed-FOV lidar (black = pixels with no calibration due to non-response = 25, red = pixels with a bad calibration = 123, and green = pixels devoted to other purposes thus not usable for ranging = 40 for a grand total of 188 pixels not usable for ranging).

Since the range / intensity calibration is in place, the range precision can be estimated. As already discussed in the techniques section, the procedure for acquiring data to evaluate range precision is identical to that used to acquire data for development of the calibration except that the range / intensity coefficients are applied either in post-processing after the test (in the case of the experimental, higher-performing LaRC coefficients being evaluated) or in real-time during the test (in the case of the ASC coefficients on-board the camera in firmware). Note that the ASC coefficients are the ones to be used in the present flight test (although efforts are underway to incorporate the higher-performing LaRC coefficients into firmware). Range precision is

quantified from the experimental data by calculating a range standard deviation for the entire range image at one particular OD and then repeating the analysis process over a span of OD's. In the case of data acquired on the STR, the target board is flat and normal to the lidar and thus no plane fitting is required ahead of the standard deviation calculation other than calculating a basic mean. The slight range vector magnitude differences between the center of the lidar FOV and the periphery are negligible compared with the precision being measured. The case numbers from the experiment are correlated to particular OD values in Table 2.6. Figure 2.18 compares the range precision before and after the LaRC calibration coefficients are applied. Figure 2.18 shows that in the planned, linear operation region, the eight centimeter range precision goal is met when the LaRC calibration is applied. Figure 2.18 also demonstrates that the range / intensity calibration makes a considerable difference in range precision with un-calibrated precision in the 20 to 30 cm realm and calibrated precision remaining at and below 8 cm.

Table 2.6: Test case number correlation with OD.

Case #	OD
1	0
2	0.561
3	1.05
4	1.611
5	2.1
6	2.521
7	2.375
8	2.431
9	2.661

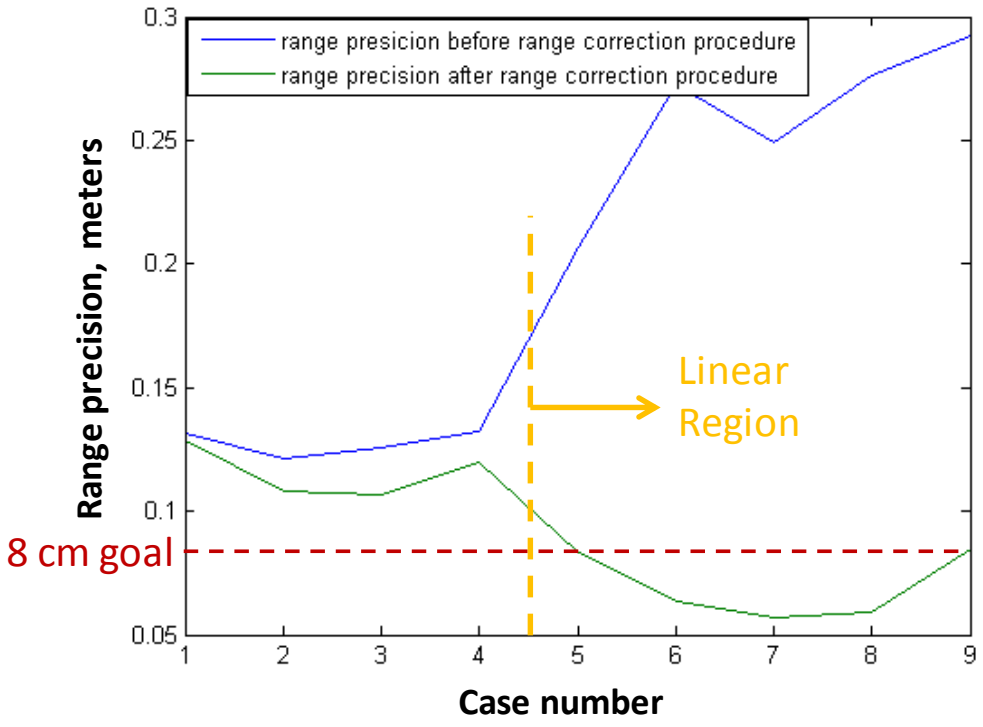

Figure 2.18: Range precision comparison before and after applying the LaRC range / intensity calibration for fixed-FOV lidar over a span of OD's on the flat STR target board showing that the 8 cm range precision goal is met in the planned, linear operating region.

Figures 2.19 through 2.22 illustrate the effect which the range / intensity calibration has on range precision in a single frame of data (i.e. peering into the case seven point on the Figure 2.18 curve in more detail). Figure 2.19 is a range contour plot for the case seven OD value for the flat STR target board before application of the range / intensity calibration. Note that the board, even though it is actually flat, appears curved due to the range / intensity effect. Figure 2.20 confirms the apparent curvature of the board as it is a range histogram which shows a spread of range values for various pixels that far exceeds the 8 cm precision goal. Figure 2.21 is a range contour plot at the same conditions as Figure 2.19 except that the LaRC range / intensity calibration has been applied. The apparent curvature of the board is gone. Figure 2.22, also after the range /

intensity calibration application, confirms the flatness of the board. Comparing Figure 2.20 (histogram before calibration is applied) with Figure 2.22 (histogram after calibration is applied) the concentration of the histogram about a smaller set of range bins is clear which means that the range precision is clearly improved by application of the LaRC range / intensity calibration. The comparison of Figures 2.20 and 2.22 also confirms the disparity in range precision numbers between un-calibrated and calibrated as shown in Figure 2.18 case seven.

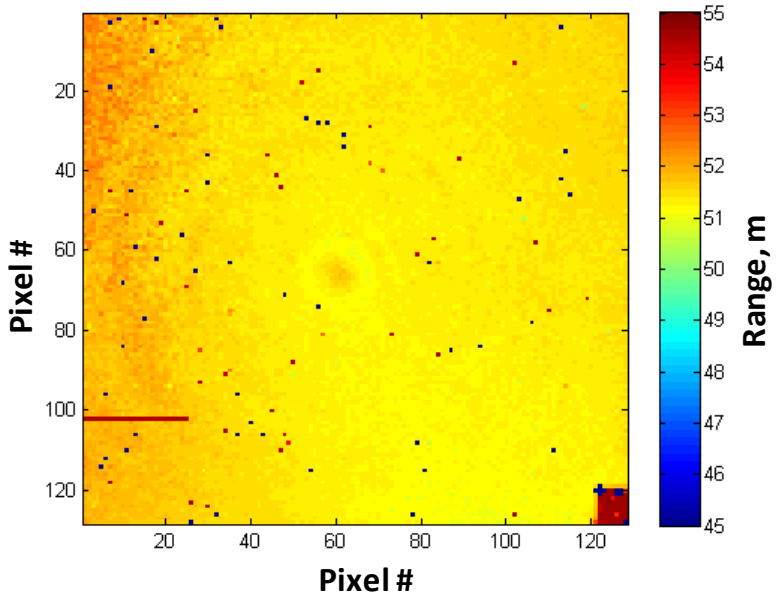

Figure 2.19: Range plot BEFORE application of range / intensity calibration; image taken of flat STR target board by fixed-FOV lidar at an OD = 2.375, case 7. Note that the curvature far exceeds the 8 cm precision goal.

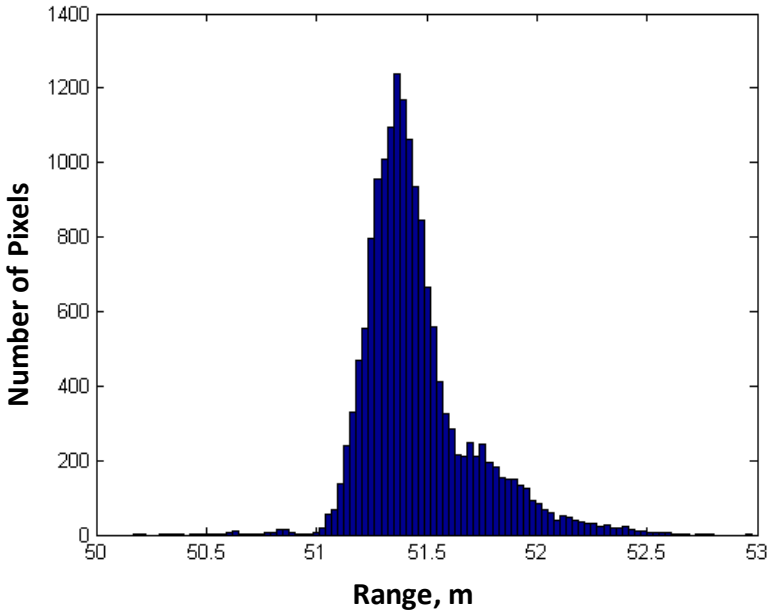

Figure 2.20: Histogram of range BEFORE application of range / intensity calibration; image taken of flat STR target board by fixed-FOV lidar at an OD = 2.375, case 7. Note the spread of ranges far exceeds the 8 cm precision goal.

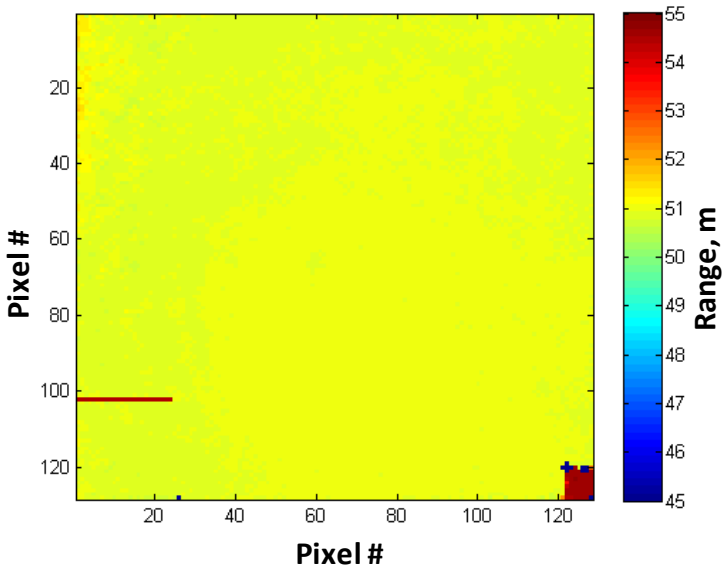

Figure 2.21: Range plot AFTER application of LaRC range / intensity calibration; image taken of flat STR target board by fixed-FOV lidar at an OD = 2.375, case 7. Board apparent curvature has been removed successfully.

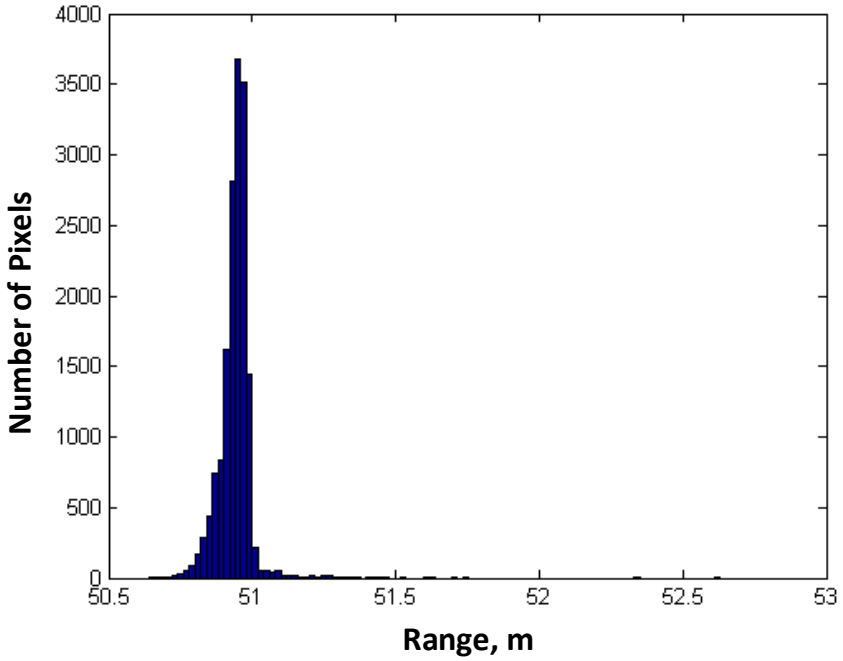

Figure 2.22: Histogram of range AFTER application of LaRC range / intensity calibration; image taken of flat STR target board by fixed-FOV lidar at an OD = 2.375, case 7. Note the spread of ranges has been concentrated to meet the 8 cm precision goal successfully.

The ASC range / intensity calibration also significantly improves range precision, but not quite as well as the LaRC curves. Figure 2.23 shows that in the planned, linear operation region, the eight centimeter range precision goal is marginally met when the ASC calibration is applied. The linear region starts at an OD of approximately 1.85 and extends to the maximum OD value shown in the plot. At the high intensity end of the linear range (lowest OD), the range precision just meets the 8 cm goal, but as intensity decreases (increasing OD), the range precision diverges away from the 8 cm goal. Even in the vicinity of the 2.6 OD value, the range precision of 12 cm is still considerably better than the un-calibrated precision shown in Figure 2.18 which extends to nearly 30 cm. The maximum range characterization indicates that flight operations should generally effectively fall below the OD of 2.6 level (i.e. intensities should be greater than those experienced at an OD of 2.6 at the 49 m board).

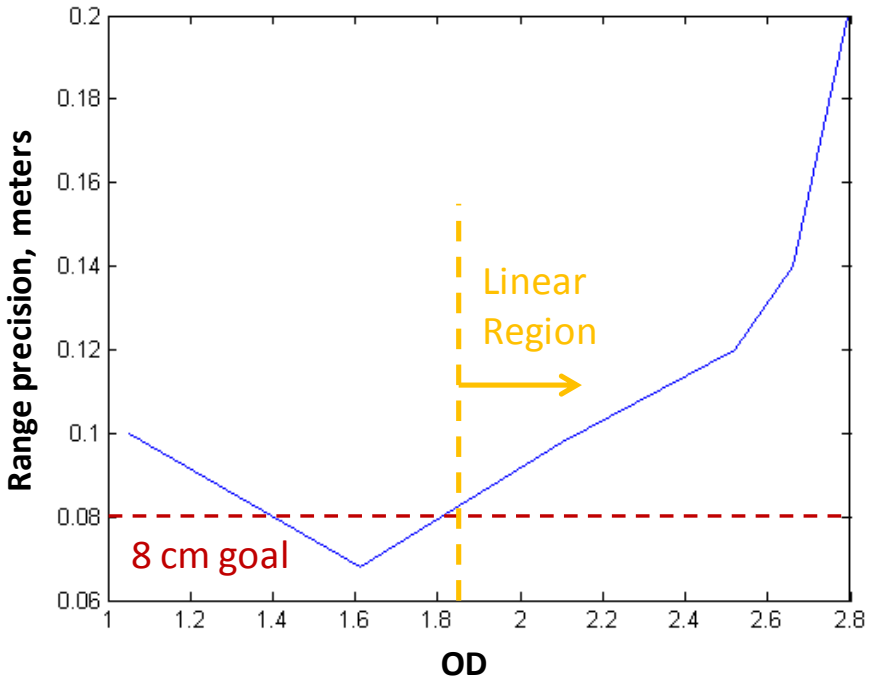

Figure 2.23: Range precision trend after applying the ASC range / intensity calibration for fixed-FOV lidar over a span of OD's on the flat STR target board showing that the 8 cm range precision goal is nearly met in the planned, linear operating region (the goal is met for the highest intensities i.e. lowest OD values in the linear region and then degrades more as the intensity decreases i.e. higher OD values).

An additional challenge with the ASC calibration, since it has a strong dependence on intensity, is that during flight the sensor will view real-world scenes which are not tightly controlled as in the lab environment. In real-world scenes, it is possible that within the same FOV, there will be surface reflectivities which vary enough that the intensity of adjacent objects will lie on each extreme end of the linear region of Figure 2.23 which means that the range precision may be low on one object and high on another which could introduce a false range variation between the two objects which may actually be flat and continuous. Despite its lower quality performance as compared to the new calibration being explored by LaRC, the ASC calibration is used for the flight tests since the camera firmware is currently written to accept it and has not been modified yet to accept the LaRC calibration as the LaRC calibration has only recently been under

development. Having the calibration reside in the Tiger Eye camera's firmware is critical to the flight tests since the calibrations are applied in real-time so that the sensor output is corrected in real-time and ready for use by the ALHAT hazard detection algorithms in flight.

2.6 Range Precision Estimation, Var-FOV Lidar

2.6.1 Objective

The objective is to determine the range precision for the var-FOV lidar after applying corrections based on the range / intensity calibration procedure. In addition to acquiring data for the camera manufacturer's (ASC's) range / intensity correction procedure and applying those coefficients for evaluation of range precision, also acquire data for and evaluate a LaRC custom range / intensity correction method.

2.6.2 Apparatus

The var-FOV lidar (configuration defined at start of the lab characterization sub-section section, with test-dependent items specified in the present section) is set to image the light gray, flat, 1.98 m x 1.98 m target board set at 7 m on the STR. The board is positioned close to the lidar so that at the wide FOV's of the var-FOV lidar, the beam can still be contained on the board. As a result of the close proximity between the target and lidar, the target board is slightly defocused (less than 9 pixels of defocus) which should have no effect on range / intensity calibration or precision estimation since the board is flat (no range information to smear) and the only setting changed between runs is the OD over the laser thus there should be no varying effect on either range or intensity. The four inch square ND filter set is used. The camera is operated

in at high sensitivity. No aerodynamic shroud is installed since the mechanical development is on-going (planned for final evaluation during integration with instrumentation pod and helicopter).

2.6.3 Techniques

The techniques applied for range / intensity calibration and subsequent quantification of range precision for the var-FOV lidar are identical to those already described for the fixed-FOV lidar.

2.6.4 Results and Discussion

Since the range precision estimation section for the fixed-FOV lidar has already covered much of the technique-specific results and discussion material, the present section on the var-FOV lidar will focus on data results only since the technique-specific discussions on range / intensity calibration and range precision estimation are generic to both lidars. In order to provide insight into the data on which the range / intensity calibration for the var-FOV lidar is based, several pieces of information are presented first. Figure 2.24 shows one intensity frame of the STR flat target board at an OD of 3.621 with pixel number being displayed on the horizontal and vertical axes and intensity (in counts) being displayed as the contour variable with the noise floor at 1000 counts. Figure 2.25 shows the histogram associated with the intensity contour plot with the bins being intensity in counts. Figure 2.26 shows the range image (or frame) which corresponds to the intensity frame of Figure 2.24 with pixel number on the horizontal and vertical axes and range in meters as the contour variable. Figure 2.27 shows the histogram associated with the range contour plot with the bins being range in meters. The Figures 2.24

through 2.27 show intensity and range behavior at a medium value of OD. Figures B.1 through B.8 in the appendix present intensity and range behavior at high and then low values of intensity. The Figures 2.24 through 2.27 show intensity and range for one test point (one OD value) in the linear region of operation. The significant number of bad pixels is addressed when the bad pixel map is introduced.

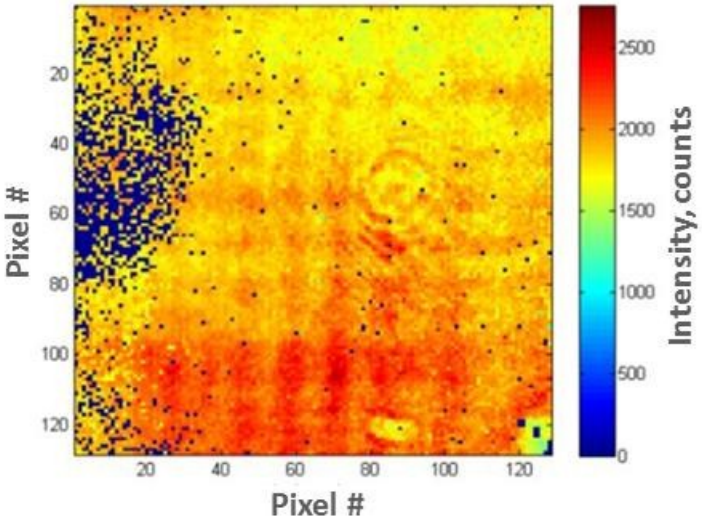

Figure 2.24: Intensity plot (at a medium intensity with most pixels in the linear region) of flat STR target board taken by the var-FOV lidar at OD = 3.621 during range / intensity calibrations.

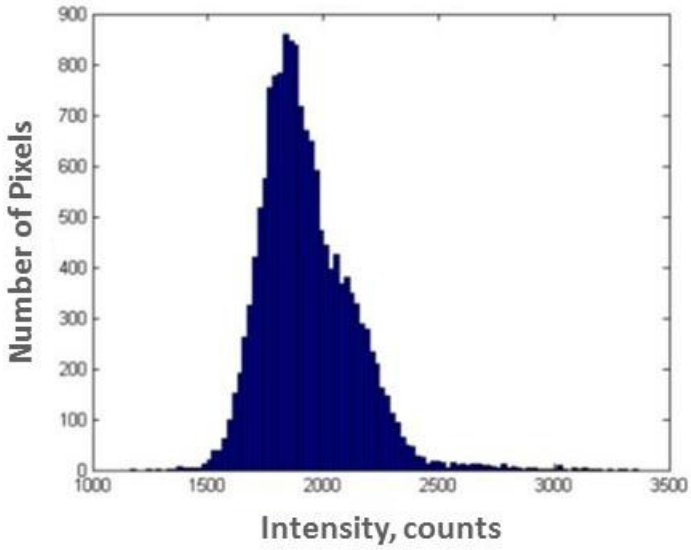

Figure 2.25: Histogram of intensity (at medium intensity with most pixels in the linear region) frame from var-FOV lidar at OD = 3.621.

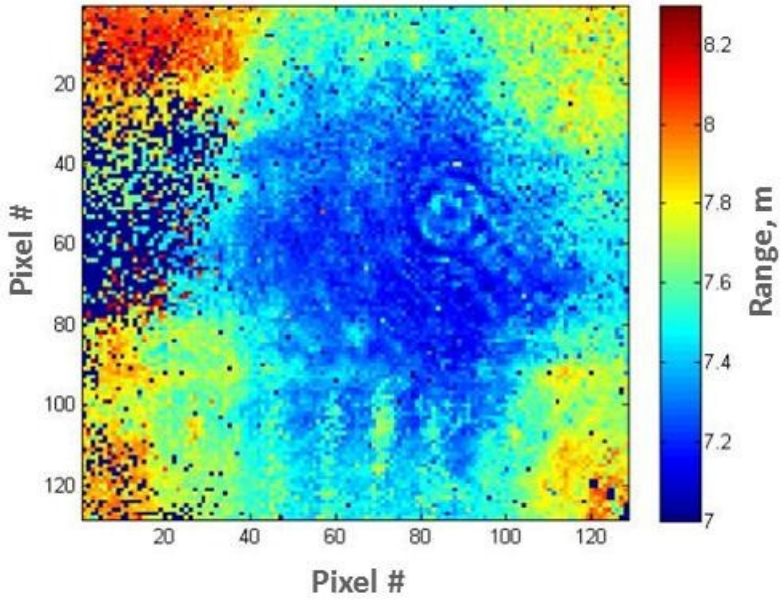

Figure 2.26: Range plot (at medium intensity case with most pixels in the linear region) of flat STR target board taken by var-FOV lidar at an OD = 3.621 during range / intensity calibrations.

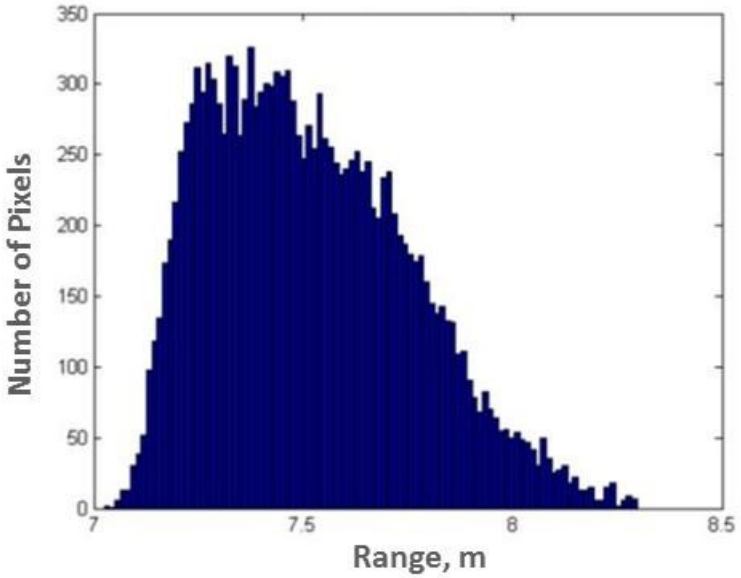

Figure 2.27: Histogram of range (at medium intensity case with most pixels in the linear region) from var-FOV lidar at OD = 3.621.

The above figures are used in order to illustrate the need for calibration. Figures 2.24 and 2.26 illustrate the precision problem being addressed. Figure 2.24 shows that the flat, uniform (diffuse with uniform reflectivity) target board is being illuminated in a non-perfect way by the transmitter optics (non-perfect top-hat beam spatial profile) such that the center portion of the target backscatters with higher intensity than the peripheral portions. Figure 2.26 illustrates the range solutions for all pixels which indicates that the board is not flat, even though it is known to be flat to better than the precision limit of the sensor, with the center portion showing a smaller range value than the periphery, i.e. the flat target board appears to be bent in 3-D in a way to look like a bump with higher intensities appearing closer. The range histogram of Figure 2.27 confirms that the pixels do indicate a span of different range values. All other OD test points used in the calibration follow the same trend observed for the one OD test point of Figures 2.24 through 2.27. Figures 2.24 and 2.26 provide an additional illustration on the negative effects of

intensity-dependent range. The intensity image of Figure 2.24 exhibits a cross-hatch pattern which is a result of the spatial intensity modes of the Fibertek laser which are also present in the intensity plots provided by the manufacturer. The range image of Figure 2.26 exhibit the same cross-hatch pattern, i.e. the intensity signature is passed on to the range image so that the target appears to have crests and troughs even though it is known to be flat to better than the maximum precision of the system. The 1000 to 2500 count range of linear operations represents the dynamic range of the sensor (from signal drop out where the pixels are not triggered to the point of signal saturation and loss of precision).

Not all 16,384 pixels respond properly in general and not all yield a successful calibration. Some pixels have detectors which are damaged and thus which generate no correction coefficients, while other pixels respond, but not correctly and thus yield calibrations which do not pass quality tests. Some pixels are bad by design since they are utilized for other purposes. Figure 2.28 is a map of the pixels which do not have usable range / intensity calibrations from ASC based on LaRC data for the var-FOV lidar which is used in the operational flight experiments to exclude bad pixel data. Figure 2.28 indicates 1766 bad pixels which is 10.8% of the total number of available pixels. The significant number of bad pixels is tolerable for the var-FOV lidar since it is devoted to evaluation of the zoom objective and to evaluation of an image-enhancement technique known as super resolution, both of which are tolerant of bad pixels. The fixed-FOV lidar, which is being used to evaluate the mosaic hazard detection technique, is not tolerant of bad pixels since each frame is a critical pieces of the stitched-together terrain map. The super-resolution technique is a three-dimensional version of the familiar digital zoom employed in many consumer digital cameras in which additional sub-pixel information is gleaned by combining successive images which are slightly offset from one

another by minute camera motions which move the actual pixels around the scene of interest and result in an effective increase in the number of pixels.

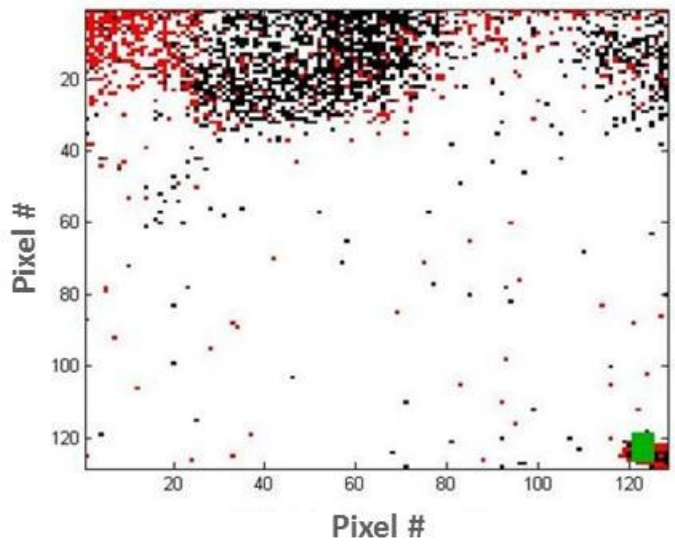

Figure 2.28: Map of the pixels without usable range / intensity calibrations from ASC based on LaRC data for the var-FOV lidar (black = pixels with no calibration due to non-response = 1111, red = pixels with a calibration = 615, and green = pixels devoted to other uses and thus not usable for ranging = 40 for a grand total of 1766 pixels not usable for ranging).

Since the range / intensity calibration is in place, the range precision can be estimated. The procedure for acquiring data to evaluate range precision is identical to that already discussed in the fixed-FOV lidar techniques section. As a reminder, the LaRC calibration coefficients are applied in post-processing, while the ASC coefficients are applied in real-time in the camera firmware and are the ones to be used in the present flight test (although efforts are underway to incorporate the higher-performing LaRC coefficients into firmware). Figure 2.29 compares the range precision before and after the LaRC calibration coefficients are applied as a function of case number. The case number is correlated to particular OD values used in the test by Table 2.7. Figure 2.29 shows that in the planned, linear operation region, the eight centimeter range

precision goal is met by the LaRC coefficients for cases numbered five and higher which correspond to lower intensity test points. Figure 2.29 indicates that the eight centimeter goal is not met for cases three and four which correspond to higher intensity test points in the linear range as those points show precision climbing to 15 cm. Since the range precision meets the eight centimeter goal for lower intensities, an operational fix is possible which would force the lidar to operate in the favorable region of the curve. Since the lidar has excess maximum range capability available, the AGC algorithm could be set such that the lidar does not enter the higher intensity region of the curve (lower case number). Figure 2.29 also demonstrates that the range / intensity calibration makes a considerable difference in range precision with un-calibrated precision in the 20 to 30 cm realm and calibrated precision remaining in the vicinity of the eight centimeter goal.

Table 2.7: Test case number correlation with OD.

Case #	OD
1	2.521
2	2.852
3	3.082
4	3.29
5	3.621
6	3.851
7	4.126

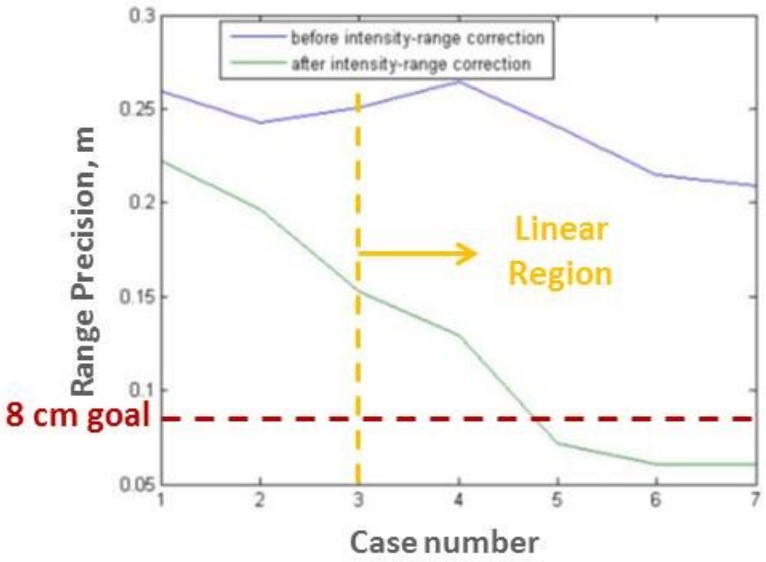

Figure 2.29: Range precision comparison before and after applying LaRC range / intensity calibrations for var-FOV lidar over a span of OD's on the flat STR target board showing that the 8 cm range precision goal is marginally met in the planned, linear operating region of case 3 and higher. In the lower OD portion (higher intensity of cases 3 and 4) of the linear region precision varies up to 15 cm, but in the higher OD portion (lower intensity of cases 5 through 7) it remains below the 8 cm goal.

Figures 2.26, 2.27, 2.30 and 2.31 illustrate the effect which the range / intensity calibration has on range precision in a single frame of data (i.e. peering into the case five point on the Figure 2.29 curve in more detail). Figure 2.26 is a range contour plot for the case five OD value for the flat STR target board before application of the range / intensity calibration. Note that the board, even though it is actually flat, appears curved due to the range / intensity effect. Figure 2.27 confirms the apparent curvature of the board as it is a range histogram which shows a spread of range values for various pixels that far exceeds the 8 cm precision goal. Figure 2.30 is a range contour plot at the same conditions as Figure 2.26 except that the LaRC range / intensity calibration has been applied. The apparent curvature of the board is gone. Figure 2.31, also after the range / intensity calibration application, confirms the flatness of the board. Comparing

Figure 2.27 (histogram before calibration is applied) with Figure 2.31 (histogram after calibration is applied), the concentration of the histogram about a smaller set of range bins is clear which means that the range precision is clearly improved by application of the LaRC range / intensity calibration. The comparison of Figures 2.27 and 2.31 confirms the disparity in range precision numbers between un-calibrated and calibrated cases shown in Figure 28 case five. Additional evidence of the efficacy of the range / intensity calibration and its likely positive effect on range precision is the absence of the cross-hatch pattern in the range contour of Figure 2.30 (after calibration) which was so apparent in Figure 2.26 (before calibration), being carried over from the intensity image of Figure 2.24 which clearly made the cross-hatch pattern an intensity-dependent range phenomenon detrimental to range precision.

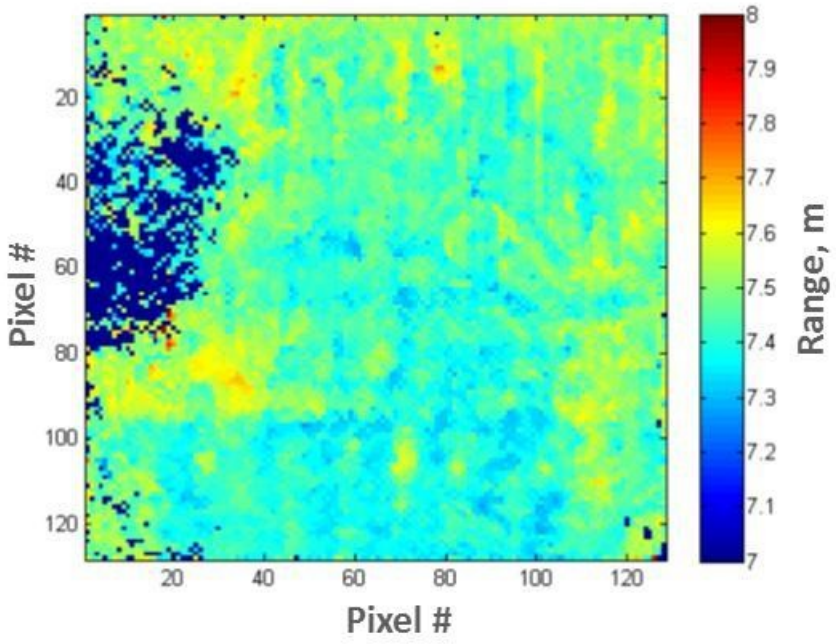

Figure 2.30: Range plot AFTER application of LaRC range / intensity calibration; image taken of flat STR target board by var-FOV lidar at an OD = 3.621, case 5. Board apparent curvature has been removed successfully.

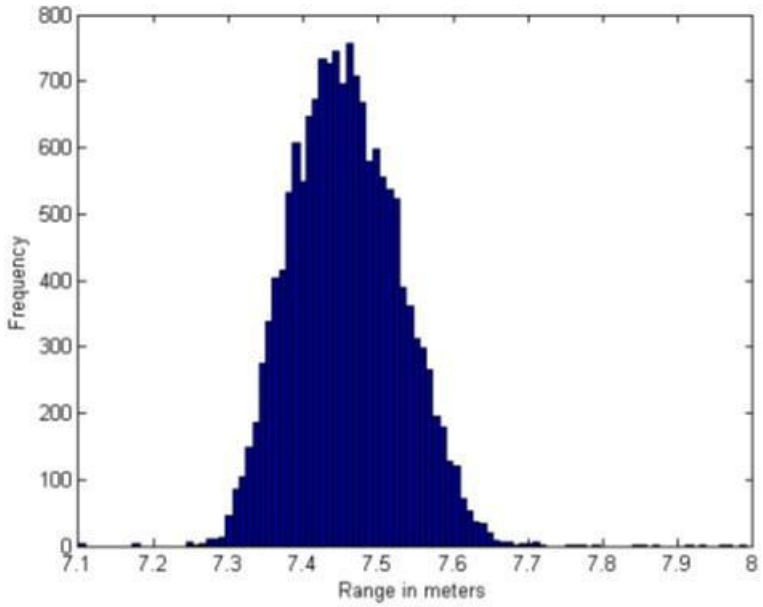

Figure 2.31: Histogram of range AFTER application of LaRC range / intensity calibration; image taken of flat STR target board by var-FOV lidar at an OD = 3.621, case 5. Note the spread of ranges has been concentrated to meet the 8 cm precision goal successfully.

The ASC range / intensity calibration also significantly improves range precision, but not quite as well as the LaRC curves. Figure 2.32 shows that in the planned, linear operation region, the eight centimeter range precision goal is closely approached but not met when the ASC calibration is applied. The linear region starts at an OD of approximately 3.1 and extends to the maximum OD value shown in the plot. The range precision of 11 to 13 cm is still considerably better than the un-calibrated precision extends to nearly 30 cm. As discussed in relation to the var-FOV lidars large number of bad pixels, the zoom optics and super-resolution algorithm objectives being addressed by the var-FOV lidar are robust against range precisions which approach but do not achieve the eight centimeter ALHAT goal, since that goal is more critical to the fixed-FOV lidar employing the mosaic hazard detection technique.

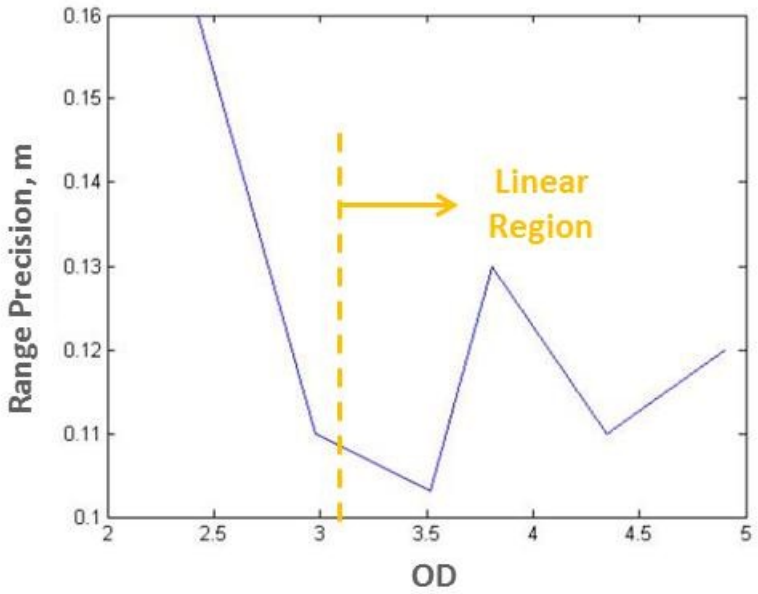

Figure 2.32: Range precision trend after applying ASC range / intensity calibration coefficients for var-FOV lidar over a span of OD's on the flat STR target board showing that the 8 cm range precision goal is approached in the planned, linear operating region (still several times better than an un-calibrated lidar). This calibration is applied in real-time to flight data.

Despite its lower quality performance as compared to the new calibration being explored by LaRC, the ASC calibration is used for the flight tests since the camera firmware is currently written to accept it and has not been modified yet to accept the LaRC calibration as the LaRC calibration has only recently been under development. Having the calibration reside in the Tiger Eye camera's firmware is critical to the flight tests since the calibrations are applied in real-time so that the sensor output is corrected in real-time and ready for use by the ALHAT hazard detection algorithms in flight.

2.7 Lab Characterization Summary and Flight Test 4 System Goals

Table 2.8 presents a summary of the flash lidar lab characterization test results as they compare to the derived goals for the flash lidar system to be demonstrated in the present field test series. The goals in green are met, while the goals in bold orange font are the ones only

marginally met. Since the Fibertek is the planned space laser, the maximum range achieved with it is the defining case for maximum range. The FOV range for the var-FOV lidar does not achieve the full 24° goal since the mono-static transmitter optics delivered by the vendor were non-functional (had attempted to pass a pulsed lidar through focus to achieve the wide angles which resulted in air breakdown). LaRC attempted, with the author playing a key role, a last minute effort to recover by designing, developing, characterizing, and integrating a set of bi-static transmitter optics into the lidar sensor head which could be automatically zoomed through software control to achieve the desired divergence range and succeeded up to the point of 16°. The fixed-FOV lidar achieves the eight centimeter range precision goal using the LaRC method in post-processing. However for the real-time ASC method (which is the one to be used in flight), the fixed-FOV lidar precision only achieves the 8 cm goal within a range of intensities and then falls short of the goal as intensities drop with the most extreme intensity falling considerable away from the goal, however still achieving better range precision than an un-calibrated lidar. Since the lidar has excess maximum range capability, the intensities during the flight test should remain in the high portion of the linear range so that 8 cm is achieved. For future developments, the LaRC method will be incorporated into firmware for application in real-time. The LaRC method does better than the eight centimeter goal for the lower intensities of the linear range (higher OD values), so the AGC could be tuned to force operations in the lower-intensity regime for performance superior to that of the eight centimeter goal. The var-FOV lidar range precision results are summarized in Table 2.8 and are similar in character to the range precision results for the fixed-FOV lidar just described and should be sufficient for flight.

Table 2.8: Lab characterization test results compared to the flash lidar system goals for field test #4. Goals which are met are in green and goals which are marginally met are in bold **orange**.

Parameter	Fixed-FOV Flash Lidar (lab characterization)	Var-FOV Flash Lidar (lab characterization)	Field Test 4 Goals
Max operational range	1070 m	1600 m	1000 m
# pixels	128 x 128	128 x 128	128 x 128
FOV	1°	6° to 16°	**1°, 6° - 24°**
Range Precision: a) Post-processed b) Real-time	6 to 8 cm 8 to 20 cm	6 to 15 cm 11 to 13 cm	- **8 cm**
Frame Rate	30 Hz	30 Hz	30 Hz
Range / Intensity Calibration Application	Real-time	Real-time	Real-time

HELICOPTER INTEGRATION AND FLIGHT TEST

The purpose of flight testing in a development effort is to test the systems at longer ranges, detect hazards in a dynamic environment with a complete GNC and sensing system, detect hazards under non-controlled conditions such as real-world reflectivity gradients, subject the systems to the rigors of the flight environment to push environmental design robustness, test the system response to the solar background under dynamic conditions, etc.

3.1 Integration of Lidars to Helicopter

The lidars along with supporting electronics are integrated along with the rest of the ALHAT GNC system into an instrumentation pod (see Figure 3.1) on the mesa test range at NASA JPL.

Figure 3.1: Both flash lidars along with support electronics are integrated into an instrumentation pod (center) with the other ALHAT GNC systems from NASA-JPL, NASA-JSC, and Draper Labs at the NASA-JPL mesa test range.

The flash lidar sensor heads, along with the Doppler Lidar and Laser Altimeter, are installed in a vertically translating rack structure (Figures 3.2 and 3.3) within the pod so that they can be retracted within the pod and the pod belly door closed during hazardous portions of the flight (takeoff and landing) and any time that laser safety must be ensured. During experiment data collection phases, the lidars are lowered down from the pod and pointed to the desired target area with the two-axis gimbal system. Figure 3.2 shows the rack structure from the 3D CAD model used in pod and rack design, while Figure 3.3 shows a front and rear view of the two LaRC flash lidar sensor heads (without aerodynamic shrouds) along with the 19-inch rack-mount supporting electronics chassis.

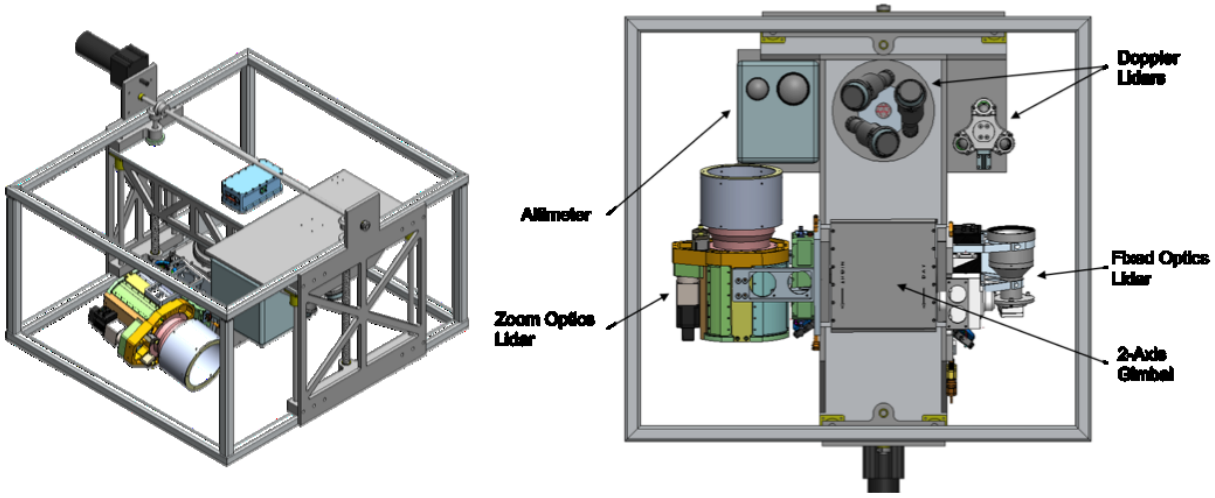

Figure 3.2: Vertically translating rack structure within the instrumentation pod into which the ALHAT lidars (including the two flash lidars) are mouted. The rack structure retracts or deploys the lidars depending upon the phase of flight, in conjunction with a protective belly pod door, to keep the lidars safe during takeoff and landing operations and to provide additional laser safety during transit flights.

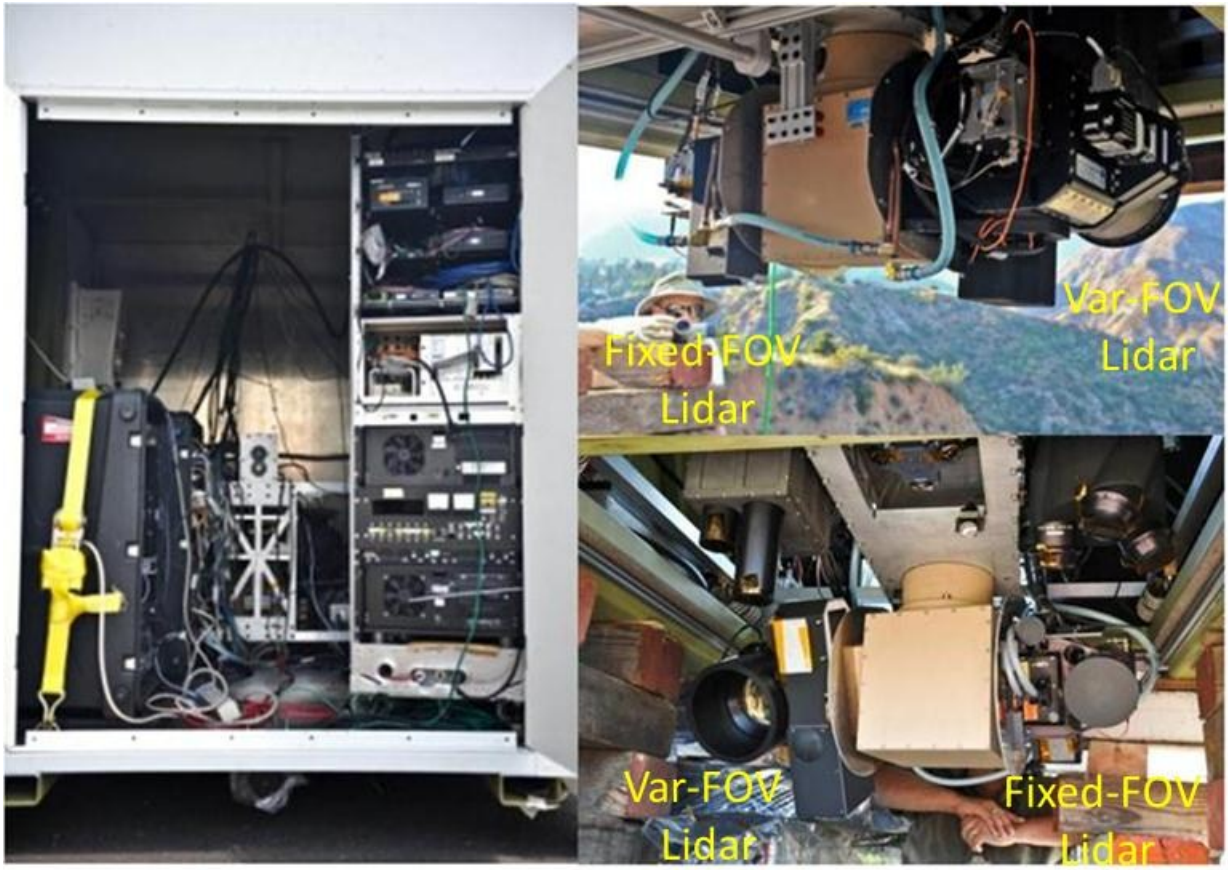

Figure 3.3: Instrumentation pod interior (left) showing 19-inch rack mount electronics and instrumentation pod belly with both LaRC flash lidar sensor heads deployed with belly pod door open (front and rear view).

Once all equipment is integrated and electrical, mechanical and software interfaces are debugged, the systems are put through a series of integrated function tests with ever-increasing complexity to approach the best simulation possible of the flight environment before moving all systems to the helicopter. Figure 3.4 shows successful results from the fixed-FOV maximum range integrated functional test. Note that the var-FOV lidar was not maximum-range tested since pod orientation precluded a clear view of the targets. The left half of Figure 3.4 shows the set of slanted targets in the foreground and the set of normal targets in the background. The right

half of Figure 3.5 shows the range contour plot which indicates that the targets are at approximately 975m. Figure 3.5 even shows sloping of the slanted targets since the range contour plot shows a gradient of coloring along them.

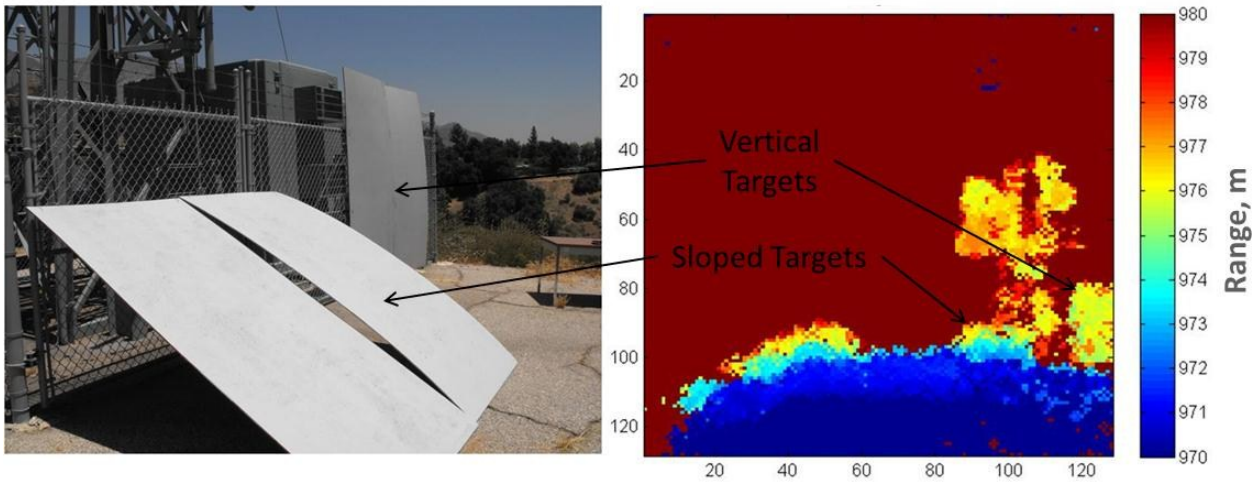

Figure 3.4: Fixed-FOV lidar maximum range functional test as integrated in the instrumentation pod with the normal and slanted targets located approximately 1 km away on the JPL mesa test range. The range contour plot shows successful ranging of both targets at approximately 975m.

After instrumentation pod integration and test are completed at NASA-JPL, the pod is moved to the high desert to be integrated to the Erickson Aircrane helicopter at NASA-Dryden. The integration of the pod to the helicopter is relatively simple by design. The pod attaches to the helicopter via a set of hooks just as other equipment attaches to the helicopter during its normal fire-fighting operations. A set of cabling is run from the pod to the aft cockpit of the helicopter where an ALHAT systems operator flies for attachment to user interface equipment (displays, keyboard, mouse, power control box, etc). The aft cockpit of the Aircrane is normally occupied by the crane operator. The ALHAT systems are self-contained in the pod by design so that all checkout operations are performed separately from the helicopter so that all debugging

can occur prior to the start of the expensive use of helicopter and crew ground and flight time. Figure 3.5 shows the instrumentation pod as installed on the helicopter along with the aft cockpit of the helicopter where the ALHAT systems operator is seated during the flights. Figure 3.6 shows the instrumentation pod (with aft door open) undergoing preflight checks along with pictures of the two flash lidars deployed by the translating rack structure with belly doors open. Figure 3.6 shows the lidars' aero shrouds installed including the laser exit hole on the fixed-FOV lidar which was later found to be misaligned and resulting in laser scatter and thus loss of laser energy on target and unwanted pixel pre-triggering which necessitated the lowering of lidar sensitivity.

Figure 3.5: Instrumentation pod installed on Erickson Aircrane helicopter at NASA-Dryden and ready for the start of flight testing along with aft cockpit where ALHAT systems operator rides during the flights.

Figure 3.6: Instrumentation pod during preflight operations with rack systems being tested and with both flights lidars undergoing test. The flash lidars are deployed with the belly pod door open and each lidar covered by its own aerodynamic shroud. The fixed-FOV aerodynamic shroud, annotated on the picture, was the shroud whose laser exit opening was later found to be mis-aligned with the beam resulting in beam scattering and loss of laser exit energy along with the associated laser-scattering-induced pixel pre-triggering that required a reduction in lidar sensitivity.

3.2 Helicopter Flight Testing

3.2.1 Test Plan

Field test #4 flight test operations consisted of multiple approaches to a hazard field of human-made geometric targets along with some runs targeted at the flat lakebed surface. The Erickson Aircrane helicopter is chosen for its large payload ability (in service, it literally acts as a powerful crane which sits on a helicopter rather than on a ground cart like typical cranes) and resulting excess power which enables it to approach the trajectories utilized in the ALHAT planetary landing simulations. Figure 3.7 shows the planned helicopter approach angles (15, 30, and 45 deg) and flight paths to the hazard field. The approach paths are chosen both for the convenience of the navigation system and to ensure that certain hazard groups are included in the FOV of the given approach.

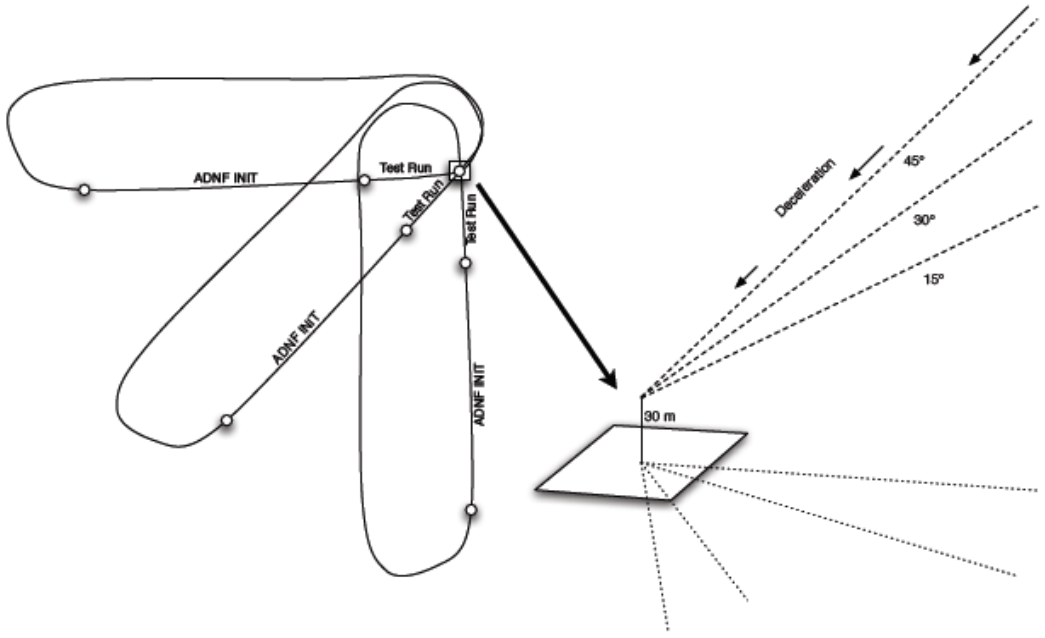

Figure 3.7: Field test approach angles and flight paths to the hazard field.

Figure 3.8 shows the test area within Edwards AFB. Flights originate from NASA-Dryden in the upper portion of the figure and proceed to the hazard field situated several miles away on the southwest corner of the Edwards AFB Rogers Dry Lake. Figure 3.9 shows the full hazard field which consists of a host of square and hemispherical targets of varying size and spacing as well as safe-sites with no hazards designed to stress the lidar precision as well as the hazard detection algorithms. The hazard field is surrounded by the flat lakebed which served as a target for the range precision runs.

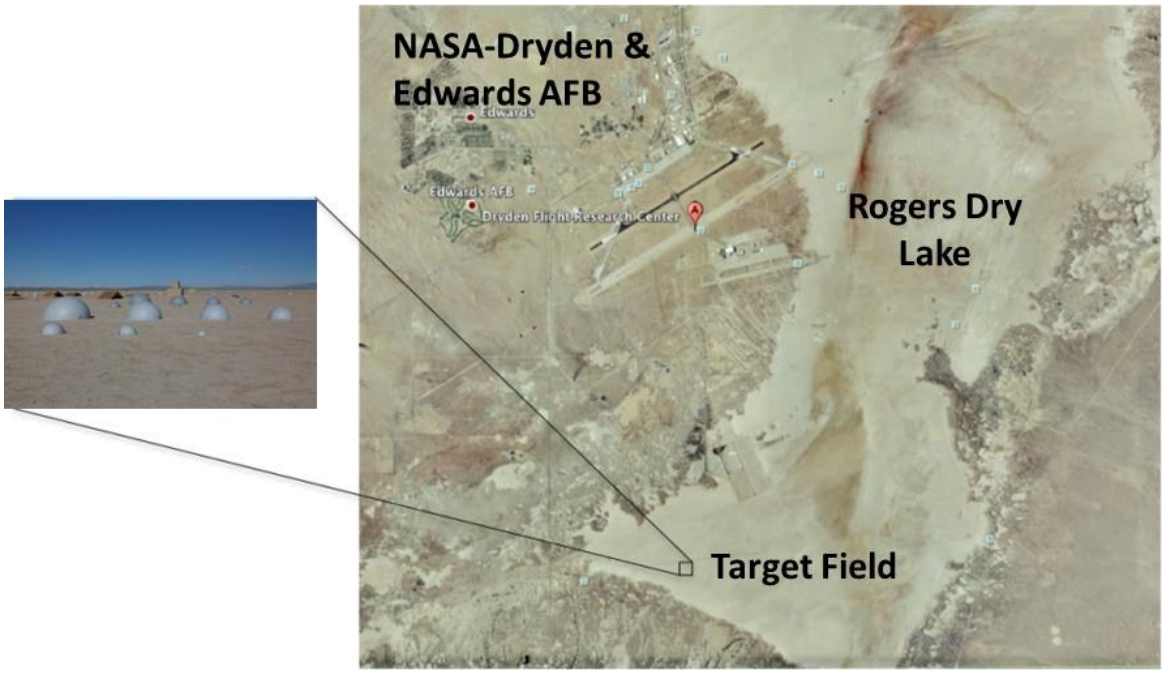

Figure 3.8: Edwards AFB Rogers Dry Lake with hazard field situated on the southwest corner. A portion of the hazard field is shown.

Figure 3.9: Aerial view of the complete hazard field situated on the Edwards AFB Rogers Dry Lake which consists of a host of square and hemispherical targets of varying size and spacing as well as safe-sites with no hazards designed to stress the lidar precision as well as the hazard detection algorithms. The hazard field is surrounded by the flat lakebed which serves as a target for the range precision runs.

3.2.2 Flight Results

The field test consists of eight flights spread over a week. The first three flights are referred to as shakeout flights and are focused mainly on initial checkout of systems in flight. Shakeout flight data is usable for characterization if it turns out that the systems, or the involved subsystems, perform nominally. Table 3.1 details the flights, which of the two lidars is operated on a given flight (since there is only one set of support electronics and since flight test needs are different between the two lidars anyway), and any pertinent notes. Recall that only one lidar is operated per flight since the two lidars share the same set of support electronics and data acquisition and control system. Due to systems glitches, no lidar data is available from the first

shakeout flight flown on July 25, 2010. In shakeout flight two, the systems performed nominally and the data is usable for characterization. Fiber optic t0 damage on the var-FOV lidar minimized the useful data available from the third shakeout flight. Flight numbers one through three, which employed the fixed-FOV lidar, generated nominal data usable for characterization. During flights one through three, the var-FOV lidar undergoes t0 fiber optic troubleshooting and repair. Flight number four is dedicated to camera and gimbal objectives and the lidars are not operated. Flight number five generated nominal data with the var-FOV lidar repaired and functional. The flights are concluded just minutes after the start of a significant brush fire to the west which did extensive damage to the surrounding areas. Had the flights not concluded prior to the fires, experiment operations would have been difficult if not impossible since ash began raining down from the fires. Figure 3.10 shows the helicopter lifting off from NASA-Dryen and carrying the ALHAT instrumentation pod to the Edwards AFB test range. Figure 3.10 also shows the required laser safety goggles which the ground station team at the hazard field (and all team members) are required to wear due to the class IV non-eye-safe lasers being used.

Table 3.1: Flight log from ALHAT field test #4, where shakeout flights are considered systems checkout flights.

Flight Number	Flash Lidar Utilized	Notes
Shakeout Flight 1	Fixed-FOV	No data collected, 7/25/2010
Shakeout Flight 2	Fixed-FOV	7/26/2010
Shakeout Flight 3	Var-FOV	Fiber optic t0 damage, 7/26/2010
Flight 1	Fixed-FOV	7/27/2010
Flight 2	Fixed-FOV	7/27/2010
Flight 3	Fixed-FOV	7/28/2010
Flight 4	None	Lidars not operated, 7/28/2010
Flight 5	Var-FOV	7/29/2010

Figure 3.10: Erikson Aircrane helicopter lifting off from NASA-Dryden and en-route to Edwards AFB test range carrying the ALHAT instrumentation pod. Members of the ground station at the hazard field are required to wear laser safety goggles due to the class IV non-eye-safe lasers being used.

The flight results show a combination of successes and challenges. A number of cutting-edge components from industry and NASA are integrated, many for the first time, into two high performance flash lidar sensors which take the next step closer to the final ALHAT system for space missions. Flight history is built up on the new technologies. LaRC custom data acquisition and control flight software bugs resulted in intermittent performance and data storage. The JPL two-axis gimbal experienced similar intermittent performance due to bugs. The gimbal is critical to hazard detection since it ensures that the lidars are pointed at the hazard field. The combination of intermittent lidar performance coupled with intermittent gimbal performance resulted in little successful hazard detection. Hazards are imaged, but just by the luck of where the lidar happened to be pointed at the time given the helicopter attitude. Since it is not possible to point at hazards at the desired ranges, the algorithms and sensor are not tested at their stress conditions for hazard detection. Sufficient data is gleaned in order to characterize the lidars, but sufficient data is not available to make conclusions on hazard detection and avoidance. Also as a result of the combined intermittent bugs, the var-FOV zoom functioning is not tested, but rather the variable FOV is set at one fixed FOV number. The following discussion covers characterization of the lidar maximum range and range precision for the fixed-FOV lidar and the var-FOV lidar. Before data is presented, a few key image processing and data interpretation concepts are discussed.

3.2.2.1 Flash Lidar Data Results

3.2.2.1.1 Image Processing and Data Interpretation

The lidar image processing consists of several real-time and post-processing steps. The real-time steps, so called since the image is frozen at the laser pulse as is characteristic of flash lidar systems and any processing done is accomplished (with the image output) before the next laser pulse based on the period between 30 Hz pulses i.e. 1/30 of a second. Image construction consists of real-time peak detection. Range / intensity calibrations are applied after peak detection is accomplished. The post-processing steps occur after the flight is concluded and data is downloaded. The post-processing steps include removal of bad pixels using the bad pixel map as a guide. Each Lidar range image is converted to a digital elevation map (DEM). As an example of one of the many steps in the process of conversion of lidar range image to DEM is the removal of vehicle attitude perspective which introduces a sloping effect to the terrain if it is not corrected for.

The flight number five images from the var-FOV lidar require some adjustment which arose as a result of the rushed nature of the on-the-fly t0 fiber optic repair process. The transmitter and receiver FOV for the var-FOV lidar are misaligned. Since misalignment, by its nature, results in non-illuminated pixels, and since the non-illuminated pixels eventually time-out and report a maximum number of 2130 m for the range parameter, a cropping process is instituted during the data processing phase to ignore the non-illuminated pixels so that they do not corrupt the maximum range and range precision numbers. In addition to the transmitter and receiver misalignment, a data acquisition system anomaly resulted in a strip of image data (approximately 25% of the right side of the image) being lost. The correction for the strip of lost data is identical to the correction for the misalignment.

Interpretation of maximum range and range precision data builds upon the interpretation methods used in the lab characterization section. Maximum operational range is defined as the

range where 90% of the pixels trigger. The LaRC custom data acquisition system represents range with a 16 bit word using a two centimeter step size which sets 1300 meters as the largest range number that can be represented. The LaRC custom data acquisition system represents intensity with an 8 bit word with a step size of 16 intensity counts giving the full 0 to 4096 intensity counts span which is available from the camera. In the case of range precision estimation, a plane is fit to the data and range standard deviation calculations are referenced to the best fit plane. The best-fit plane is an attempt to effectively create a zero incidence as was carefully set for the target board mechanically during lab characterization (as discussed in the lab characterization section) to separate apparent range biasing from the actual range precision number. Since the flight environment is not an idealized one like the lab environment and a number of uncertainties are present, the best fit plane does not totally remove the false range biasing, thus range precision flight numbers are not as reliable as lab numbers and are generally falsely higher.

In the case of hazard detection, hazards of opportunity are imaged due to the issues discussed at the beginning of the flight results section (gimbal experienced intermittent operations which, when combined with the lidar intermittent operations, due to custom data acquisition and control software issues, the desired hazards are not imaged at the desired ranges). Since it is not possible to point to hazards at the desired ranges, the algorithms and sensor are not tested at their stress conditions for hazard detection.

3.2.2.1.2 Results Summary

Table 3.2 summaries the results from lab characterization and flight testing and compares performance to the field test #4 goals. The number of pixels and frame rate goals are met. The

FOV goals results and discussions are briefly presented in the present section first. The details behind the maximum range, range precision, and range/intensity application numbers shown in Table 3.2 are discussed in the fixed-FOV lidar and var-FOV lidar results and discussion sections forthcoming. All goals are either met (colored green in the table) or marginally met (colored orange in the table).

The FOV goals set for the present field test (number four) are marginally achieved. The shortfall between the goals and the actual performance arose from the failure of the zoom optics manufacturer to develop a working set of transmitter optics. A rushed in-house effort was undertaken to develop the transmitter zoom optics which partially met the desired zoom range and were successfully demonstrated in lab characterization testing. The additional shortfall between the lab performance and the flight performance was unrelated to the laser or optics hardware, but was instead a failure on the part of the data acquisition and control team to complete software development and test to be able to drive either set of zoom optics in flight (receiver or transmitter) which resulted in a single FOV being flown with no zooming attempted.

Table 3.2: Summary of lab and flight characterization results for the fixed-FOV and var-FOV lidars as compared with the field test #4 goals. Goals which are achieved are in bold **green** color, while goals only marginally achieved are in bold **orange** color.

Parameter	Fixed-FOV Flash Lidar		Var-FOV Flash Lidar		Field Test 4 Goals
	Lab	Flight	Lab	Flight	
Max operational range	1070 m	*600 m	1600 m	1200 m	1000 m
# pixels	128 x 128	128 x 128	128 x 128	128 x 128	128 x 128
FOV	1°	1°	6° to 16°	**6°	**1°, 6° - 24°**
Range Precision: a) Post-processed	6 to 8 cm	-	6 to 15 cm	-	-
b) Real-time	8 to 20 cm	***7 to 14 cm	11 to 13 cm	***12 to 20 cm	**8 cm**
Frame Rate	30 Hz	30 Hz	30 Hz	30 Hz	30 Hz
Range / Intensity Calibration Application	Real-time	Real-time	Real-time	Real-time	Real-time

* Aerodynamic shroud mechanical misalignment artifically limited maximum range, fixed-FOV lidar

** Data acquisiton and control system failures, not related to zoom techology

*** Flight characterization not as reliable as lab for this parameter

3.2.2.1.3 Fixed-FOV Lidar Results and Discussion

3.2.2.1.3.1 Maximum Range

The flight results define a maximum range for the fixed-FOV lidar. Figure 3.11 shows the percentage of triggered pixels for each complete frame of lidar data as a function of the frame number. The frames are acquired at 30 Hz or 30 frames per second, indicating that the descent maneuver lasts approximately five minutes. Since the maximum range is defined as the range at which 90% of the pixels trigger, the maximum range occurs approximately at frame number 4300. Thus for frame numbers less than 4300, less than 90% of the pixels trigger which means that the range image is only a partial image.

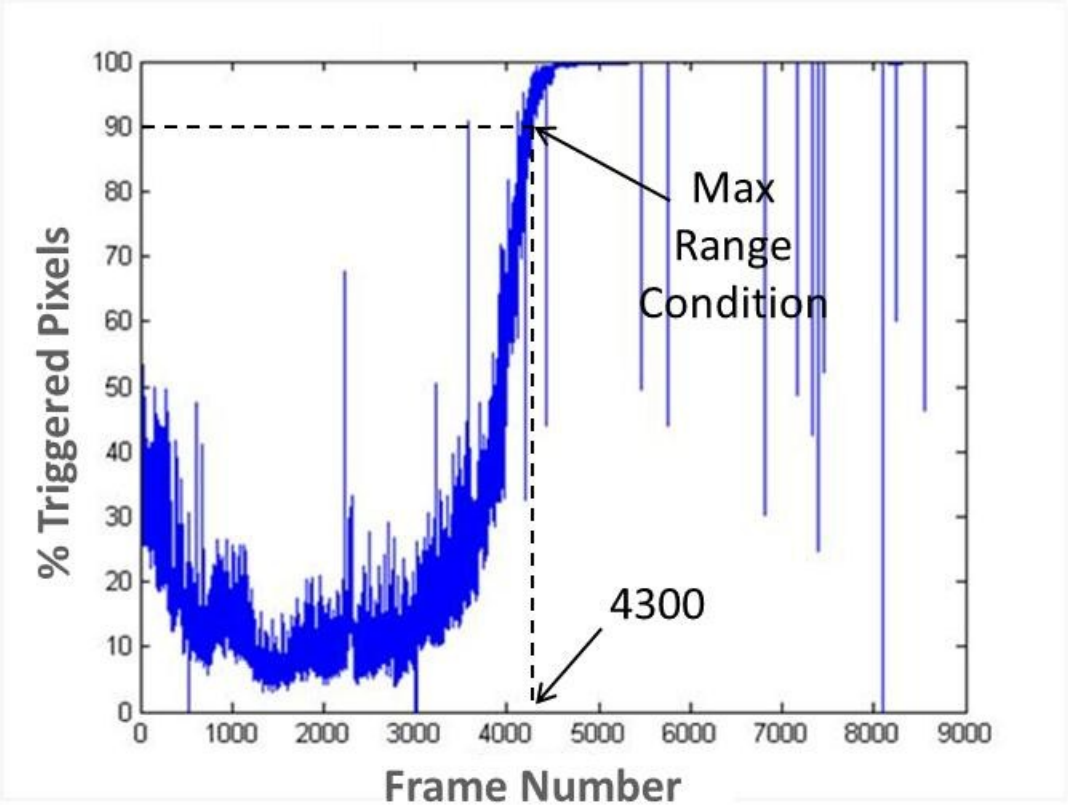

Figure 3.11: Shakeout flight #2 (fixed-FOV lidar) descent maneuver percentage of triggered pixels as a function of frame number at a rate of 30 frames / sec. Maximum range (90% pixels triggered) is shown occur in the vicinity of frame number 4300.

Figure 3.12 shows the average intensity of each frame of lidar data as a function of frame number. The average intensity, which corresponds to the maximum range condition as defined in Figure 3.11, is approximately 780 counts. Figure 3.13 shows the average range of each lidar frame as a function of frame number. The average range, which corresponds to the maximum range condition as defined in Figure 3.11, is approximately 600 m.

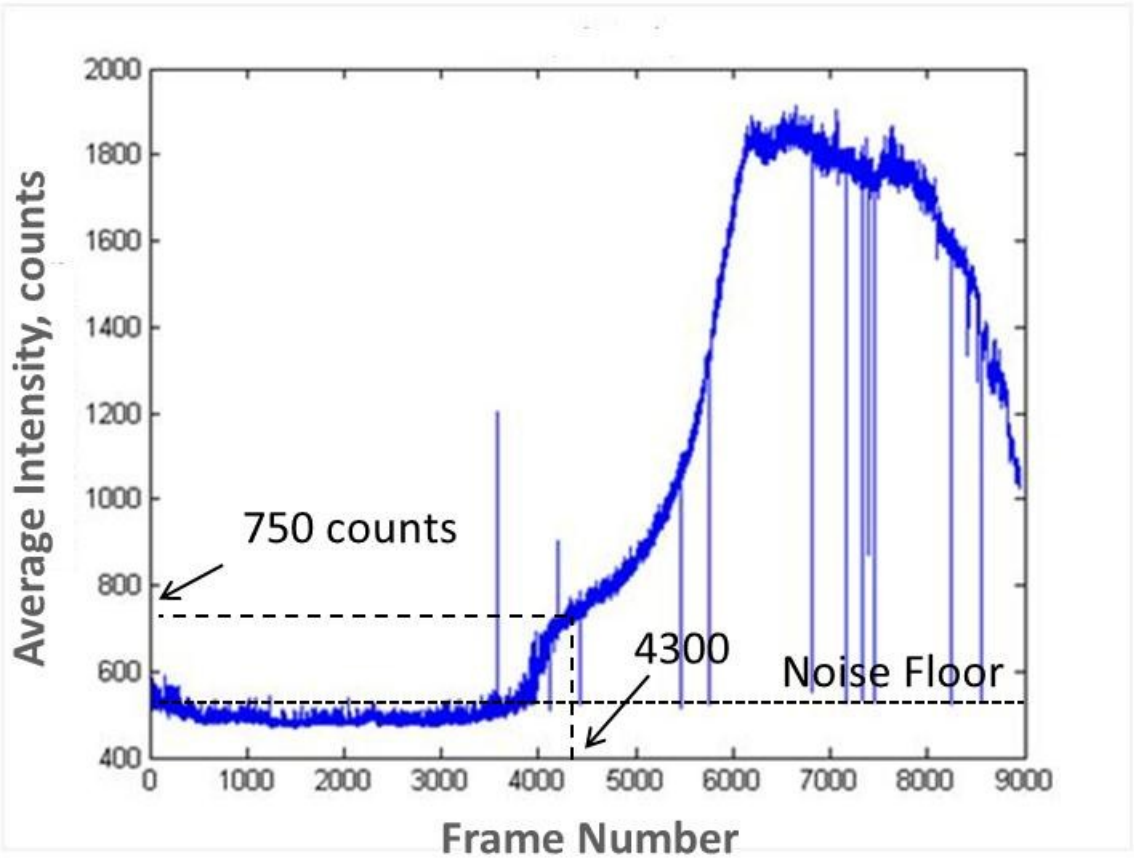

Figure 3.12: Shakeout flight #2 (fixed-FOV lidar) descent maneuver average intensity of all triggered pixels as a function of frame number (30 frames / sec) acquired in flight. Maximum range resides at approximately frame number 4300 with an average intensity of 750 counts.

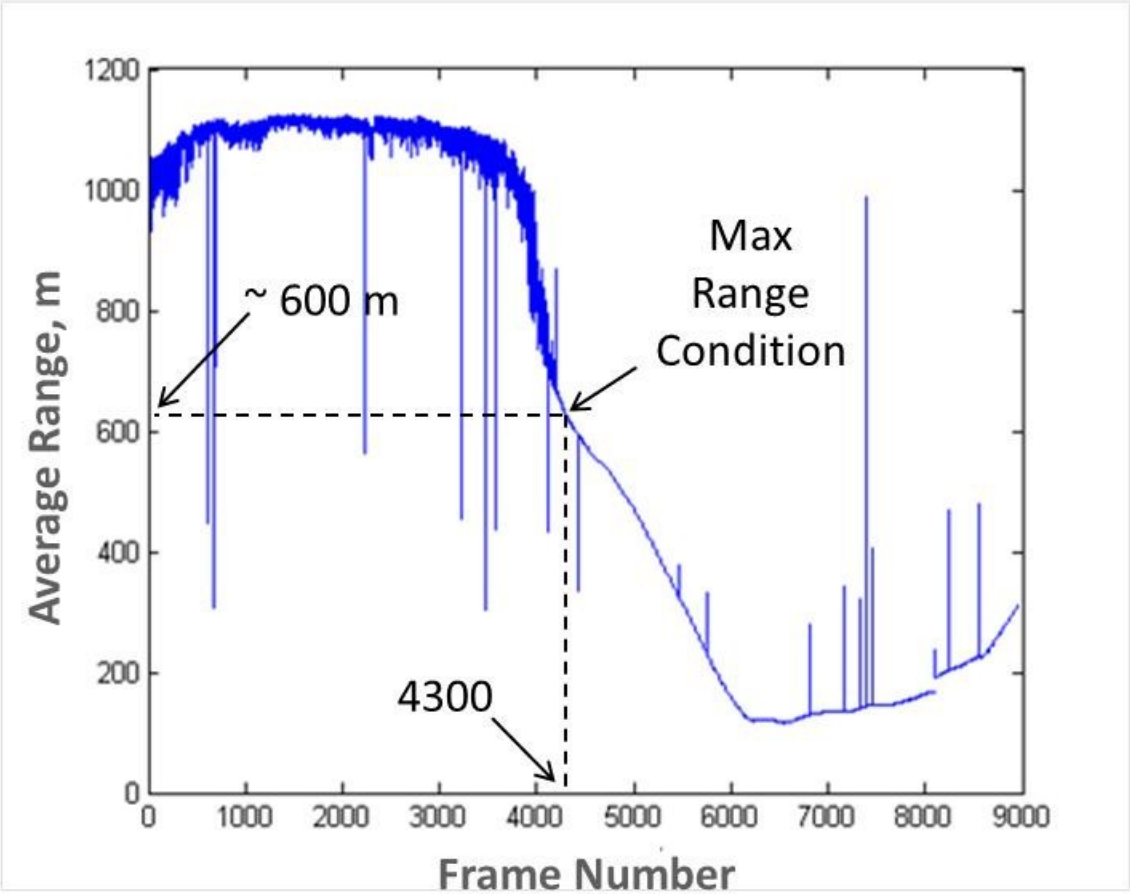

Figure 3.13: Shakeout flight #2 (fixed-FOV lidar) descent maneuver average range of all triggered pixels as a function of frame number (30 frames / sec). Maximum range resides at approximately 600 m.

Figures 3.14 and 3.15 present an intensity contour plot along with its associated range contour plot for a range value above the maximum range condition as defined in Figure 3.11 in order to provide a window into the behavior of the lidar above maximum range. The intensity contour in Figure 3.14 shows that only the lower left corner of pixels trigger which is indicated by an intensity value at slightly above the noise floor of 1000 counts. The corresponding range contour plot in Figure 3.15 confirms that only a cluster of pixels in the lower left trigger and they report a range value around 800 m while the remainder of the un-triggered pixels report a

maximum range of 2130 m which the LaRC custom data acquisition system operating at 16 bits in range just reports this 2130 m as the maximum value possible to represent with 2 cm steps which is 1300 m which is outside the bounds of the displayed range contour anyway.

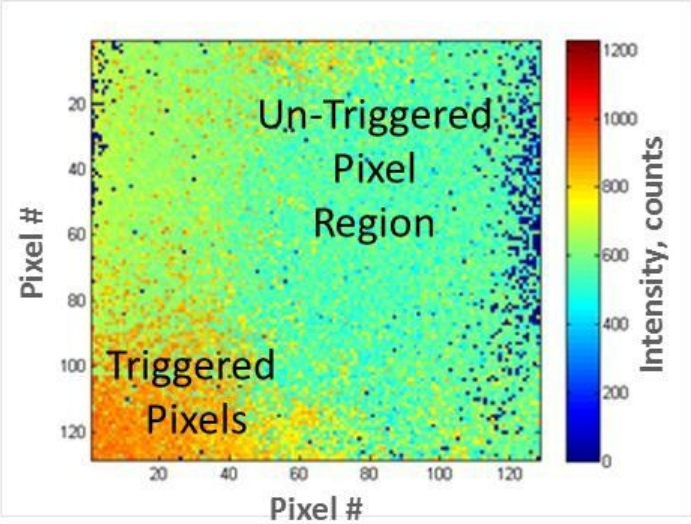

Figure 3.14: Shakeout flight #2 (fixed-FOV lidar) intensity contour frame at a range above the maximum range of 600 m. Image depicts some triggered (lower left) and some un-triggered pixels. Most intensities are outside the linear range.

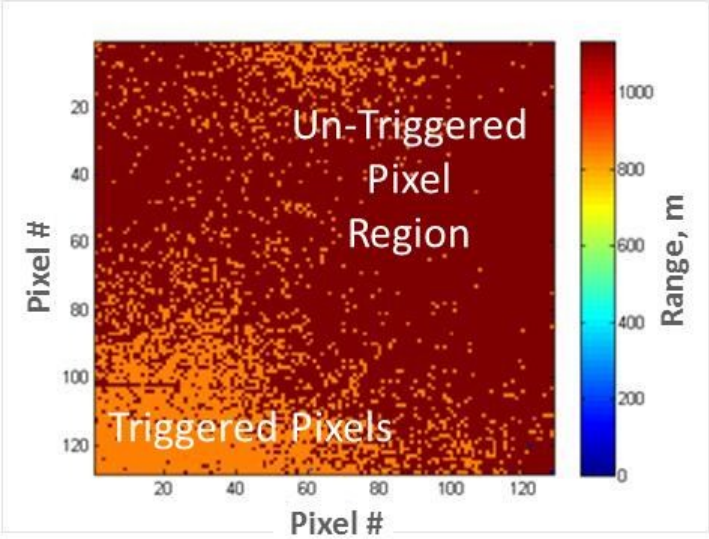

Figure 3.15: Shakeout flight #2 (fixed-FOV lidar) range contour frame at a range above the maximum range of 600 m. Image depicts some triggered (lower left) and some un-triggered pixels.

Figures 3.16 and 3.17 present an intensity contour plot along with its associated range contour plot for a range value below the maximum range condition as defined in Figure 3.11 in order to provide a window into the behavior of the lidar below maximum range. The intensity contour in Figure 3.16 shows that all pixels trigger which is indicated by an intensity value at or above the noise floor of 1000 counts. Most pixels indicate an intensity value somewhere between 1100 and 1600 counts. The corresponding range contour plot in Figure 3.17 confirms that all pixels trigger and they report a range value around 322 m. A range gradient appears in the range contour plot. The gradient is just the apparent ground slope introduced by gimbal / vehicle attitude being non-normal to the lakebed being imaged.

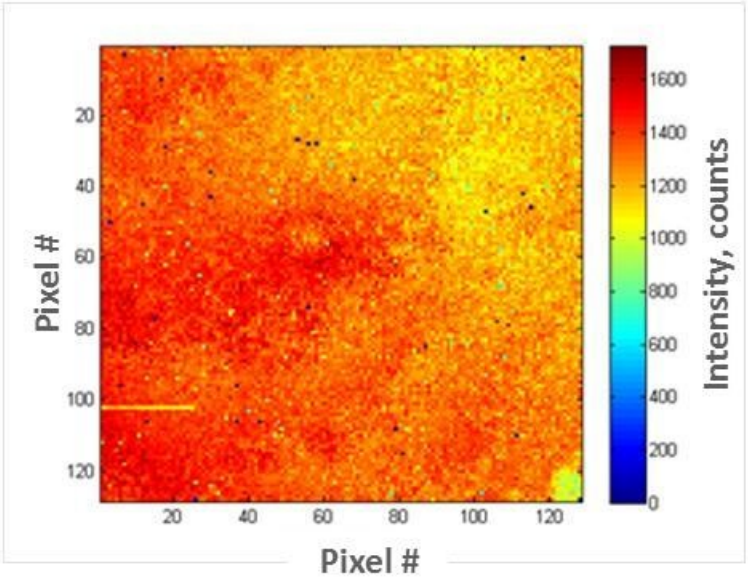

Figure 3.16: Shakeout flight #2 (fixed-FOV lidar) intensity contour frame at a range of approximately 322 m which is below the maximum. Noise floor is at 1000 counts. The image depicts triggering of all pixels. All intensities are within the linear range.

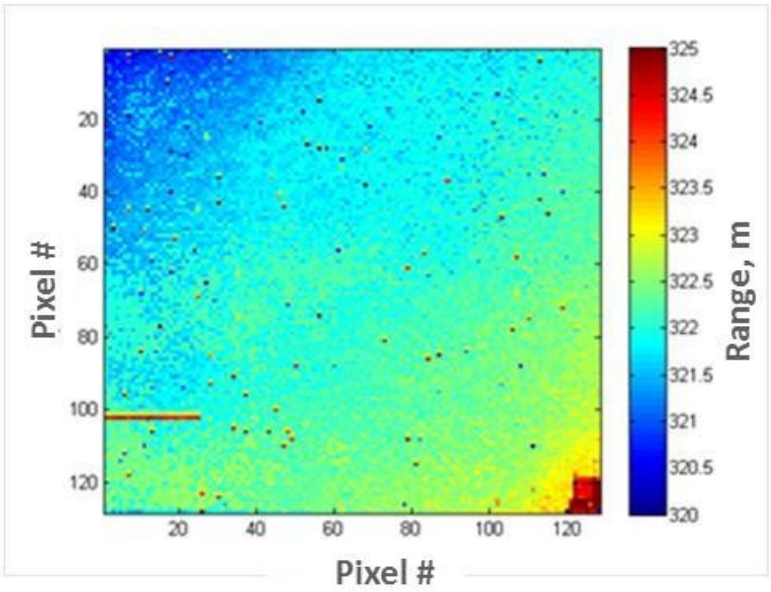

Figure 3.17: Shakeout flight #2 (fixed-FOV lidar) range contour frame at a range of approximately 322 m which is below the maximum. The image depicts triggering of all pixels. The range gradient in the frame is due to vehicle / gimbal attitude, i.e. the lakebed has an apparent slope due to a non-zero-degree incidence angle between the ground and the lidar.

Since the lab characterization testing predicts the maximum operating range to be 1070 m, the 600 m range measured in flight represents a significant shortfall. The shortfall is due to unexpected laser scatter from a last minute replacement of the aerodynamic shroud that is used to protect the lidar sensor head during flight. The previous shroud had too much damage to be flight-worthy due to the shipping process and all of the removals and reinstallations which occurred during the integration testing. The hole for the laser to fire through in the new shroud was not aligned properly with the laser which resulted in some laser energy being lost to scatter which reduced maximum range. Maximum range was further reduced since the scatter caused some pixel pre-triggering which necessitated a manual reduction in the lidar's sensitivity. Due to the fast pace of the flight testing, the laser scatter was not discovered until too late. When considering the results summary in Table 3.2 above, the 600 m maximum range of the fixed-FOV lidar is not considered in determining whether or not the field test goal is achieved since the 600 m limitation is due to a known anomaly.

3.2.2.1.3.2 Range Precision

The flight results define a range precision for the fixed-FOV lidar. The field test goal relating to application of range / intensity calibration in real-time is met since the coefficients are uploaded to camera firmware and are applied to data before transmittal out of the camera in real-time. Figure 3.18 is a plot of range precision as a function of range for images taken of the flat dry lakebed. The plot indicates that range precision varies between 7 and 14 cm depending upon range. The character of the plot closely follows that observed in the lab characterization (Figure 2.23) if the 100 m range from Figure 3.18 is equated to the OD value of 1.6 from Figure 2.23 and likewise, if the 600 m range is equated to the OD of 2.65. Thus, excellent agreement exists

between lab and flight results. The real-time calibrations used are those generated by the camera manufacturer using LaRC-acquired data. Figure 3.18 shows that the real-time calibration only marginally meets the eight centimeter goal. Recall from Figure 2.18 in the lab characterization section that the LaRC calibration, which is being evaluated as a new calibration method, shows superior results, meeting the eight centimeter goal. Since the LaRC method is new, it is not compatible yet with the camera firmware (i.e. can only be applied in post-processing), but developing that compatibility is underway. Table 3.2 contains a note on flight range precision results which indicates that lab characterization values are more reliable for determining range precision. The additional reliability of lab characterization is due to the ability to control parameters to isolate the range precision from other error sources. An example is that in lab characterization, the results are obtained from a target at zero incidence, while in flight the incidence angle is not zero but instead dynamically changing and must be compensated for in the analysis through a best fit plane which contains uncertainty which gets intertwined with the range precision estimate, thus the flight range precision estimate is generally worse (higher) than the more correct lab estimate.

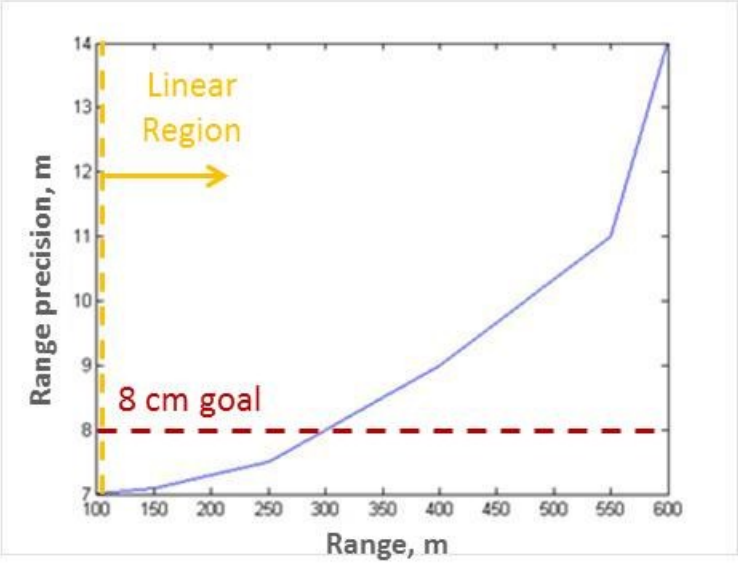

Figure 3.18: Shakeout flight #2 (fixed-FOV lidar) range precision as a function of range, based on images of the flat lakebed. Range precision is shown to vary between 7 and 14 cm in the linear region.

3.2.2.1.3.3 Target Detection

Several targets of opportunity are detected. Due to the combination of lidar data acquisition glitches and gimbal anomalies, the integrated system did not operate simultaneously for long enough to accomplish purposeful hazard detection at the ranges which would have stressed the sensor and algorithms. The targets imaged in the present section are those which the lidar happened to image. The hazard images do show an end-to-end lidar ability to image hazards for 3-D visualization. Figure 3.19 shows the 3-D lidar image of a 24 inch hemispherical target at 150m from the second shakeout flight. In addition to the 3-D DEM, Figure 3.19 shows the associated intensity and range images of the hazard. The intensity image indicates that the hazard is in the linear range and the range image shows that the hazard is on an apparent slope. The apparent slope is in fact just an illusion created by the relative attitude of the vehicle/gimbal with respect to the ground. The apparent slope is removed in the DEM generation process.

Figure 3.20 shows a 38 cm hemispherical hazard imaged on the second shakeout flight from a range of 325 m. Figure 3.20 shows the intensity and range images of the hazard. The intensity image shows the hazard and surrounding ground to be in the linear range and the range image shows an apparent slope just like the Figure 3.19 image which is due to vehicle attitude with respect to the flat, un-sloping ground. The DEM of Figure 3.20 removes the apparent slope. Note that the 38 cm hemisphere is just a smaller hemisphere in a line of hemispheres decreasing in size which is made clearer by the picture in Figure 3.21 showing the subject set of hazards positioned on the Rogers Dry Lake. Figures 3.22 and 3.23 are intensity and range contour plots, respectively, showing a stack of boxes from flight number three at a range of approximately 180m. The box intensities are all in the linear range.

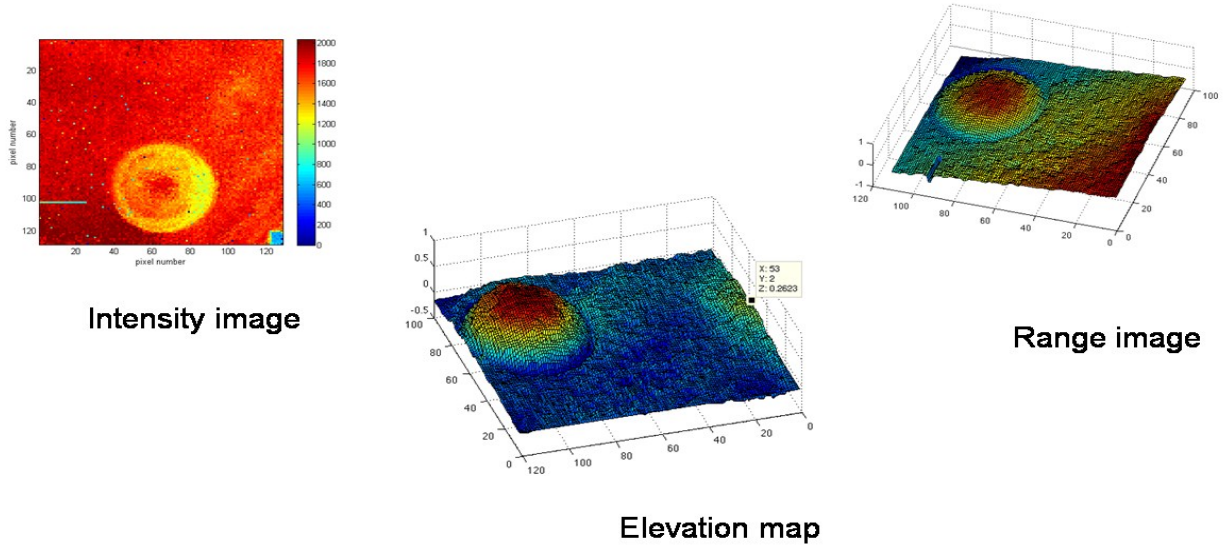

Figure 3.19: Shakeout flight #2 (fixed-FOV lidar) 24 inch hemisphere target detection at a range of approximately 150m, median filtering applied. An apparent slope is present in the 3-D range image since the lidar and the ground are not at normal angles (i.e. angle of incidence is non-zero). The elevation map has no apparent slope as a result of the back project portion of image conversion from range to DEM. All intensities are within the linear range.

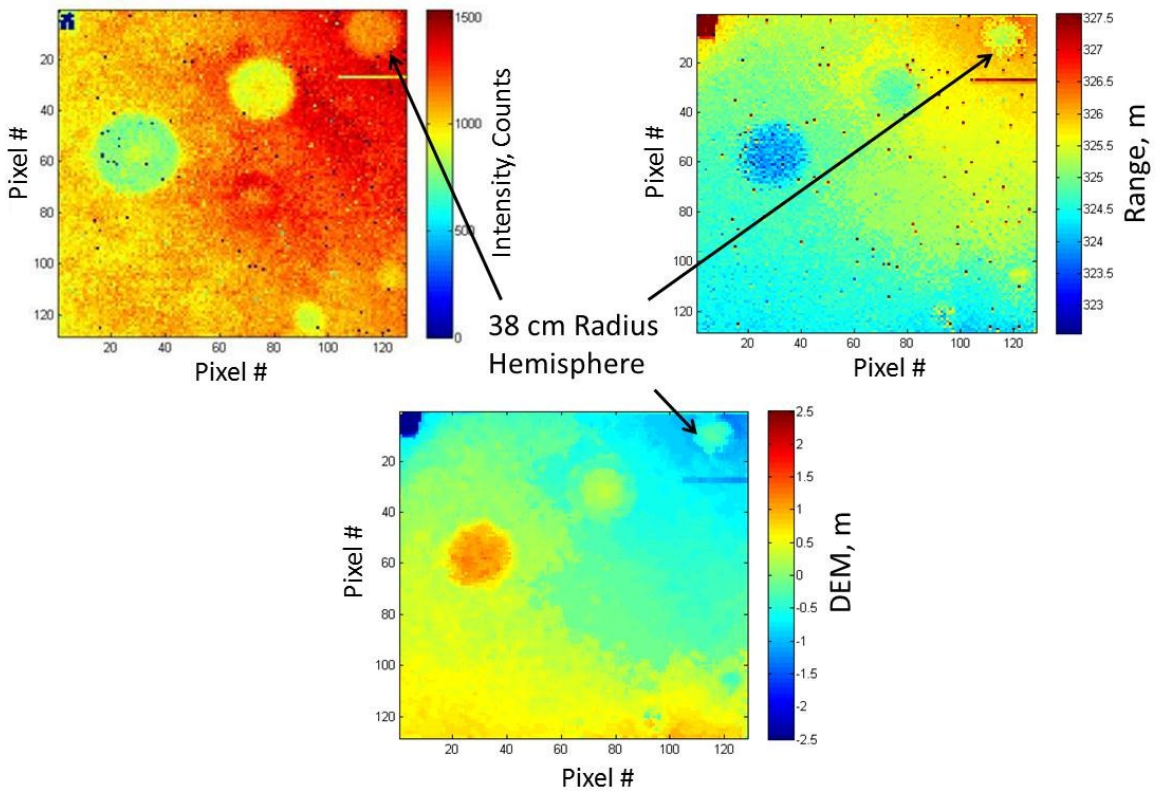

Figure 3.20: Shakeout flight #2 (fixed-FOV lidar) 38 cm hemisphere target detection at a range of 325m. The intensity image, the range image, and the DEM are shown. All intensities are within the linear range.

Figure 3.21: Hemispherical targets on Rogers Dry Lakebed, Edwards AFB, CA as detected in previous figure.

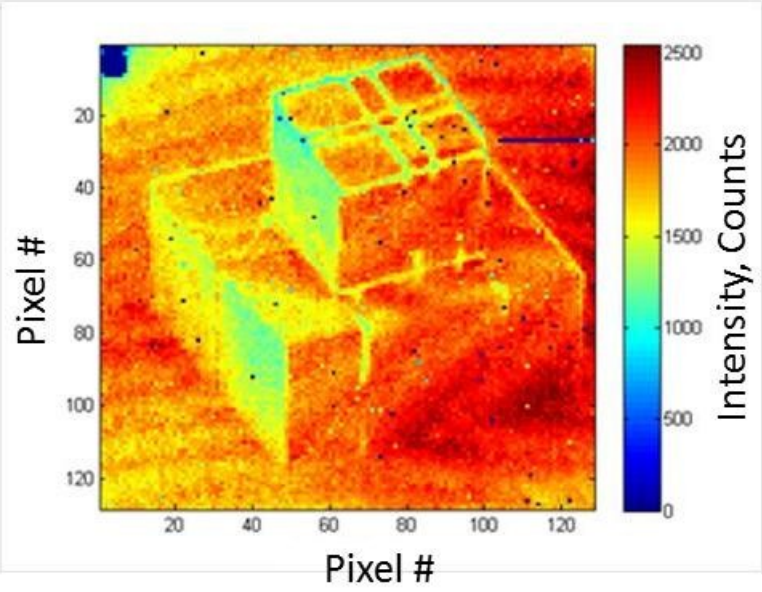

Figure 3.22: Flight #3 (fixed-FOV lidar) target detection (stacked boxes) intensity image from a range of 180m. The intensities of the boxes are within the linear range.

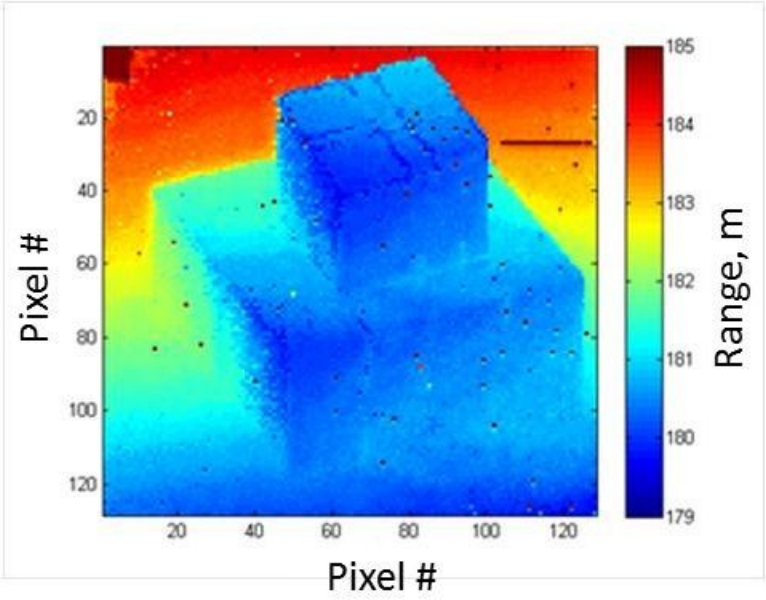

Figure 3.23: Flight #3 (fixed-FOV lidar) target detection (stacked boxes) range image.

3.2.2.1.4 Var-FOV Lidar Results and Discussion

3.2.2.1.4.1 Maximum Range

Due to the rushed nature of the repair to the var-FOV lidar's t0 fiber optic, the images of flight five, the final flight of the field test campaign, contain two anomalies which are compensated for in the maximum range estimation process. The data interpretation section above describes the anomalies in detail along with the causes of the anomalies. Additionally, data is collected at only one FOV due to a failure to complete development of the autonomous software control of the zoom motors as discussed in the results summary section above. Figures 3.24 and 3.25 present an intensity contour plot along with its associated range contour plot at the six degree FOV setting for a range value of approximately 1,090 m which is slightly below the maximum range condition in order to provide a window into the behavior of the var-FOV lidar below maximum range. The intensity contour in Figure 3.24 shows the strip of lost data on the right (lost due to a data acquisition system anomaly) and the un-triggered pixels around the perimeter. The un-triggered pixels fall at and below the noise floor of 1000 counts. The un-triggered pixels are caused by mis-alignment between the transmitter and receiver for the reasons and with the implications discussed in the data interpretation section earlier. The intensity contour in Figure 3.24 shows that all triggered pixels fall in the linear region. The corresponding range contour plot in Figure 3.25 confirms the strip of lost data and the un-triggered pixels. In the case of the range plot, un-triggered pixels manifest themselves as a range value which exceeds the contour maximum since un-triggered pixels report a range value of 2130 m. A range gradient appears in the interior portion of the range contour plot with good pixels. The gradient is just the apparent ground slope introduced by gimbal / vehicle attitude being non-normal to the lakebed being imaged. For the maximum range and the range precision analysis, the strip of lost data and the un-triggered peripheral pixels are cropped out and not considered.

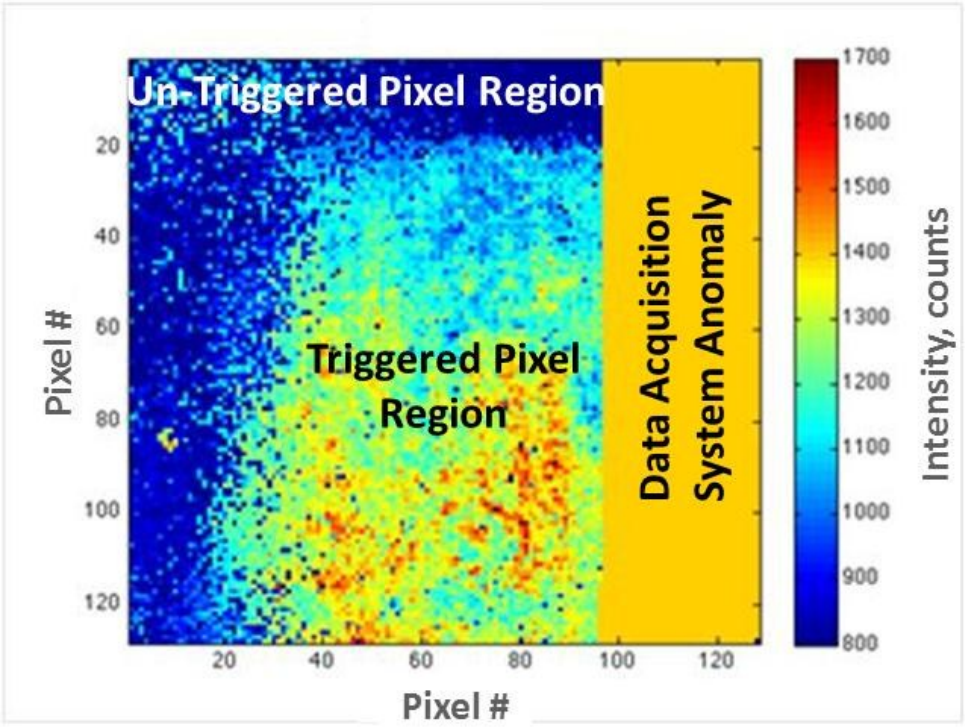

Figure 3.24: Flight #5 (var-FOV lidar) intensity contour frame for the six degree FOV setting at a range of approximately 1 km showing the strip of lost data on the right and the un-triggered pixels (near the 1000 count noise floor) around the perimeter of the image which results from transmitter / receiver FOV misalignment. The interior portion of the image shows good data in the linear range.

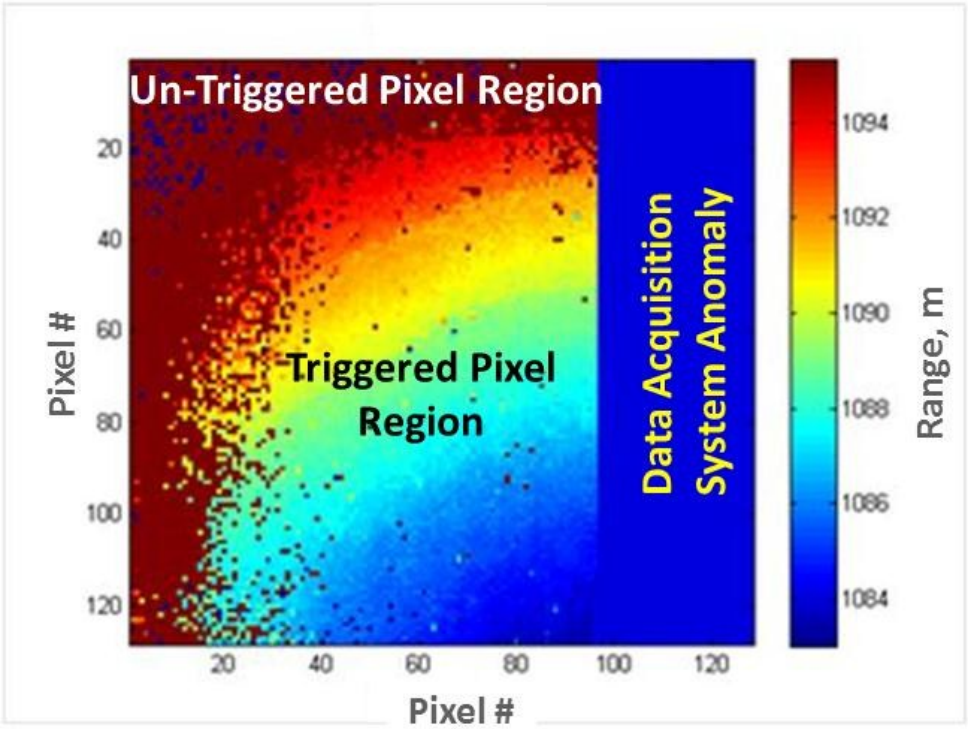

Figure 3.25: Flight #5 (var-FOV lidar) range contour frame for the six degree FOV setting showing the strip of lost data on the right and the un-triggered pixels around the perimeter of the image which results from transmitter / receiver FOV misalignment. The range value displayed for the un-triggered pixels exceeds the contour maximum (since un-triggered pixels report a range of 2130 m). The interior portion of the image shows good range data with the sloping character a normal result of non-zero-degree incidence angle between the lidar and the ground due to vehicle / gimbal attitude.

The flight number five results define a maximum range for the var-FOV lidar. Figure 3.26 shows the average intensity of each frame of lidar data (after cropping) as a function of frame number for an ascent/descent maneuver at the six degree FOV setting. Figure 3.27 shows the accompanying median range for each frame of lidar data (after cropping) as a function of frame number. Due to the cropping process, maximum range is not defined as the point where 90% of the pixels trigger. Maximum range is identified for the var-FOV lidar through comparison of Figures 3.26 and 3.27. Figure 3.27 starts by showing a range value close to 500m,

then the range spikes upward discontinuously to 1100 m and then returns discontinuously back to 500m. The discontinuous change is likely the result of a banking maneuver of the helicopter performed to set up for the run which momentarily resulted in the lidar being pointed at a distant area during the turn. The ascent maneuver begins, after a short descent to complete the setup for the run, and peaks out at 1200m at which point a descent begins to setup for the next run. The Figure 3.26 average intensity trends support the same profile of setup and then ascent to a maximum.

The var-FOV lab characterization and flight results for maximum range are in agreement based on some basic adjustments. Table 3.2 summarizes the lab and flight results as compared to the field test goals. The lab results indicate a maximum operational range of 1600m. Although the flight results are capped at 1200m, additional range could have been achieved in flight to bring the lab and flight numbers into agreement. At the maximum range condition of Figure 3.27 frame 84000, the average intensity of Figure 3.26 still reads 1200 counts. Since the noise floor rests at 1000 counts, then approximately 200 counts of additional signal reduction due to range are available and could have been used to achieve an even greater range, but the flight runs are designed to verify ALHAT goals and since the field test goal is 1000m, then longer range data is not sought during the flights. The LaRC custom data acquisition is designed with a 2 cm step size for the 16 bit range which precludes representation of ranges greater than 1300m as another illustration of limitations based on the flight test objectives for not reaching for longer ranges than the field test goals. For purposes of agreement checking, trading most of the left-over intensity for range produces a theoretical flight maximum of 1300m another 100m being accounted for by the lower surface reflectivity of the sand as compared to the reflectivity of the lab characterization target board. The sand is 40% reflective at the 11 deg incidence angle at

which the 1200m data is acquired, while the lab characterization target board reflectivity is 46%. The reflectivity adjustment should boost the flight range by 7% referring back to equation 1.7 of the flash lidar technology basics section. The remaining 200m of disagreement between lab and flight results is attributed to dynamic and less-controlled nature of flight testing versus lab testing (such as surface reflectivity deviations from the sample tested and slight deviations in laser pulse energy which are weakly temperature dependent). Thus the lab and flight data are in agreement within 200m and the field test goal of 1000m is achieved.

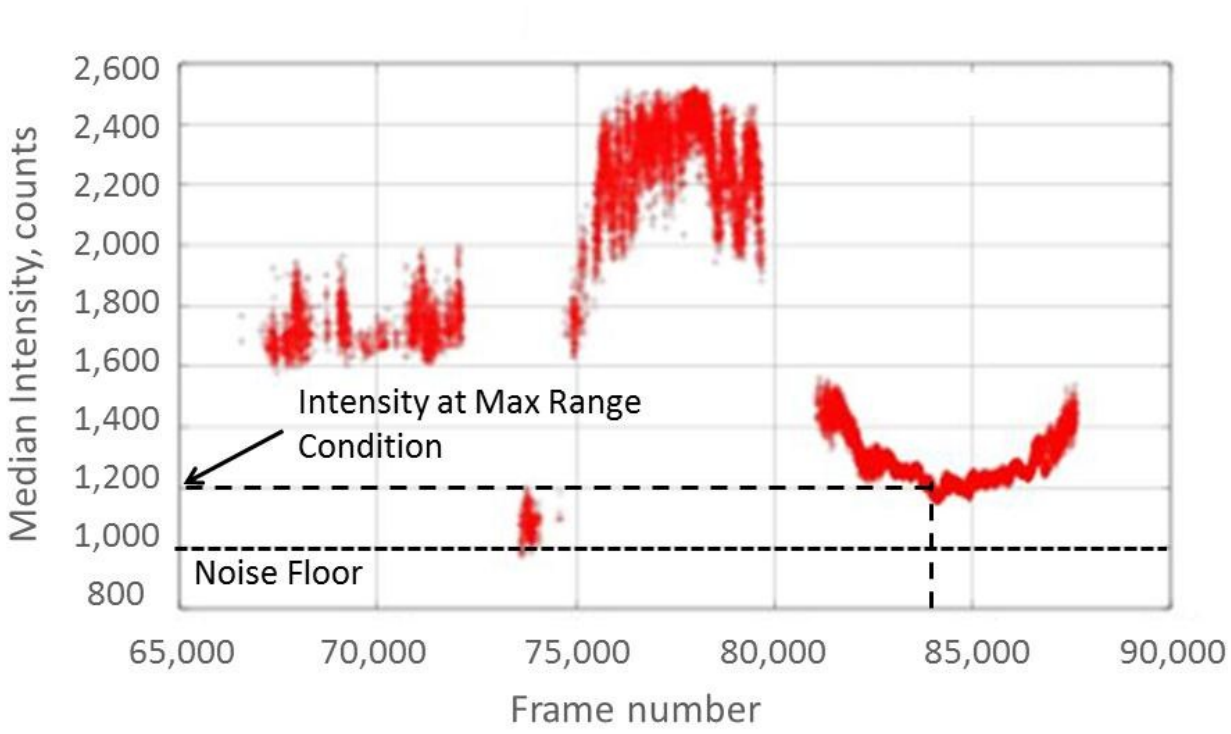

Figure 3.26: Flight #5 (var-FOV lidar) ascent/descent maneuver median intensity of all triggered pixels in the cropped region as a function of frame number (30 frames / sec) acquired in flight at the six degree FOV setting with the noise floor at approximately 1000 counts. All data resides in the linear range. Intensity at maximum range is approximately 1200 counts at frame number 83,500.

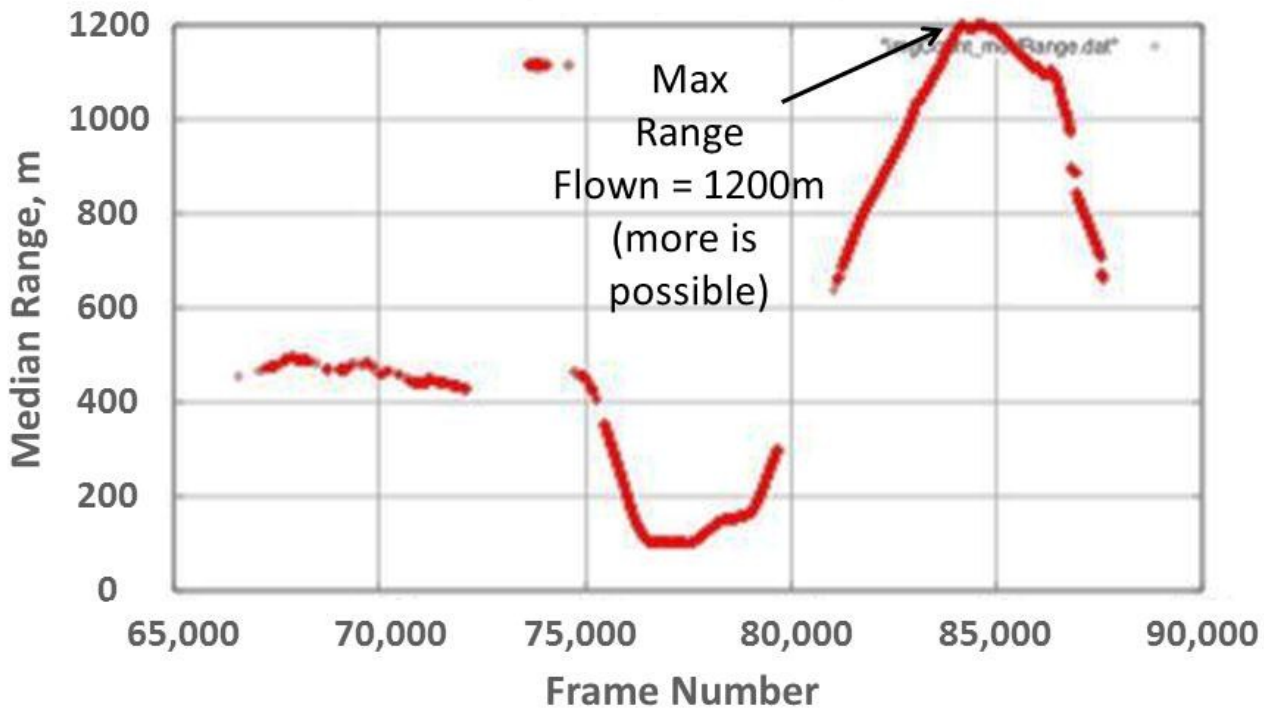

Figure 3.27: Flight #5 (var-FOV lidar) ascent/descent maneuver median range of all triggered pixels as a function of frame number (30 frames / sec) at the six degree FOV setting. Maximum range is shown to be approximately 1200 m at frame number 83,500.

3.2.2.1.4.2 Range Precision

The flight results define a range precision for the var-FOV lidar. The field test goal relating to application of range / intensity calibration in real-time is met since the coefficients are uploaded to camera firmware and are applied to data before transmittal out of the camera in real-time. Figure 3.28 is a plot of range precision as a function of range for images taken of the flat dry lakebed. The plot indicates that range precision varies between 12 and 20 cm depending upon range, with a possible outlier at 30 cm due to intensity within 100 counts of the noise threshold. Although the eight centimeter field test goal for range precision is not met for the var-FOV lidar, its other field test goals are not negatively affected since the var-FOV lidar is

intended mainly to evaluate the zoom technology and the super-resolution image enhancement both of which are robust against a slightly elevated range precision. The fixed-FOV lidar is the one whose objectives benefit more from its general achievement of the eight centimeter goal and it serves as the ALHAT test vehicle for addressing range precision.

The character of the plot in Figure 3.28 closely follows that observed in the lab characterization (Figure 2.32) if the 200 m range from Figure 3.28 is equated with the OD value of 3.0 from Figure 2.32 and, likewise, if the 1200 m range from Figure 3.28 is equated to the OD value of 4.4 from Figure 2.32. The trend of both curves resembles a trace of the letter "W." The Figure 2.32 lab curve is being compared to flight since the camera manufacturer's calibration (from LaRC-acquired data) can be loaded into firmware for real-time application in flight (i.e. since the new LaRC coefficients can only be applied in post-processing, they are not directly comparable to the flight results). The range precision curve from the flight testing is shifted upward by approximately seven to ten centimeters compared to the lab characterization curve. Since the lab is the best place to characterize range precision, it is more likely that the lab characterization numbers are closer to the actual precision. The disparity between lab and flight centers on the lack of ability to tightly control parameters in flight which can falsely add to the range precision estimate such as the inability to set and hold a fixed incidence angle between the lidar and the target, which, as was demonstrated in the lab characterization section using Figure 2.12, introduces a range bias. Additionally, the flight environment results in dynamically changing incidence angles which are partially compensated for in the analysis by applying a best-fit plane to try to remove apparent slope while computing the standard deviation, but the best fit plane contains error terms which add to range bias. The range bias changes from instant to instant which explains why the flight curve is not offset a clear and constant amount from the

lab, but is instead offset by slightly different amounts depending on the test point that is considered. Due to the trend agreement between the lab and flight range precision curves and the generally constant offset between them, excellent agreement exists between lab and flight results, with preference being given to the actual range precision numbers from the lab experiment.

Table 3.2 summaries the lab and flight results for var-FOV lidar range precision. Table 3.2 indicates that the field test four range precision goal of eight centimeters is marginally achieved. The real-time lab and flight results show that eight centimeter is not achieved, but the new method being developed and tested by LaRC in post-processing indicates that the goal is achieved over a portion of the intensity span. Since the LaRC method is under development, it is not yet incorporated into camera firmware for real-time operations, but such incorporation is actively underway. Once the LaRC calibration is loaded into camera firmware, the AGC can be used to force operations to occur in the lower intensity portion of the range precision curve where the field test goal of eight centimeters is achieved.

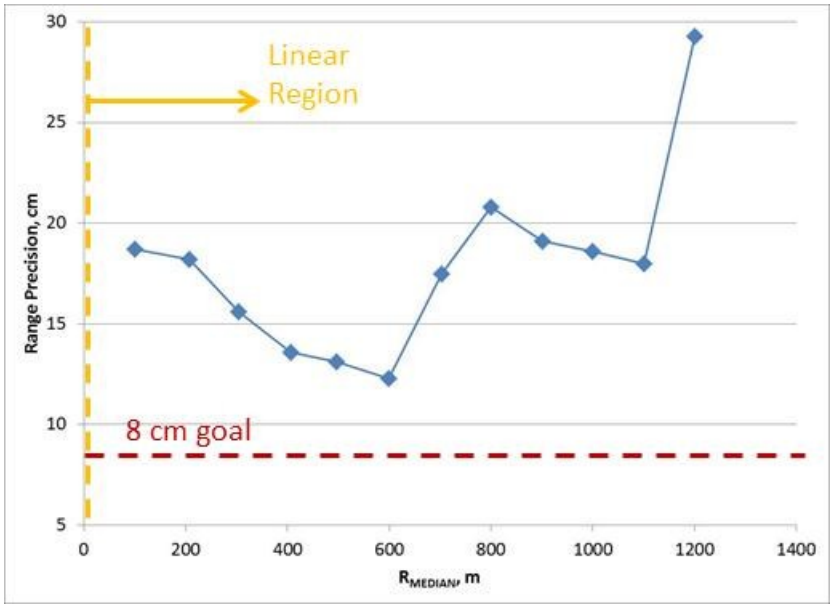

Figure 3.28: Flight #5 (var-FOV lidar) range precision as a function of median range based on images of the flat lakebed. Range precision follows the same the character as lab data in the linear region except with a vertical offset likely due to uncertainty in best fit plane for flight data.

CONCLUSIONS ON TECHNOLOGY ADVANCEMENT AND FUTURE PLANS

4.1 Achievements Comparison with Long-Range Goals

Two flash lidars, integrated from a number of cutting-edge components from industry and NASA, have been lab characterized and flight tested under the ALHAT project (in its fourth development and field test cycle) which is seeking to develop a GNC and sensing system based on lidar technology capable of enabling safe, precise human-crewed or robotic landings in challenging terrain on planetary bodies under any ambient lighting conditions. The flash lidars incorporate pioneering 3-D imaging cameras based on InGaAs APD and novel micro-electronic technology, high pulse-energy 1.06 μm Nd:YAG lasers, and high performance transmitter and receiver fixed and zoom optics. The two flash lidars were characterized on the LaRC Sensor Test Range, integrated with other portions of the ALHAT GNC system from around the country into an instrument pod at NASA-JPL, integrated onto an Erickson Aircrane Helicopter at NASA-Dryden, and flight tested at the Edwards AFB's Rogers dry lakebed over a field of human-made geometric hazards.

Table 4.1 compares the achievements from the present development and test effort to the long-range ALHAT goals. The maximum operational range achievement shown is that of the var-FOV lidar since it incorporates the Fibertek laser which is the laser planned for the final ALHAT system. Although the table shows that the long-range ALHAT goals have been

achieved for maximum operational range, additional maximum range capability is desired to incorporate larger incidence angles for more trajectory flexibility. The lab results (summarized in Table 3.2) do indicate that additional maximum operating range is available, up to 1600m. The var-FOV lidar was only tested to 1200m in flight, even though additional signal was available, since the flights were aimed at verifying the ALHAT goals which for maximum range ended at 1000m. A factor of four additional pixels is needed in order to achieve the long-range goals. The FOV needs to be extended from 16° to 24° to meet the long-range goals. Additional reduction in range precision is needed. The frame rate long-range goal has been achieved. The long-range goal for real-time application of range / intensity calibration coefficients has been achieved. Several hazards are imaged to provide 3-D DEM information at medium ranges. The lidar technology has been advanced to its next level in pursuit of the long-range ALHAT goals. Sensor technology upgrades are needed in order to close the gap between the present state and the long-range goals to ready the systems for use on a space mission.

Table 4.1: Summary of achievements from present development / test cycle compared to ALHAT long-range goals.

Parameter	Field Test 4 Achievements	ALHAT Long-Range Goals
Max operational range	1200 m	> 1000 m
# pixels	128 x 128	256 x 256
FOV	1°, 6° to 16°	Variable 6° to 24°
Range Precision: a) Post-processed b) Real-time	6 to 15 cm 8 to 20 cm	- 5 cm
Frame Rate	30 Hz	30 Hz
Range / Intensity Calibration Application	Real-time	Real-time

4.2 Plans for Technology Advancements Leading to Long-Range Goals

Although the maximum operational range goals have been achieve, 20% or so of additional maximum range capability is desired to not only provide margin, but also ensure that the desired maximum range is possible at a wider range of beam incidence angles and surface types (since surface reflectivity is incidence-angle dependent and planetary body type) to support added flexibility in vehicle attitude which translates directly into flexibility in vehicle trajectory. Lower loss receiver optics are being pursued which are optimized for the new 1.06 um wavelength which should also minimize the number of optical elements needed which minimizes reflection and bulk absorption losses. Transmitter optics redesign is planned to minimize the number of optical elements to reduce beam attenuation. Higher sensitivity camera FPA's are being pursued which incorporate a more sensitive detector array as well as a lower noise ROIC which should lower the noise floor (i.e. increase dynamic range) and allow camera operations at lower detection threshold levels to observe fainter signals from farther ranges.

Improved spatial precision is being pursued to permit hazard detection at maximum range through a factor of four increase in the number of pixels as well as the incorporation of real-time image enhancement processing techniques. The desired GSD has been approached with a 1 deg lens, but the 6 deg FOV lens is preferred at maximum range so that more landing site space can be viewed at once. Detectors and ROIC's which incorporate the factor of four increase in pixels are being developed with prototypes under test. A Real-time image enhancement technique referred to as Super Resolution similar to the familiar digital magnification of consumer cameras is under development and test presently with an initial version embedded in firmware and working in real-time presently. The super resolution technique effectively increases the number

of pixels up to a factor of 8 by combining successive images, each of which are shifted in space by either vehicle motion or vibration, in a way where information between physical pixels is filled in, thereby, effectively increasing the number of pixels.

Improvements are being pursued in zoom optics both for the receiver zoom as well as the transmitter zoom to enable realization of the full 6 to 24 deg travel so that the ground footprint of the field of view is maintained by zooming out (without increasing GSD, which is essentially the ground footprint of one pixel representing a form of spatial precision, above the threshold needed for hazard detection) to compensate for the decreasing range during descent. Improvements being pursed for the receiver zoom optics include miniaturization of the system flown in the present field test series while retaining the constant f/# design point to help ease the saturation issues experienced during the last several hundred feet of descent. The f/# design is set slightly larger than that of the camera detector's micro-lens array so that aperture is minimized and photons are not wasted. A natural result of zooming the receiver lens out during descent is that depth of field is increased which eases the defocus that occurs during the last several hundred meters of descent. Improvements to the transmitter zoom being pursed include coverage of the full 6 to 24 degree range as opposed to the subset of 6 to 16 degrees achieved in the present field test development effort. An additional improvement that is being considered for the transmitter zoom is to extend its maximum divergence angle to permit the option of over-zooming (i.e. over-filling the receiver FOV) the transmitter during descent to help ease the camera saturation issue.

Improved range resolution is being pursued in order to achieve the resolution necessary to enable detection of the desired hazard size at the flight ranges of interest, especially at maximum range where the maximum amount of altitude and time are available to redirect the vehicle to the optimum landing point away from hazards but close to the desired landing point.

Improvements in peak detection and range / intensity calibration are being pursued. Several technologies being pursed are competition sensitive and cannot be discussed by the author. Incorporation of the new, higher performing (per the lab results presented of the present study) LaRC range/intensity calibration into camera firmware is being pursed. An alternative 3-D imaging camera is being developed and tested which approaches peak detection in an analog method, versus the present camera's digital method.

REFERENCES

Amzajerdian, F., M. Vanek, L. Petway, D. Pierrottet, G. Busch, and A. Bulyshev, *Utilization of 3-D Imaging Flash Lidar Technology for Autonomous Safe Landing on Planetary Bodies*, Proc. of SPIE, Vol. 7608, 2010.

Brady, T., and S. Paschall, *The Challenge of Safe Lunar Landing*, Proc. of IEEE Aerospace Conference, Big Sky, MT, March 6 – 13, 2010, pp. 1 – 14.

Cooke, C., J. Cernius, and A. J. LaRocca, "Ranging, Communications, and Simulation Systems," in *The Infrared Handbook*, edited by W. L. Wolfe and G. J. Zissis, p. 23-6, Infrared Information and Analysis (IRIA) Center, Michigan, 1985.

Dries, J. C., B. Miles, and R. H. Stettner, *A 32 x 32 Pixel Flash Laser Radar System Incorporating InGaAs PIN and APD Detectors*, Proc. SPIE, Vol. 5412, 2004.

Epp, C. D., E. A. Robertson, and T. Brady, *Autonomous Landing and Hazard Avoidance Technology (ALHAT)*, Proc. of IEEE Aerospace Conference, Big Sky, MT, March 1-8, 2008, pp. 1- 7.

Hovis, F. E., J. Rudd, J. Edelman, K. Andes, J. Young, *Compact Space-Based Laser for Flash Lidar*, Contract #NNL08AA42C Final Report, 2010.

Huertas, A., A. E. Johnson, R. A. Werner, R. A. Maddock, *Performance Evaluation of Hazard Detection and Avoidance Algorithms for Safe Lunar Landings*, Proc. of IEEE Aerospace Conference, Big Sky, MT, March 6 – 13, 2010, pp. 1 – 20.

LaRocca, A. J., "Atmospheric Absorption," in *The Infrared Handbook*, edited by W. L. Wolfe and G. J. Zissis, p. 23-6, Infrared Information and Analysis (IRIA) Center, Michigan, 1985.

Quantel USA, *User's Manual Centurion Diode Pumped Nd:YAG Laser System, Revision C*, 2008.

Richmond, R., R. Stettner, and J. Glessner, *Eye-Safe Laser Radar Focal Plane Array for Three-Dimensional Imaging*, Proc. of SPIE, Vol. 4035, 2000.

Singh, U. N., S. Ismail, M. J. Kavaya, D. M. Winker, and F. Amzajerdian, "Space-Based Lidar," in *Laser Remote Sensing*, edited by T. Fujii and T. Fukuchi, p. 799, Taylor and Francis Group, Boca Raton, 2005.

Stettner, R., H. Bailey, and R. Richmond, *Eye-Safe Laser Radar 3-D Imaging*, Proc. SPIE, Vol. 4377, 2001.

Stettner, R., H. Bailey, and S. Silverman, *Large Format Time-of-Flight Focal Plane Detector Development,* Proc. SPIE, Vol. 5791, 2005.

Stettner, R., *Compact 3D Flash LIDAR Video Cameras and Applications*, Proc. SPIE, Vol. 7684, 2010.

APPENDICES

APPENDIX A

Range / Intensity Plots Used to Develop the Calibration for Fixed-FOV Lidar

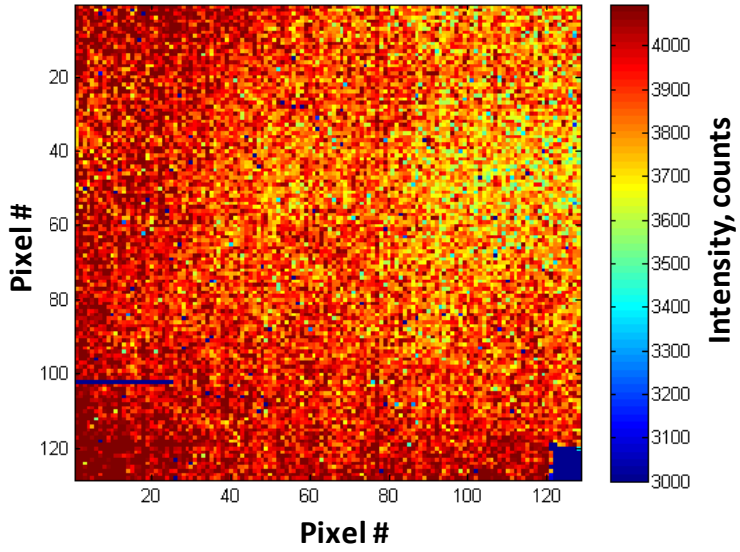

Figure A.1: Intensity plot (at a high intensity with most pixels saturated) of flat STR target board taken by the fixed-FOV lidar at OD = 1.05 during range / intensity calibrations.

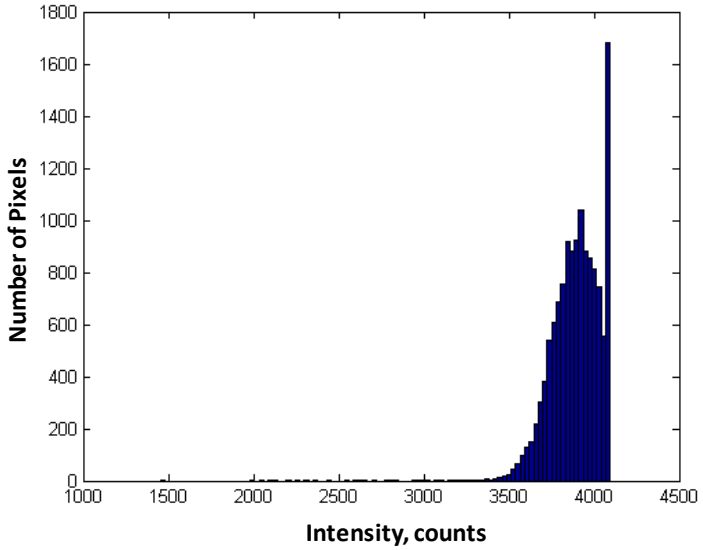

Figure A.2: Histogram of intensity (at high intensity with most pixels saturated) frame from fixed-FOV lidar at OD = 1.05.

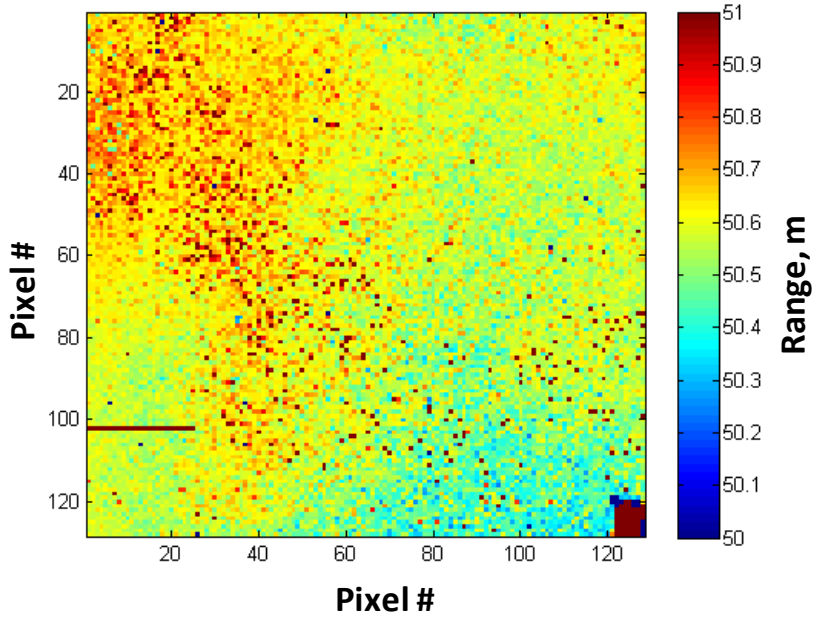

Figure A.3: Range plot (at high intensity case with most pixels saturated) of flat STR target board taken by fixed-FOV lidar at an OD = 1.05 during range / intensity calibrations.

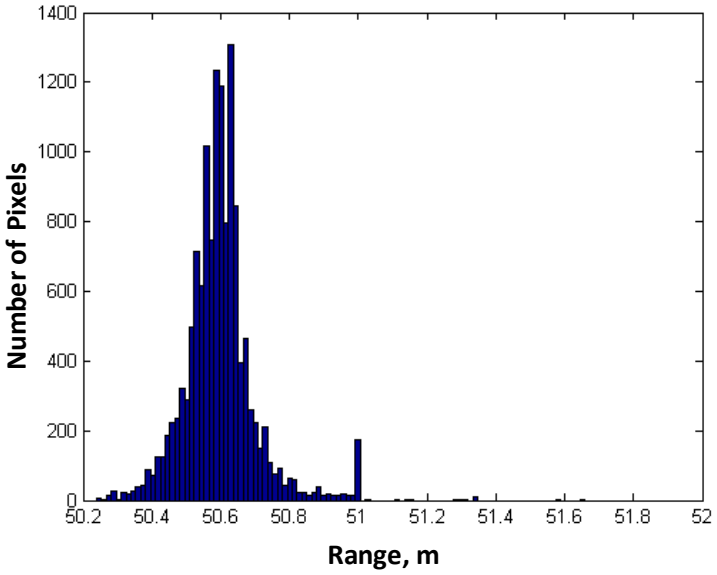

Figure A.4: Histogram of range (at high intensity case with most pixels saturated) from fixed-FOV lidar at OD = 1.05.

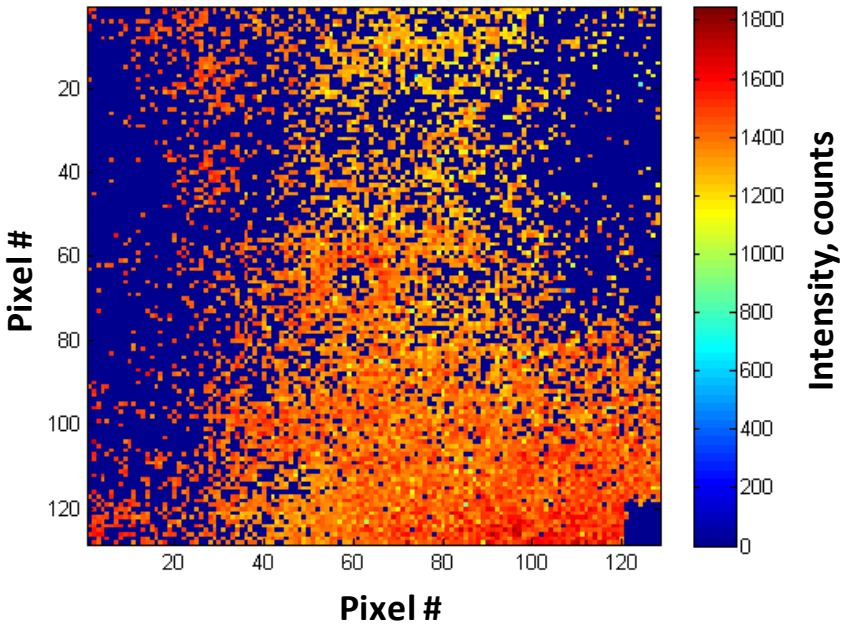

Figure A.5: Intensity plot (at a low intensity with some pixels not triggered) of flat STR target board taken by the fixed-FOV lidar at OD = 2.796 during range / intensity calibrations.

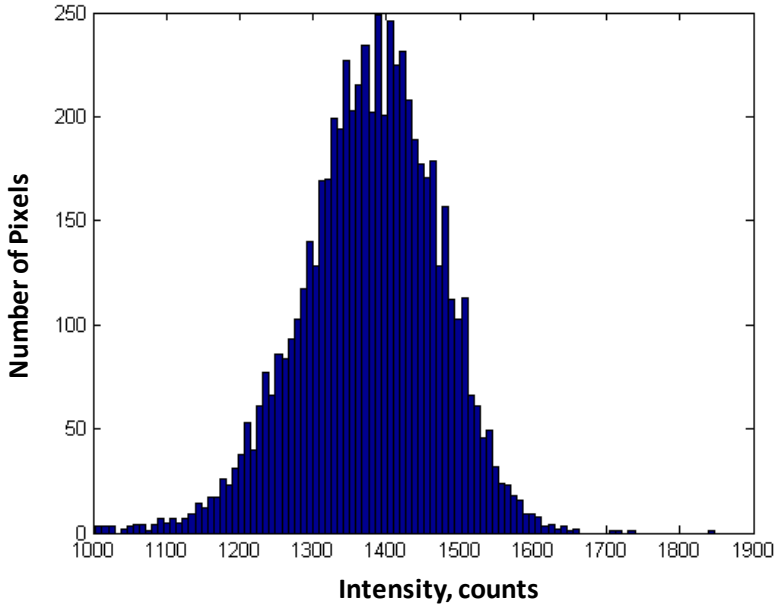

Figure A.6: Histogram of intensity (at low intensity with some pixels not triggered) frame from fixed-FOV lidar at OD = 2.796.

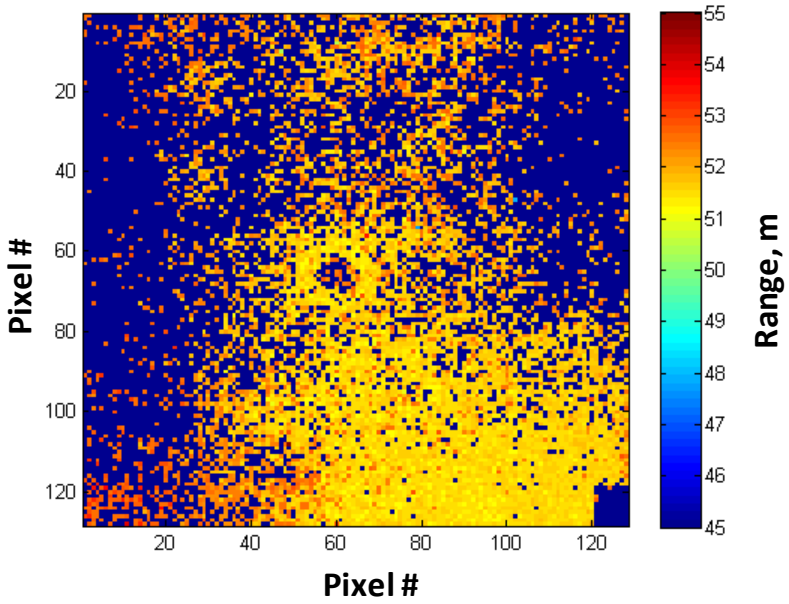

Figure A.7: Range plot (at low intensity case with some pixels not triggered) of flat STR target board taken by fixed-FOV lidar at an OD = 2.796 during range / intensity calibrations.

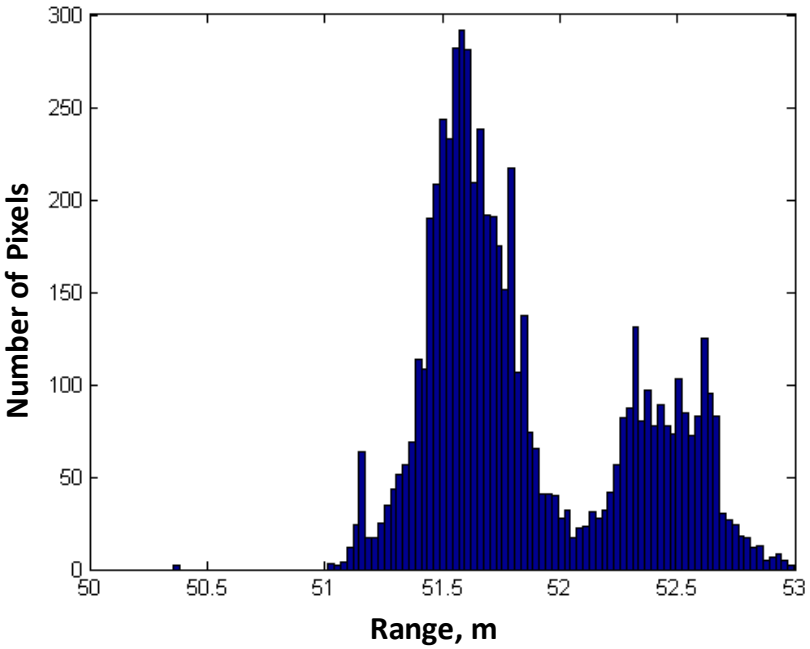

Figure A.8: Histogram of range (at low intensity case with some pixels not triggered) from fixed-FOV lidar at OD = 2.796.

APPENDIX B

Range / Intensity Plots Used to Develop the Calibration for Var-FOV Lidar

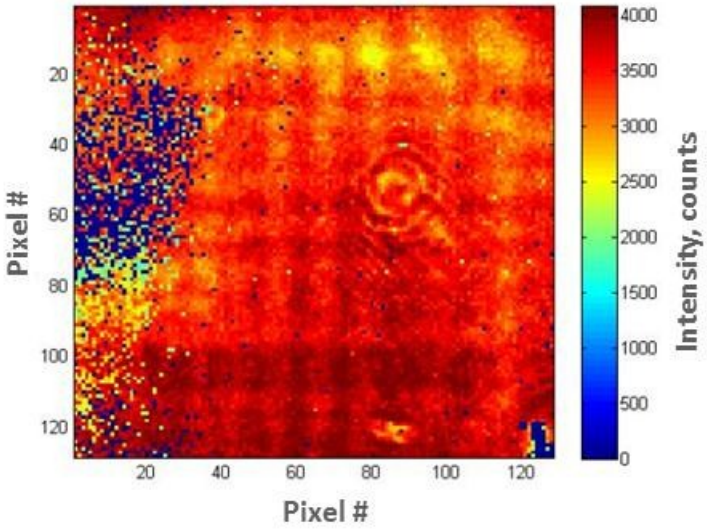

Figure B.1: Intensity plot (at a high intensity with most pixels saturated) of flat STR target board taken by the var-FOV lidar at OD = 2.521 during range / intensity calibrations.

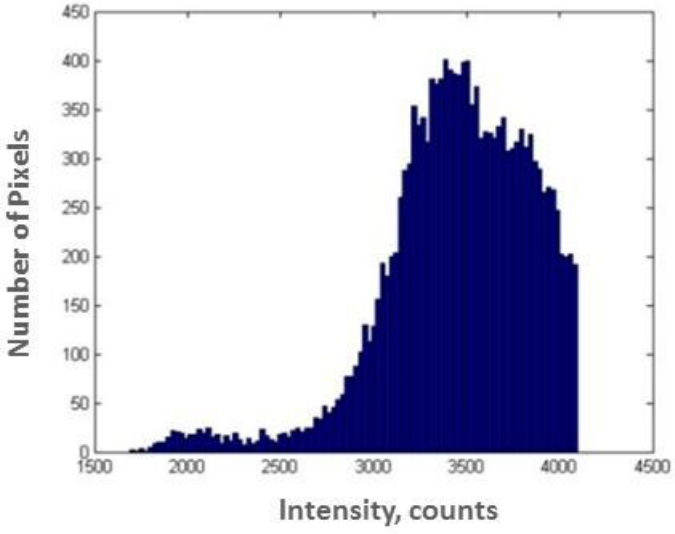

Figure B.2: Histogram of intensity (at high intensity with most pixels saturated) frame from var-FOV lidar at OD = 2.521.

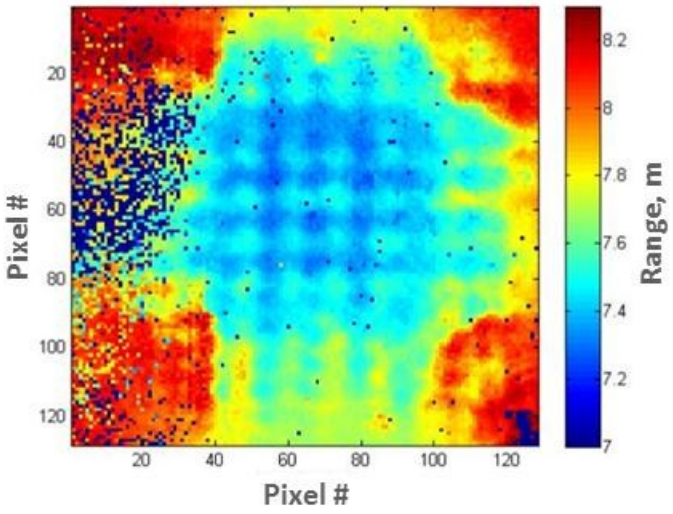

Figure B.3: Range plot (at high intensity case with most pixels saturated) of flat STR target board taken by var-FOV lidar at an OD = 2.521 during range / intensity calibrations.

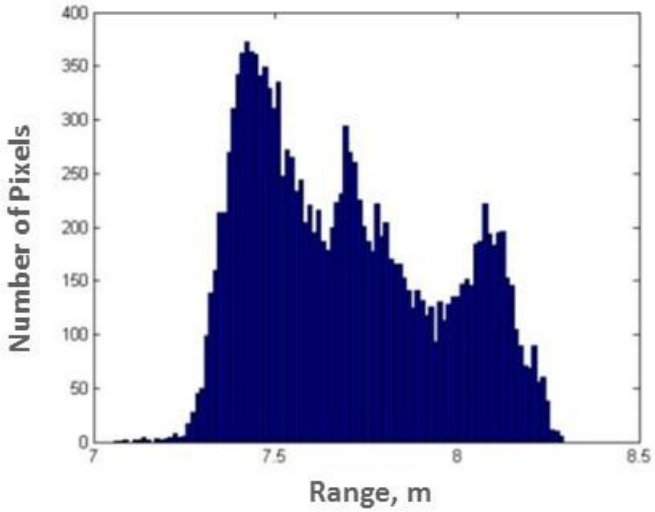

Figure B.4: Histogram of range (at high intensity case with most pixels saturated) from var-FOV lidar at OD = 2.521.

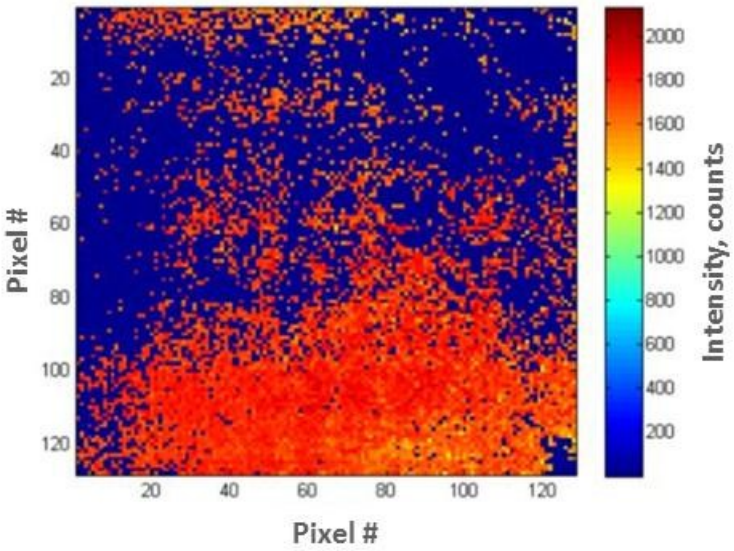

Figure B.5: Intensity plot (at a low intensity with some pixels not triggered) of flat STR target board taken by the var-FOV lidar at OD = 4.126 during range / intensity calibrations.

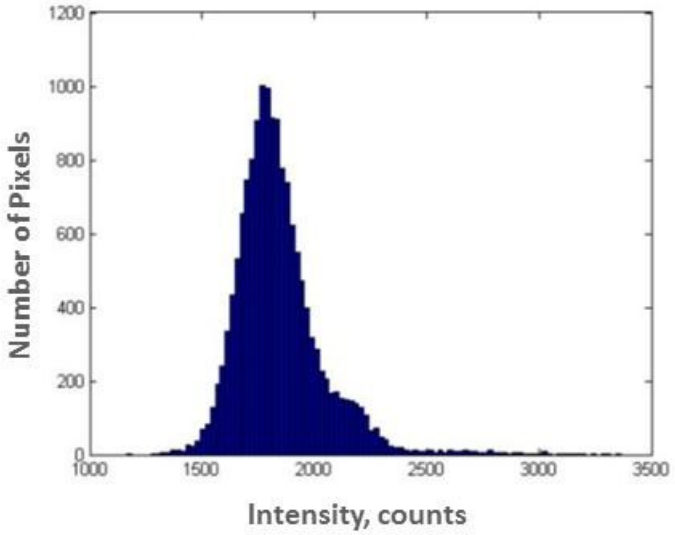

Figure B.6: Histogram of intensity (at low intensity with some pixels not triggered) frame from var-FOV lidar at OD = 4.126.

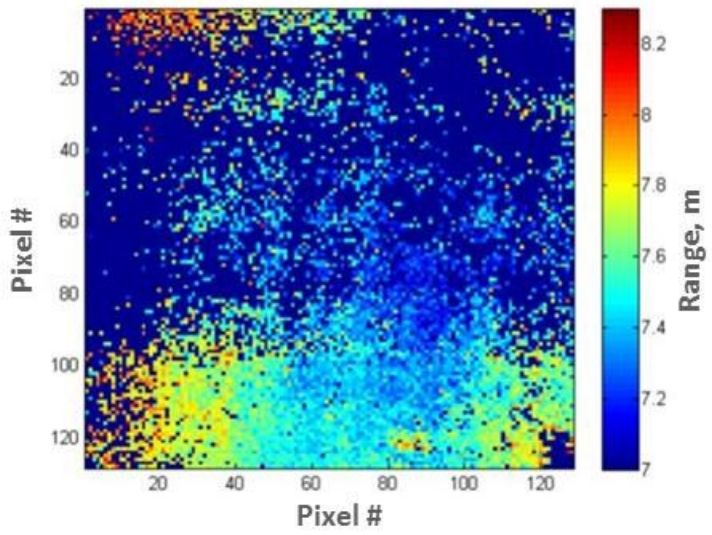

Figure B.7: Range plot (at low intensity case with some pixels not triggered) of flat STR target board taken by var-FOV lidar at an OD = 4.126 during range / intensity calibrations.

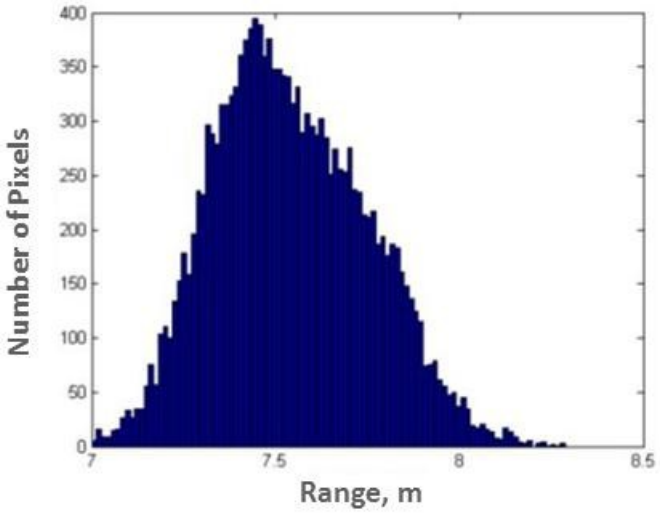

Figure B.8: Histogram of range (at low intensity case with some pixels not triggered) from var-FOV lidar at OD = 4.126.